VILNIUS UNIVERSITY
CENTER FOR PHYSICAL SCIENCES AND TECHNOLOGY

Kristina
KRISTINAITYTE

NMR spectroscopy of structure, diffusion and relaxation in materials used in innovative medicine

DOCTORAL DISSERTATION

Natural Sciences,
Physics N 002

VILNIUS 2019

This dissertation was written between 2015 and 2019 in Vilnius University. The research was supported by Research Council of Lithuania.

Academic supervisor:
Prof. Dr. Nomeda, Rima Valeviciene (Vilnius university, medical and healthcare sciences, medicine – M 001).
Academic consultant:
Prof. Habil. Dr. Vytautas, Balevicius (Vilnius university, natural sciences, physics – N 002).

This doctoral dissertation will be defended in a public/closed meeting of the Dissertation Defence Panel:
Chairman – **Prof. Habil. Dr. Juras, Banys** (Vilnius university, natural sciences, physics – N 002).
Members:
Prof. Dr. Saulius, Bagdonas (Vilnius university, natural sciences, physics – N 002).
Prof. Dr. Virginijus, Barzda (University of Toronto Mississauga, natural sciences, physics – N 002).
Prof. Habil. Dr. Sigitas, Tumkevicius (Vilnius university, natural sciences, chemistry – N 003).
Dr. Jonas, Venius (Nacional Cancer Institute, natural sciences, biophysics – N 011).

The dissertation shall be defended at a public/closed meeting of the Dissertation Defence Panel at 14:00 (hour)/ on 23rd September 2019 in meeting room A101 of the Center for physical sciences and technology (FTMC).
Address: Sauletekio al., 3, A101, Vilnius, Lithuania
Tel. +370 5 264 8884; e-mail: office@ftmc.lt
The text of this dissertation can be accessed at the libraries of (name of the institutions granted the right to conduct doctoral studies in alphabetical order), as well as on the website of Vilnius University:
www.vu.lt/lt/naujienos/ivykiu-kalendorius

VILNIAUS UNIVERSITETAS
NACIONALINIS FIZINIŲ IR TECHNOLOGIJŲ MOKSLO CENTRAS

Kristina
KRISTINAITYTĖ

Struktūros, difuzijos ir relaksacijos vyksmų medžiagose, taikomose inovatyvioje medicinoje, BMR spektroskopija

DAKTARO DISERTACIJA

Gamtos mokslai,
Fizika N 002

VILNIUS 2019

Disertacija rengta 2015– 2019 metais Vilniaus universitete.
Mokslinius tyrimus rėmė Lietuvos mokslo taryba (gauta stipendija už akademinius pasiekimus)

Mokslinė vadovė:
prof. dr. Nomeda Rima Valevičienė (Vilniaus universitetas, medicinos ir sveikatos mokslai, medicina – M 001);
Mokslinis konsultantas:
prof. habil. dr. Vytautas Balevičius (Vilniaus universitetas, gamtos mokslai, fizika – N 002).

Gynimo taryba:
Pirmininkas – **prof. habil. dr. Jūras Banys** (Vilniaus universitetas, gamtos mokslai, fizika – N 002).
Nariai:
prof. dr. Saulius Bagdonas (Vilniaus universitetas, gamtos mokslai, fizika – N 002),
prof. dr. Virginijus Barzda (Toronto universitetas Mississauga, gamtos mokslai, fizika – N 002),
prof. habil. dr. Sigitas Tumkevičius (Vilniaus universitetas, gamtos mokslai, chemija – N 003),
dr. Jonas Venius (Nacionalinis vėžio institutas, gamtos mokslai, biofizika – N 011).

Disertacija ginama viešame / uždarame Gynimo tarybos posėdyje 2019 m. rugsėjo mėn. 23 d. 14:00 val. Fizinių ir technologijos mokslų centre (FTMC) A101 posėdžių salėje / auditorijoje. Adresas: Saulėtekio al. 3, A101, Vilnius, Lietuva, tel. +370 5 264 8884; el. Pastas office@ftmc.lt.

Disertaciją galima peržiūrėti Vilniaus universiteto, Fizinių ir technologijos mokslų centro bibliotekose ir VU interneto svetainėje adresu: https://www.vu.lt/naujienos/ivykiu-kalendorius

ABBREVATIONS

CA – Contrast Agent
CaHA – Calcium Hydroxyapatite
Cho – Choline
Cit – Citrate
COSY - COrrelation SpectroscopY
CP – Cross Polarization
Cr – Creatine
CT – Comupted Tomography
DFT – Density Functional Theory
DSS – 4,4-dimethyl-4-silapentane-1-sulfonic acid
DTI – Diffusion Tensor Imaging (Tractography)
DWI – Diffusion Weighted Imaging
fMRI – functional Magnetic Resonance Imaging
FTIR – Fourier-transform infrared spectroscopy
HA – Hydroxyapatite
HMBC – Heteronuclear Multiple Band Correlation
HMQC – Heteronuclear Multiple Quantum Correlation
LCLC – Lyotropic Chromonic Liquid Crystals
MAS – Magic Angle Spinning
MNP – Magnetic NanoParticle
MRI – Magnetic Resonance Imaging
MRS – Magnetic Resonance Spectroscopy
MRSI – Magnetic Resonance Spectroscopy Imaging
NMR – Nuclear Magnetic Resonance
NP – NanoParticle
NSA – Number of Scans Accumulated (Averaged)
PANO – picolinic acid N-oxide
PET – Positron Emission Tomography
PRESS - Point RESolved Spectroscopy (PRESS)
PT – Proton Transfer
PWI – Perfusion Weighted Imaging
RF – Radio Frequency
SBM – Solomon–Bloembergen–Morgan
SMD – Solvation Model based on Density
SNR – Signal-to-Noise Ratio

Spm – Spermine
SSY – Sunset Yellow FCF
STEAM – STimulated Echo Acquisition Mode
SV – Single Voxel
TE – Time of Echo
TEM – Transmission Electron Microscopy
TR – Time of Repetition
UCNP – UpConverting NanoParticle
VOI – Volume of Interest

CONTENTS

1. INTRODUCTION

In the field of medicine, Nuclear Magnetic Resonance (NMR) spectroscopy has found wide applications including both diagnosis and treatment, where imaging methods have an important role. In the large field of radiology, Magnetic Resonance Imaging (MRI) has some undeniable advantages as a diagnostic tool [1]. First of all, there is no ionizing radiation as using X-ray radiography, computed tomography (CT) or nuclear medicine including positron emission tomography (PET). Secondly, it can give a good contrast between soft tissues in cases, where it is a challenge or even an impossible task for other imaging techniques [2, 3]. Moreover, there is a great variety of MRI contrast agents (CAs) [4, 5] and even more of the advanced ones being investigated or implemented [6, 7], especially as ultra-high-field scanners are on the rise [8]. Currently, hospitals routinely use machines with field strengths of 1.5 T or 3 T. There are already dozens of 7 T machines in research labs, but only in 2017, the first 7 T model was cleared for clinical use. At the extreme end there are scanners designed for humans that reach beyond 10 T [9].

Fast development of image acquisition techniques [1] such as perfusion-weighted imaging (PWI) [10], magnetic resonance spectroscopy (MRS) [11], functional MRI (fMRI) [12] or diffusion-weighted imaging (DWI), including diffusion tensor imaging (DTI) [13], have revolutionized the use of MRI in the clinics improving its sensitivity and detection capability. These techniques provide great insight into physiologic mechanisms and pathologic conditions, tracing the links between tissue microstructure, metabolism, and hemodynamics. Probably one of the most debatable MRI modalities is MRS. It uses principals of ^{1}H-NMR spectroscopy for in vivo measurements. ^{1}H-NMR spectrum of metabolites is obtained directly from the selected voxel. The results provide critical information related to the downstream products of many cellular and metabolic processes which could provide a snapshot of the health/disease status of a particular tissue or organ leading to early diagnosis [14]. However, there are some challenges, such as restricted measurement time due to patient compliance, motion artifacts, low-concentration metabolites, highly inhomogeneous environment or water frequency determination to ensure that actual voxel location is equal to the intended one, as well as to achieve good water and lipid suppression. There are sophisticated approaches [15-18] which help to cope with some problems, but unfortunately, they are not applied in every hospital and even if they were, the qualified

experimenter would be needed. If experimental data is collected and processed properly, the obtained MRS results give a valuable clinical information enabling early detection of oncological diseases. However, sometimes it is a difficult task to achieve. Therefore, MRS is not a standardized procedure in clinical routine yet and instead, is more favorable in research centers.

Early diagnosis is essential for successful treatment, thus this area of research has been rapidly growing. Nanotechnology, combined with other disciplines, such as molecular biology and imaging technology, provides unique capabilities enabling innovative diagnosis and therapy using nano-materials [19]. Magnetic nanoparticles (MNPs), due to recent advances in their production, functionalization and biocompatibility [20, 6], have found many applications, ranging from conventional MRI contrast agents or more advanced targeted [21] and multimodal [22, 23, 7] ones to MNPs used in therapy for selective drug delivery [24-27] or biosensors [28, 29]. Innovative portable NMR biosensors are capable of detecting bacteria with high sensitivity, identify small numbers of cells, analyze them on a molecular level in real time and measure a series of protein biomarkers in parallel [30]. Such biosensors use magnetic nanoparticles as proximity sensors to amplify molecular interactions. Nano-structured materials provide a novel possibility for molecular isolation putting water molecules in unusual conditions. Some of those materials, such as hydroxyapatite (HA) can be utilized in bone tissue engineering. Different magnetic nanoparticles are combined with HA to promote bone formation and cell growth [31, 32 and references therein]. The knowledge about water states and structures present in systems with restricted geometry can be useful creating the series of nano-materials, as well as correlating the short-range order effects with macroscopic properties, like, strength, flexibility, aging effects etc., and maybe even with biocompatibility.

Fast development of explicit and novel applications of nanomaterials in nearly all domains is undeniable [33]. New synthesis routes, as well as the characterization methods, are extremely important. The versatility of NMR brought an array of applications in industry and academia, encompassing basic research into the structure and dynamics of inorganic and biological systems, development of novel materials, medical diagnostics, and many others. Therefore, it is very welcome addressing potential future developments of nano-structure materials and NMR-based methods applied in clinical routine.

1.1 Goals and tasks of the work

1. To adapt MRS technique at Vilnius University Hospital Santaros Klinikos (VULSK) and to test alternative methods for prostate malignance identification.

2. To investigate the influence of different sized Gd-based upconverting nanoparticles on water diffusion and spin–lattice relaxation at different magnetic field strength in order to elucidate the key factors enhancing the relaxation of contrast agents for MRI.

3. The precise study of temperature and composition effects on the phase behavior, slow self-assembling processes and tautomeric equilibrium in aqueous solutions of lyotropic chromonic liquid crystals (LCLCs) applying high-resolution ^{1}H and ^{15}N NMR spectroscopy.

4. To study the states of water and hydrogen-bond clustering process of molecules confined in series of nano-structured calcium hydroxyapatites (CaHAs) applying solid-state NMR spectroscopy; to compare the results with those that follow from the FTIR study on water clustering in liquid solutions and inert matrices.

1.2 Statements of doctoral thesis

1. The behavior of NMR spectra of prostate metabolites is sensitive to the changes in pH. A difference in chemical shifts between pH-dependent metabolite citrate and pH-independent metabolite choline might be a good additional indicator for malignant tissue in early diagnosis.

2. Different magnetic field strengths did not alter the spin–lattice relaxivity of water in presence of gadolinium (Gd)-based upconverting nanoparticles (UCNPs). This suggests that Gd-based UCNPs could be developed into high-performance multimodal magnetic resonance imaging (MRI) contrast agents working over a broad range of imaging field strengths used in clinical routine.

3. The tautomeric equilibrium in Sunset Yellow FCF (SSY) is strongly shifted towards the hydrazone form. The dominance of the hydrazone form was confirmed experimentally using the long-range ^{1}H–^{15}N

correlation, widely known as HMBC. The corresponding equilibrium constant $pK_T = 2.5$ was deduced using the quantum chemistry DFT SMD model.

4. The growing of SSY aggregates is accompanied by the segregation of water in the intercolumnar areas with no access for exchange with the N–H protons in the internal layers of the columnar stacks; the life time of those aggregates is $\geq 10^{-8}$ s or even longer.

5. The equilibration time at the nematic to columnar phase transition in SSY aqueous solutions is very long because of slow supramolecular restructuring, i.e. the growing of columnar stacks and building of hexagonal arrays. These processes affect the shape and shift of the ^{1}H NMR signals and are easy to monitor.

6. The water cluster structure and the size in nano-structured calcium CaHAs depends on the hydration level. Hexamer- or even higher structures were observed only in the samples containing significant amount of adsorbed water. The amount of adsorbed and surface structured water can be probed using ^{1}H MAS NMR technique.

1.3 Scientific novelty

1. pH dependences of chemical shifts of main prostate metabolites in aqueous solutions were analyzed implementing both high resolution 400 MHz ^{1}H NMR and 128 MHz MRI scanner. A model of prostate phantom was developed which will be used for further development of MRS technique at Vilnius University Hospital Santaros Klinikos.

2. In the frame of simplified Solomon–Bloembergen–Morgan (SBM) model it was shown that two measured diffusion coefficients are associate with processes occurring near the surface of UCNPs and in bulk water. Using the relationship between relaxation and diffusion, the total impact of NPs on relaxation of water molecules as well as the impact on relaxation of local water molecules, directly connected to paramagnetic Gd^{3+} ions in NPs, were estimated.

3. The peak in ^{1}H NMR spectra at ca 14.5 ppm was found for the first time and can be attributed to the proton in the intramolecular N–H…O bond. The existence of this signal shows that the growing of SSY aggregates is accompanied by the segregation of water in the intercolumnar areas with no access for exchange with the N–H protons in the internal layers of the columnar stacks.

4. The temperature dependences of H_2O chemical shift and Raman O–H stretching band shape show that water confined in the intercolumnar areas behaves as in the neat substance. When the sample is heated and the transition from M phase to N phase occurs, the molecular motion of water is seen to change in a manner similar to that when water is melting.

5. If the sample is cooled down to the temperature below N $\rightarrow$ M transition relatively fast, the structural changes are behind, and the system falls into supercooled state. In this case, the system evolves via long lasting self-assembling from the supercooled state to the equilibrium. This process was monitored using ^{1}H NMR spectroscopy for the first time.

1.4 Publications included in the thesis

1. **K. Kristinaityte**, J. Razanskas, V. Paketurytė, Nomeda R. Valeviciene, V. Balevicius, Methods of Sample Preparation for Analysis and Quality Assurance of Prostate MR Spectroscopy, Medical Physics in the Baltic States 13 (2017) p. 61-64.

2. **K. Kristinaityte**, L. Dagys, J. Kausteklis, V. Klimavicius, I. Doroshenko, V. Pogorelov, N. R. Valevicienė, V. Balevicius, NMR and FTIR studies of clustering of water molecules: from low-temperature matrices to nano-structured materials used in innovative medicine, Journal of Molecular Liquids, 235 (2017) p. 1-6.

3. **K. Kristinaityte**, A. Marsalka, L. Dagys, K. Aidas, I. Doroshenko, Y. Vaskivskyi, Y. Chernolevska, V. Pogorelov, N. R. Valevicienė, V. Balevicius, NMR, Raman, and DFT Study of Lyotropic Chromonic Liquid Crystals of Biomedical Interest: Tautomeric Equilibrium and Slow Self-Assembling in Sunset Yellow Aqueous Solutions, J. Phys. Chem. B., 122 (2018) p. 3047-3055.

4. **K. Kristinaityte**, T. Zalewski, M. Kempka, S. Sakirzanovas, D. B. Paulaviciene, S. Jurga, R. Rotomskis, N. R. Valeviciene, Spin-Lattice Relaxation and Diffusion Processes in Aqueous Solutions of Gadolinium-Based Upconverting Nanoparticles at Different Magnetic Fields, Appl. Magn. Res., 50 (2019) p. 553-561.

1.5 Presentations at the conferences

1. K. Kristinaitytė, B. Gricienė, Patient radiation doses in head, chest, abdominal and pelvis CT procedures, Medical Physics in the Baltic States 12, Kaunas, Lithuania, 2015.

2. K. Kristinaitytė, L. Dagys, J. Kausteklis, V. Klimavicius, I. Doroshenko, V. Pogorelov, N. Valevičienė, V. Balevicius, NMR and FTIR studies of clustering of water molecules: from low-temperature matrices to nano-structured materials used in innovative medicine, Physics of Liquid Matter: Modern Problems (6^{th} PLMMP-2016), Kyiv, Ukraine, 2016.

3. K. Kristinaitytė, J. Kausteklis, A. Ežerskytė-Misevičienė, V. Klimavicius, L. Dagys, N. R. Valevičienė, A. Kareiva, V. Balevicius, Spectroscopy of States of Water in Advanced Nano-Structured Materials for Innovative Medicine, American Advanced Materials Congress (AAMC-2016), Miami, USA, 2016.

4. K. Kristinaitytė, N. R. Valevičienė, A. Marsalka, I. Doroshenko, V. Pogorelov, V. Balevicius, ^{1}H NMR study of lyotropic liquid crystals with biomedical interest and metabolites in water solutions, XXIII Galyna Puchkovska International School-Seminar "Spectroscopy of Molecules and Crystals" (XXIII ISSSMC), Kyiv, Ukraine, 2017.

5. K. Kristinaityte, J. Razanskas, V. Paketurytė, Nomeda R. Valeviciene, V. Balevicius, Methods of Sample Preparation for Analysis and Quality Assurance of Prostate MR Spectroscopy Medical Physics in the Baltic States 13, Kaunas, Lithuania, 2017.

6. K. Kristinaitytė, A. Maršalka, L. Dagys, K. Aidas, I. Doroshenko, Y. Vaskivskyi, Y. Chernolevska, V. Pogorelov, N. Valevičienė, V.

Balevicius, Tautomeric Equilibrium and Slow Self-Assembling in Aqueous Solutions of Lyotropic Chromonic Liquid Crystal Sunset Yellow, Physics of Liquid Matter: Modern Problems (8th PLMMP- 2018), Kyiv, Ukraine, 2018.

7. K. Kristinaityte, T. Zalewski, M. Kempka, V. Balevicius, S. Jurga, Gd - Based Upconversion Nanoparticles as A Multimodal Contrast Agents, the AMPERE NMR school, Zakopane, Poland, 2018.

8. N. R. Valeviciene, V. Balevicius, K. Aidas, L. Dagys, A. Marsalka, K. Kristinaityte, V. Pogorelov, Y. Chernolevska, Y. Vaskivskyi, I. Doroshenko, G. Pitsevich, U. Sapeshka, NMR, Raman and DFT Study of Tautomeric Equilibrium and Slow Self-Assembling in Lyotropic Chromonic Liquid Crystal SSY Aqueous Solutions, 73rd International Symposium on Molecular Spectroscopy (ISMS 2018), Chicago, IL, USA, 2018.

9. K. Kristinaityte, S. Dragunas, S. Sakirzanovas, D. Baziulyte - Paulaviciene, L. Dagys, R. Rotomskis, N. R. Valeviciene, V. Balevicius, NMR Relaxation Rates and Diffusion Processes in Aqueous Solutions of Gd (III) Ion Doped Upconversion Nanoparticles, A European Magnetic Resonance Meeting (EUROMAR 2018), Nantes, France, 2018.

10. K. Kristinaityte, J. Razanskas, N. R. Valeviciene, V. Balevicius, ^{1}H - NMR Spectroscopy in Prostate Cancer: pH Evaluation as Additional Indicator for Malignant Tissue, 7th Baltic Congress of Radiology (BCR 2018), Kaunas, Lithuania, 2018.

1.6 Authors contribution

The majority of NMR experimental work presented in the thesis was done by the author. Part of experimental setup was prepared together with Laurynas Dagys. Other experimental work was carried out by the co-authors: FTIR analysis of CaHA by Jonas Kausteklis, 2DCOR calculations by Vytautas Balevičius, DFT calculations by Kęstutis Aidas, cross-polarization (CP) MAS NMR experiment by Vytautas Klimavicius. The data analysis, preparation of publications and presentations were a team work of all authors.

2. OVERVIEW

Regarding the reviewed application of NMR-based methods and materials in clinics four types of substances were chosen: metabolites present in prostate, up-converting nanoparticles (UCNPs) as MRI contrast agents (CAs), sunset yellow (SSY) as a lyotropic chromonic liquid crystal (LCLC) used in biosensors and calcium hydroxyapatite (CaHA). The first two can be directly applied in NMR-based imaging modalities as potential cancer biomarkers. The second two are innovative materials that can be utilized in medicine and NMR spectroscopy is a useful tool for their analysis. Metabolites of prostate were chosen because prostate MRS is the most frequently used complimentary to MRI modality in Vilnius University Santaros Klinikos (VULSK). Other materials were chosen considering the availability and the contribution that has been made analyzing these materials with parallel methods such as Raman or FTIR spectroscopy. In a forthcoming chapter a short overview about the materials analyzed in this dissertation will be presented.

2.1 Main metabolites of prostate

A metabolite is the intermediate end product of metabolic reactions catalyzed by various enzymes that naturally occur within cells. Metabolites have various functions, including fuel, structure, signaling, stimulatory and inhibitory effects on enzymes, catalytic activity of their own, defense and interactions with other organisms. The major component of prostate is citrate (Cit). Its extraordinarily high concentration ranges from around 40 up to 150 mM. For comparison, there are only about 0.2 mM of citrate in blood plasma [34]. Other main present metabolites are creatine (Cr, 5 mM), choline (Cho, 1 mM), spermine (Spm, 6 mM) [35 and citations therein].

It is well known that proliferating tumor cells have different metabolic requirements from normal, differentiated cells and consequently exhibit altered levels of many metabolites associated with cell growth as well as energetics, stress and tissue-specific biochemistry. However, what is less well understood are the differences in metabolism between tumors by their degrees of severity [36 and citations therein]. Prostate cancer is an attractive model from a metabolic perspective. The hallmark of the healthy prostate epithelial cell is the zinc accumulating, citrate synthesizing phenotype. Malignant prostate cells reverse this phenotype and adopt a zinc wasting, citrate oxidizing phenotype [37, 34], thereby resulting in significant decrease of citrate.

Conversely, the choline and creatine levels are low in normal peripheral zone and increase in malignant loci. It is likely that the choline increase is associated with membrane structures [38, 34].

Understanding the biologic mechanisms underlying the development of prostate cancer is critical for improved therapeutic and prevention strategies. Prostate-specific-antigen (PSA) test has been used as a standard screening procedure for prostate cancer detection. However, despite being *prostate*-specific, PSA testing is not *cancer*-specific [39]. Thus, new screening and risk stratification methods for both initial diagnostic and follow-up care would have an immense benefit. Increasingly, metabolomics is being explored to address this need. For prostate metabolite profiling NMR-based metabolomics uses samples of urine, serum or prostate tissue from needle biopsy [39, 40 and citations therein, 41]. Another approach is to use in vivo ^{1}H-NMR spectroscopy in combination with regular MRI. In clinical terminology this modality is called magnetic resonance spectroscopy (MRS). Compared to fluid NMR, an obvious advantage is that we can assess metabolite levels directly in the human body as well as at any desired location and if needed simultaneously at different locations.

Metabolic information obtained by MRS can be helpful in diagnosis as well as in monitoring of different tumors, such as brain or breast [42 and citation therein]. Advanced applications of MRS have also been implemented: functional MRS (fMRS) [43] to study metabolism of activated human cortex, diffusion tensor MRS [44, 45] to investigate the diffusion properties of metabolites, ^{13}C-NMR [46] to dynamically study metabolic pathways using intravenous ^{13}C-labeled substrate or to detect glycogen, and ^{31}P-NMR [47,48] providing information about energy metabolism, membrane degradation and pH *in-vivo*. Although nowadays most clinical MRI scanners have sequences for ^{1}H-MRS measurements, the modality is usually not routinely applied. There are some technical challenges such as restricted measurement time due to patient compliance, motion artifacts, low-concentration metabolites, highly inhomogeneous environment, water and lipid suppression, poor spatial resolution or water frequency determination to ensure that the actual voxel location is equal to the intended one. Several methods have been proposed suggesting solutions for some of the mentioned problems. As for example, newer signal processing technologies allow rapid acquisition of undersampled k-space data, leading to reduced acquisition time [49], new sequences minimize spectral contamination by signals arising from tissue outside the prostate [50], improved methods for estimation and correction of frequency

and phase drift help to avoid artifactual line broadening, line shape distortion and reduced SNR [51].

Unfortunately, incorporation of technical advances in clinic units can be a difficult task to achieve, especially if the clinic is not a research center. A lot of depends on the manufacture of the MRI machine as well. Moreover, a qualified physicist is needed. Therefore, although the variety of applications and promising results have stimulated a surge of interest in MR spectroscopy, this modality is still considered an "investigational technique" and is more preferable in research centers rather than in clinics. To facilitate clinical acceptance and standardization, consistent guidelines for data acquisition and analysis, quality assessment, and interpretation are still needed [52]. The key technique for achieving reproducible and accurate MRS results is phantom testing. Phantom design and solutions must be of the highest preciseness and reproducibility so that they can act as a stable reference point for any alterations made on the imaging parameters.

In this dissertation a homemade MRS phantom containing main prostate metabolites (Cit, Cho, Cr and Spm) was prepared. Aqueous solutions of these metabolites were analyzed using high resolution ^{1}H-NMR spectrometer. The obtained results were later applied for further development of MRS technique at Vilnius University Hospital Santaros Klinikos.

2.2 Upconverting nanoparticles

MRI contrast agents are widely used in clinical routine and has expanded beyond the initial expectations since the approval of the first MRI contrast agent which dates back to 1988 and is called gadopentetate dimeglumine (Magnevist®) [53, 4, 5]. Today, CAs are applied in approximately 30% of all MRI procedures [54]. Most important class of commercially available CAs [53, 54, 4, 5] are complexes of the paramagnetic Gadolinium (III) ion which is chelated with hydrophilic polyaminocarboxylate ligands to reduce the toxicity of the heavy metal.

Developments in scanner hardware, image acquisition techniques and reconstruction methods have stimulated MRI to evolve to magnetic fields of higher strength [8, 9]. It provides an opportunity to improve the sensitivity of imaging and allows contrast dose reduction without compromising image quality. However, it is well known that longitudinal relaxivity (r_1) of most common Gd-based commercial contrast agents typically decreases with increasing magnetic field [54-56]. Thus, there is an ongoing need to create

new contrast agents. In the last decade different kinds of nanoparticles, such as targeted/tissue-specific or multimodal ones [21-27], have attracted significant attention as potential imagine probes.

The novel up-converting Gd-containing nanoparticles (UCNPs) were studied in this dissertation. The main advantage of these NPs is that they can be used as multimodal contrast agents for MRI and optical imaging. Besides, the toxicity of the heavy metal would be reduced compared to commercial CAs. Upconverting nanoparticles (UCNPs) are inorganic crystalline nanomaterials that can convert near-infrared (NIR) excitation light into visible and ultraviolet emission light. Excitation with NIR light minimizes autofluorescence background and enables deeper penetration into biological samples due to reduced light scattering. Adding gadolinium into the UCNP turns such a compound into a paramagnetic system, which can be used as MRI contrast agent. Water molecules interact with unpaired electrons of the paramagnetic ion, resulting in a reduction of the proton spin-lattice relaxation time (T_1), which means that water proton relaxivity is increased [57]. Approaches of UCNPs are still at the experimental stage. Typically, three techniques are applied for obtaining high relaxivity CAs at the nanoscale: size control, surface modification and shape regulation. It has been widely known that the coating layers of UCNPs enhance their fluorescent intensities [58-60]. However, the main challenge remains: how to optimize the NP's structure and size in order to achieve the most efficient relaxivity without loss of their optical properties.

When surfactant molecules are used, they interact with water, hence diffusion of water molecules must decelerate. That affects the behaviour of the spins, if the external magnetic field is inhomogeneous. This is the reason why diffusion measurements as well as T_1 relaxation measurements can give fundamental details of such system when effectiveness of MRI contrast agent is concerned.

2.3 Lyotropic chromonic liquid crystals

Lyotropic liquid crystals represent an intersection of several challenging fields of research - supramolecular self-assembling and broad variety of processes in ordered complex fluids [61, 62]. The spontaneous aggregation due to a combination of wide set of molecular interactions, media, and hydrophobic effects are very important phenomena in the field of both fundamental research and technological applications such as the development

of new materials or new ways to treat diseases [63, 64, 65]. The importance of the balance between different types of intermolecular forces for designing processes at molecular scale was reported recently [66], showing that the transfer of assembles of the lipid rafts into the surfactant-based lyotropic liquid crystals can be realized.

Lyotropic chromonic liquid crystals (LCLCs) are a novel and important yet relatively poorly studied class of soft matter. These materials have attracted considerable attention first of all in the areas of optics and innovative biomaterials [67-69]. The combination of self-assembling, ease of alignment, and sensitivity to changing conditions and additives, coupled with their optical properties, makes these systems unique and valuable for creating micropatterned materials and constructing various sophisticated components and devices, including polarizers, optical compensators, and light-harvesting equipment. The fact that LCLCs are water-based suggests and promises a future role in biosensing for medical diagnostics. And indeed, there was noted a growing interest in using the liquid crystals in biological sensors as the medium that amplifies the reactions in molecular and meso(submicron) scales rescaling those to the macroscale, which is accessible for detection [70]. Small and isolated particles do not disrupt the uniform alignment of LCLC, but the formation and growth of immune complexes trigger director distortions detectable by optical means [70]. The combination of liquid crystal display technology and biochemical techniques promises a new generation of medical diagnostic tools - small and portable, inexpensive LCLC biosensors with simplified experimental setup, capable of operating remote from laboratory [71, 72].

Chromonic phases are usually formed in water from disk-like or plate-like multiring aromatic compounds including drugs, dyes and nucleic acids. These phases occur as the result of the face-to-face aggregation of the molecules into columns forming stacks with the ionic solubilizing groups exposed at the aggregate−water interfaces [67-69, 73]. There are two principal chromonic phases - the N phase, which consists of a nematic array of columns and the M phase (also called columnar) at higher concentrations, which has columns laying in a hexagonal array (Fig. 2.3.1).

The most well-known LCLC materials are disodium cromoglycate, also called cromolyn sodium, and 6-hydroxy-5-[(4-sulfophenyl)azo]-2-naphthalenesulfonic acid, also known as Sunset Yellow FCF (SSY) or Edicol. Recently, the phases and structure of mixtures composed of these two representative chromonic liquid crystal materials in water have been studied

using polarized light microscopy, microspectroscopy, centrifugation, and X-ray diffraction [74]. A variety of combinations of isotropic (I), nematic (N), and columnar (M) phases are observed depending on their concentrations. It was noted that their miscibility in the M phase is so low that essentially a complete phase separation occurs. This phase behavior of the mixture is due to both separation of the molecules in the formation of the aggregates and separation of aggregates of the same species by their slow diffusion.

The precise study of temperature and composition effects on the phase behaviour, slow self-assembling processes, and tautomeric equilibrium in SSY aqueous solutions applying NMR is presented in this dissertation.

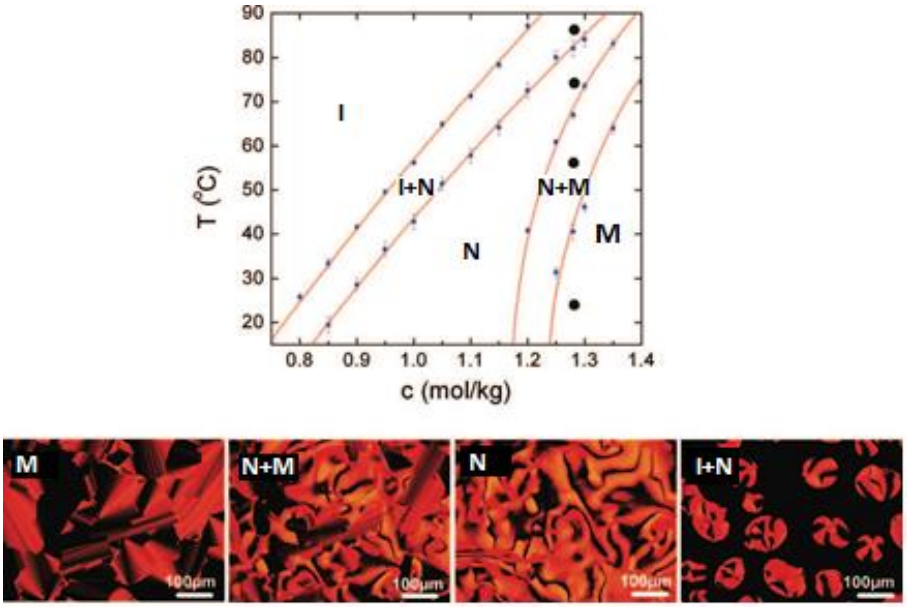

Fig 2.3.1 Phase diagram and polarizing microscope textures of SSY water solutions (adapted from Park et al. [69]) Note the close similarity with Horowitz et al. data [66]

2.4 Hydroxyapatite

Water can be considered as convenient and at the same time rather complex model to investigate the cooperative interactions and the structural organization of molecular clusters sized over the nano- and mezzo-scales. This can be done by isolating water molecules in low-temperature matrices [75-78], dissolving them in hydrophobic solvents [79], confining in carbon nanotubes [80] or in other mesoporous carbon materials [81,82]. In restricted

geometries water molecules can interact with surfaces through hydrophobic and hydrophilic interactions and hydrogen-bond interactions. The competition between the surface–liquid and liquid–liquid interactions can lead to the appearance of interesting new structures and dynamical features of the water that are not observed in bulk water [82]. Hence the nano-structured materials provide a novel possibility for molecular isolation putting molecules in unusual conditions never met before. Moreover, some of those materials, like e.g. calcium hydroxyapatite ($Ca_{10}(PO_4)_6(OH)_2$, further - CaHA), have found many applications in innovative medicine.

Hydroxyapatites (HA) are widely applied in implantology, orthopedic and periodontal surgery, drug carriers or bone regeneration [83-88]. Rapid progress in tissue engineering has led to the development of novel nano-structured materials that can be used for the treatment of bone defects, i.e. to replace tissue which is damaged either by trauma or disease, or due to congenital defects in sequential order. Bone regeneration materials are designed to stimulate osteoinductivity, osteoconductivity, osteointegration, biocompatibility, resorbence, and bone-like mechanical properties. Different additives can be introduced into the HA ceramics, in order to promote bone formation and cell growth with some of these properties [31, 32 and references therein]. Due to close similarity to the mineral components of hard tissues (bone, enamel, dentin, etc.), calcium hydroxyapatite (CaHA) is highly biocompatible and therefore is one of the most favorable materials used in bone tissue engineering [85]. The knowledge about water states and structures present therein can be useful creating the series of nano-materials as well as correlating the short-range order effects with macroscopic properties, like, strength, flexibility, aging effects etc., and maybe even with biocompatibility. Therefore, it is challenging to obtain more novel data on the states of water and the clustering phenomena in these materials.

In this dissertation ^{1}H MAS NMR spectroscopy was used to study the H-bond clustering of water molecules confined in an argon matrix and in nano-CaHAs. The knowledge about water clustering in inert matrices was applied recognizing and assigning the water clusters and explaining NMR features of water in series of nano-CaHAs (home-made and commercial ones).

3. METHODOLOGY

Nuclear magnetic resonance (NMR) as a physical phenomenon was first observed in 1946 by two independent teams led by Felix Bloch at Stanford and Edward Mills Purcell at Harvard [89, 90]. The NMR spectrometer is basically a device capable of three things: magnetizing the ensemble of nuclear spins with a large applied magnetic field, rotating the spin polarizations by radiofrequency (RF) pulses to produce transverse nuclear magnetization and detecting the small oscillating electric currents induced by the precessing transverse spin magnetization [91]. Most NMR experiments require an extremely homogeneous magnetic field which must be maintained over the entire volume of the sample. However, in 1972, Paul Lauterbur and Peter Mansfield realized independently that controlled inhomogeneity can be enormously useful examining the spatial structure of an object [91, 92]. Later on, in 2003, they were awarded the Nobel Prize for their role in the early development of NMR imaging. These days, applications of novel NMR approaches remarkably expended across the fields of innovative medicine and materials research.

In this chapter main topics regarding dissertation will be touched, namely NMR in clinical routine, solid state NMR, 2D correlational spectroscopy, NMR relaxometry and diffusion measurements.

3.1 NMR in medicine

Human-scale NMR imaging is generally known as magnetic resonance imaging (MRI) which has become a routine diagnostic tool. In the NMR imaging, spatially dependent magnetic fields with magnitude varying in a controlled fashion are deliberately applied, using specially designed gradient coils. In the presence of a magnetic field gradient, the NMR spectrum maps the density of nuclear spins along the gradient axis. If the gradients are known, one can easily work out from which part of the sample an NMR signal at a given frequency (Ω) comes from.

Usually three gradients along x, y and z-axis are imposed. An example of pulse sequence for NMR imaging is presented in Fig. 3.1.1 [91]. After the initial $\pi/2$ pulse for exciting the ensemble of the spins, there follows a variable evolution interval t_1 during which the gradient along x-axis (G_x) is applied. At time point when the gradient G_x is turned off, the gradient along y-axis (G_y) is turned on for the time interval t_2 during which NMR signal is acquired. The

corresponding offset frequencies (Ω^0 (1) and Ω^0 (2)) during t_1 and t_2 are given by:

$$\Omega^0 (1) = -\gamma G_x x \quad (3.1.1)$$

$$\Omega^0 (2) = -\gamma G_y \quad (3.1.1)$$

Here γ is a gyromagnetic ratio, and x, y are the spatial coordinates corresponding to the offset frequencies in the presence of the field gradients G_x and G_y. The position and thickness of the slice along the z-axis is set by adjusting the RF pulse frequency and the amplitude of the G_z gradient.

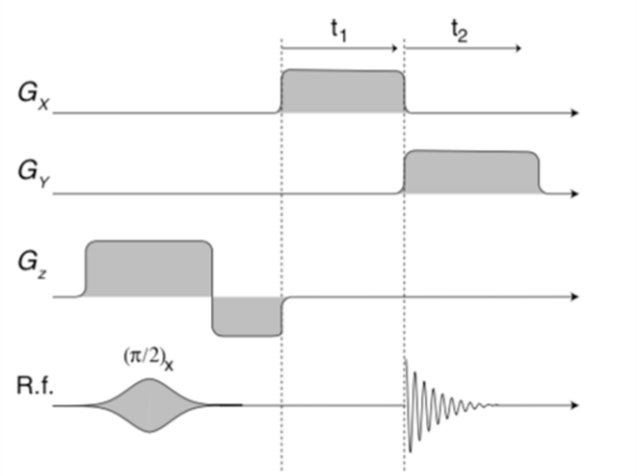

Fig. 3.1.1. Pulse sequence for NMR imaging of a slice through a three-dimensional object, perpendicular to the z-axis (adapted from M.H. Levit. [91])

In practice, more sophisticated procedures are implemented to give a faster, and more reliable performance. One of the MRI advantages is a good contrast between soft tissues which is created by differences in the strength of the NMR signal recovered from different locations within the body. This depends mainly upon the relative density of excited nuclei and on differences in their relaxation times (T_1, T_2). In clinical and research MRI, hydrogen atoms are most often used due to their natural abundance in human body. Contrast between tissues is often enhanced by using carefully designed pulse sequences [2, 3, 10-13] that are sensitive to T_1 or T_2, as well as the spin density or only to those spins which are present in a flowing liquid, such as blood.

Contrast agents (CAs) can be used to further improve the sensitivity and detection capability of MRI.

The contrast enhancement using contrast agents is obtained when one tissue has either stronger affinity for the CA or greater vascularity than another one. Diseased tissues, such as tumors, compared with healthy ones have a much higher uptake of the CA resulting in a better contrast. Since the intrinsic T_1 of tissues is much higher than T_2, the predominant effect at low doses of CA is the T_1 shortening [93, 94]. Thus, organs taking up such CAs will become brighter in T_1-weighted MRI sequence. The most commercially used CAs are paramagnetic Gadolinium-based chelates [4, 5, 53]. Paramagnetic gadolinium (III) ion which contains 7 unpaired electrons enhance proton relaxation and thus reduce the T_1 and T_2 of the surrounding protons. This leads to a greater difference between the tissue and the fluid affected by CA regarding relaxation times of the protons present therein.

The ability to choose different contrast mechanisms gives MRI a tremendous flexibility. An even more remarkable development of NMR in medicine is that besides structural information one can also produce NMR spectra at certain points in the body, and hence get a profile of metabolites. In the medical world this modality is generally known as magnetic resonance spectroscopy (MRS) or magnetic resonance spectroscopic imaging (MRSI) if a profile of metabolites is obtained from multiple voxels. NMR signals at different frequencies reveal the electronic and nuclear environment of the observed spins identifying chemical shifts between molecular species, while in MRI the differences in frequencies are used for space encoding.

In order to measure an NMR spectrum in-vivo, first, an anatomical MRI image is required for voxel localization. The voxel is acquired from a combination of slice selective excitations in 3 dimensions in space. The most commonly used volume selection sequences are Point RESolved Spectroscopy (PRESS) and STimulated Echo Acquisition Mode (STEAM) [95-98]. It is very important that the volume of interest (VOI) is selected in as homogeneous place as possible avoiding different tissues. On the other hand, the voxel can not be too small, because of the insufficient NMR signal. Since water signal is approximately four orders greater than the signal intensity of other visible metabolites, water suppression [99-101] together with volume selection sequences is required. Depending on the selected area, outer volume fat suppression might be also needed [98, 100]. As with NMR imaging, MRS sequences contain operator-selectable parameters (*TR* and *TE*) that act together with T_1 and T_2 to affect the size and shape of spectral lines. *TR* is a

repetition time between multiple excitations, and TE is an echo time between the center of the excitation pulse and the acquisition of signal (echo).

In prostate cancer, citrate (Cit) levels decrease (due to consumption of citrate to supply energy to proliferating cells), while choline (Cho) levels increase (corresponding to increased cell membrane synthesis) [102]. Therefore, a ratio of peak intensities of metabolites ((Cho + Cr)/Cit) is used to indicate possible cancer [103, 104].

Due to some technical challenges, low concentration of metabolites or the presence of overlapping spectra lines, the MRS spectra can be difficult to interpret or even misleading without carefully analysis. Another way to analyze chemical composition of tissues is to use high resolution solid-state NMR spectroscopy of samples from needle biopsy [105, 106].

3.2 Solid state NMR

The benefits of solid-state NMR made it a powerful tool for analysis of materials that are important technologically, biomedically and from the fundamental-science standpoint [107-110 and references therein]. Comparing to liquids, solid state NMR experiments generally result in broader and more complex spectral lines, whose frequency and intensity profiles reflect the orientational distributions of molecules in the sample.

In a solution, due to rapid isotropic motions of molecules, the orientational dependence of nuclear magnetic interaction is efficiently averaging out and only the isotropic component is detectable. However, in a solid, the motion of molecules is heavily restricted and anisotropic spin interactions are not averaged out. As an example, let's take a single crystal where molecules are lined up and have the same orientation. In such case, the chemical shift is the same for all molecules and depends on the orientation of the crystal with respect to the magnetic field. As a result, if the crystal is rotated, the chemical shift is changed. In a powder, the molecules are orientated in all possible directions. Each crystallite with a different orientation corresponds to different frequency. The superposition of all these peaks result in a spectrum of a typical broad shape, which is called "powder pattern".

The orientation dependence of the anisotropic interactions may be eliminated or reduced by a significant molecular motion. Mechanical sample rotation modulates the anisotropic spin interactions (quadrupole couplings, chemical shift anisotropies and direct dipole–dipole couplings) and is typically on the spectral time-scale. This is achieved by using magic angle spinning

(MAS). The approach is illustrated in Fig. 3.2.1. [109]. The sample is rotated rapidly around an axis of 54.74° with respect to the static magnetic field. In practice, typical MAS frequencies range from a few hundreds of hertz up to around 70 kHz [91]. The highest currently attainable frequency in 2019 is 126 kHz [110]. Depending on the MAS frequency, a particular interaction can be averaged out either partially or completely. If the frequency is not sufficiently large compared with shift anisotropies, the spectrum contains extra peaks called spinning sidebands. If the spinning frequency is large enough, it possible to obtain solid-state NMR spectrum with a resolution approaching that obtained in a liquid sample. However, highly resolved spectrum is achieved at the expense of losing the orientational dependence and hence a valuable information on structure and dynamics.

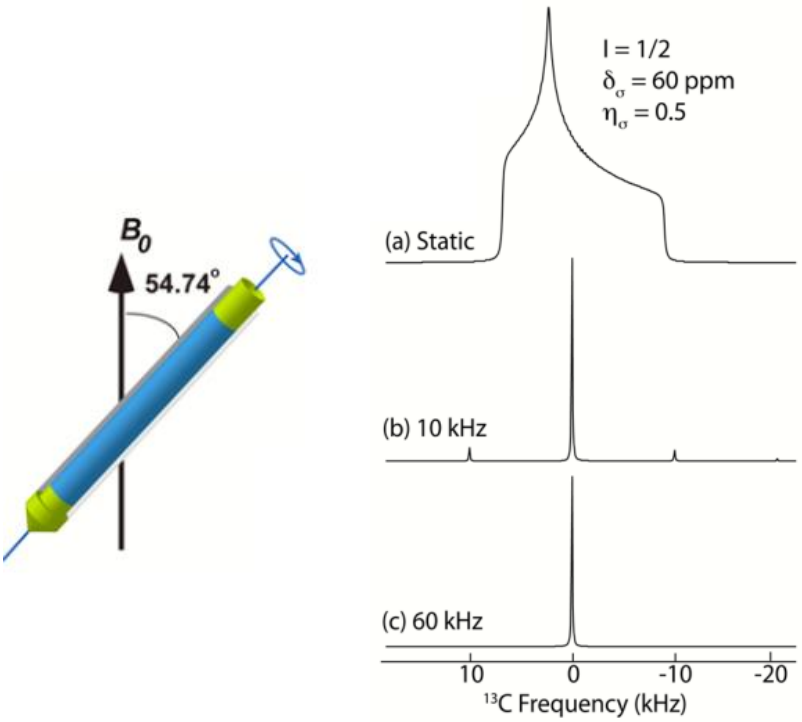

Fig. 3.2.1 An example of the effect of MAS on NMR line shapes in a spin-1/2 nucleus (δ_0 - anisotropy, η_0 - asymmetry), a) powder pattern in a static sample, b) a line shape broken up into a series of spinning sidebands at spinning at low frequency, c) an isotropic peak due to averaging out the anisotropic interaction (adapted from T. Polenova et al. [109])

3.3 2D NMR spectroscopy

Modern two-dimensional NMR spectroscopy is an essential tool for assigning NMR peaks of complex molecules [111]. If the compounds are known, chemical shift values may provide some clues. However, in many cases, chemical shifts do not provide an unambiguous answer. 2D NMR studies can be classified into homonuclear correlation studies and heteronuclear correlation studies. Homonuclear studies show peak correlations between similar nuclei, like proton-proton, while heteronuclear studies seek to identify correlations between two dissimilar nuclei, such as ^{13}C and ^{1}H or ^{15}N and ^{1}H. There are four steps in any 2D NMR experiment: preparation, evolution, mixing and detection. During the first period, called the preparation time, the sample is excited by one or more pulses. The resulting magnetization is allowed to evolve for the time period t_1. Then another period follows called the mixing time, which consists of a further pulse or pulses. After the mixing period the signal is recorded as a function of the time variable t_2 [112, 113]. Recording a two-dimensional data set involves repeating a pulse sequence for increasing values of t_1 and recording a free induction decay as a function of t_2 for each value of t_1 (Fig. 3.3.1).

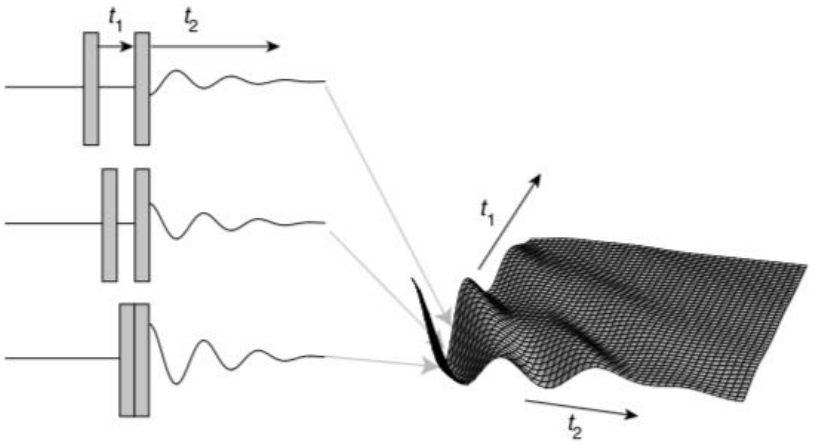

Fig. 3.3.1. Compilation of two-dimensional correlation spectra acquisition (redrawn from M.H. Levit [91])

The information content of 2D NMR spectrum is determined by the pulse sequence. In practice a combination of correlation spectra is useful. The simplest homonuclear 2D NMR experiment is COSY (Correlation

Spectroscopy). The pulse sequence contains just two π/2 pulses, separated by a variable delay t_1. The object of COSY is to discover the network of J-couplings in a molecule and so to arrive at spectral assignments. In ^{1}H-NMR case it helps to distinguish overlapping spectral lines determining which resonance corresponds to which proton. HMQC (Heteronuclear Multiple Quantum Correlation) experiment has the same function as COSY but correlates heteronuclear instead of homonuclear pairs of J-coupled spins, such as ^{1}H and ^{13}C, which are attached to each other (one bond correlation). Usually the acquired information about which proton is attached to which carbon is not enough for assigning all ^{13}C-NMR peaks and HMBC (Heteronuclear Multiple Bond Correlation) experiment is needed. HNBC spectroscopy is suitable for determining long-range connectivities. In this case, it provides information about the chemical shifts of carbon atoms that are 2-3 bonds away from the proton to which they correlate. Assigning NMR peaks may give knowledge of molecular structure, function, and dynamics, thus 2D NMR spectroscopy is one of the foremost contemporary tools in NMR experiments.

3.4 NMR relaxometry: spin-lattice relaxation

Relaxation is the process by which nuclear spins return to their thermal equilibrium following some disturbance created by RF pulses. Reaching a state of thermal equilibrium implies that the populations are given by the Boltzmann distribution, at the temperature of the molecular environment and that all coherences are absent. There are two types of relaxation processes. Spin-lattice relaxation (T_1), also known as longitudinal relaxation, is concerned with the movement of spin populations back to their Boltzmann distribution values. Spin-spin relaxation (T_2), also known as transverse relaxation, is concerned with decay of transverse magnetization. Relaxation measurements can be useful for motional studies as well as for structural investigations. In this dissertation, T_1 measurements were used for analyzing the effectiveness of UCNPs as novel MRI contrast agents.

Comparing the effectiveness of contrast agents, relaxivity (r_1) is the main parameter. It is defined as the slope of a plot of relaxation rate ($1/T_1$) versus concentration of contrast agent (CA):

$$\frac{1}{T_1} = \frac{1}{T_{10}} + r_1 C \qquad (3.4.1)$$

Here T_{10} is the relaxation time of the sample in the absence of the contrast agent and C is the concentration of CA (mM).

For spins-1/2, relaxation is caused by fluctuating magnetic fields at the sites of the nuclear spins, caused by thermal motion of the molecules. There are different sources of local magnetic fields, but in most experimental cases a single relaxation mechanism dominates. For spins-1/2 it is usually dipole-dipole mechanism.

The relaxation mechanism of electron-nuclear magnetic interaction in paramagnetic systems is usually explained by Solomom-Bloembergen-Morgan (SBM) model using three sub-systems (Fig. 3.4.1) [53, 114]: the water molecules that bind directly to the gadolinium ion forming the first coordination shell, water molecules with protons that make up the long lived second coordination shell and water molecules that move in the bulk. For the MRI contrast agents, a simpler SBM model of two spheres is more often used [115]. Such relaxation mechanism, including inner-sphere and outer-sphere components, is used in this dissertation as well.

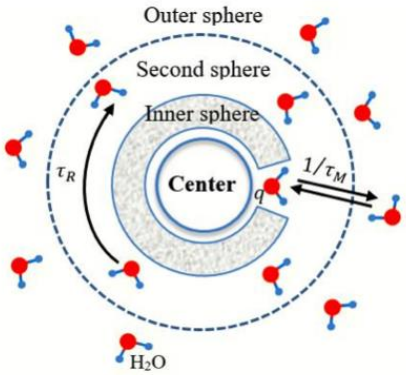

Fig. 3.4.1 Inner sphere, secondary sphere, and outer sphere of the Solomom Bloembergen-Morgan (SBM) relaxation model [53, 116]

The longitudinal relaxation rate ($1/T_1^{dip}$) that takes place in the first sub-system is described by spin-electron interaction given by Eq. (3.4.2) [53]:

$$\frac{1}{T_1^{dip}} = R_1^{dip} = \frac{2}{15} \cdot \frac{\gamma_I^2 g^2 \mu_B^2 S(S+1)}{r_{GdH}^6} \left(\frac{\mu_0}{4\pi}\right)^2 \cdot \left[\frac{3\tau_{c1}}{1+\omega_I^2\tau_{c1}^2} + \frac{7\tau_{c2}}{1+\omega_S^2\tau_{c2}^2}\right] \quad (3.4.2)$$

Here, S is the electron spin quantum number, γ_I is the nuclear gyromagnetic ratio, g is the electron g-factor, μ_B is the Bohr magneton, r_{GdH} is the distance between Gd^{3+} and the water proton, μ_0 is the magnetic permeability of a

vacuum, ω_I and ω_S are the nuclear and electron Larmor frequencies, τ_{c1} and τ_{c2} are the correlation times of nuclear and electron motion, respectively.

On the basis of the SBM theory, common strategies for enhancing spin lattice relaxivity mainly include increasing the number of bound water molecules (q), enhancing rotational correlation time (τ_R) and optimizing water residence time (τ_M). Higher τ_R values imply slower molecular tumbling and lead to increased proton relaxivity. τ_M is the inverse of water exchange rate in the inner sphere [116].

The standard pulse sequence for measuring spin-lattice relaxation times is inversion recovery. First, a 180° pulse is applied, thereby inverting the magnetization (M) along the z-axis. Then a delay τ is left for the magnetization to relax and finally, a 90° pulse is applied so that the size of the z-magnetization ($M(\tau)$), can be measured [113]. The whole process is repeated for different values of τ in order to map out the recovery of the inverted magnetization. The example is later shown in chapter 5.2.1 discussing the results (Fig. 5.2.2). Performing such an experiment, the first step is to determine the ^{1}H 90° transmitter pulse. The spectrometer acquires and processes a chosen number of experiments with different pulse length. The defined spectral region for each experiment is plotted side-by-side in one graph (Fig. 3.4.2). The spectrum with the highest intensity coresponds to the length of the 90° pulse for protons of interest. To obtain a more accurate 90° pulse measurement, it is common to find the 180° pulse length at zero crossing and divide the determined pulse value by 2.

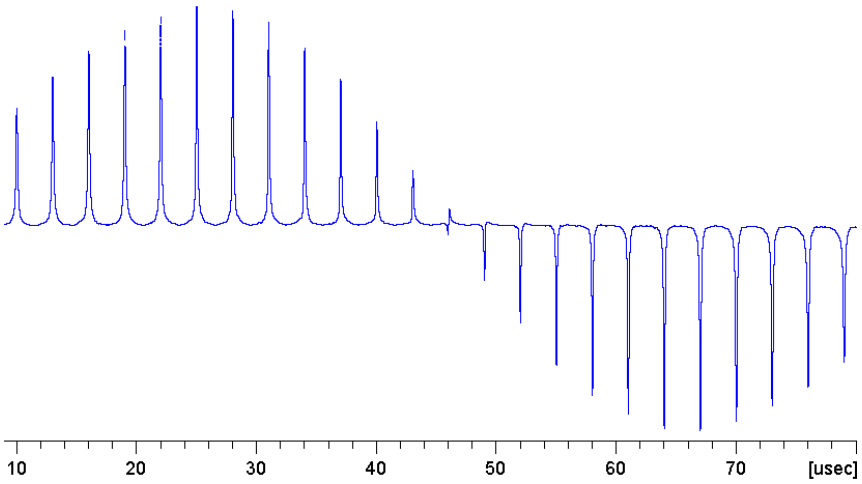

Fig. 3.4.2 Example of NMR experiment for the determination of ^{1}H 90° transmitter pulse

3.5 NMR Diffusion

Another information-rich parameter that can be obtained through specialized NMR experiment is diffusion constant. The study of molecular diffusion by NMR is large and important field. Diffusion is a random and uncoordinated translational motion of molecules. It affects the NMR properties in microscopic and macroscopic way. On microscopic scale, it averages out short-range intermolecular spin interactions. On macroscopic scale, it affects the behavior of spins if the external inhomogeneous magnetic field is generated. The motion of the molecules along the direction of the gradient changes the Larmor frequency and hence it can be used to quantitate the molecular diffusion. Relationship between diffusion coefficient and rotational correlation time (τ_R) is shown in Eg. (3.5.1):

$$\tau_{\mathrm{R}} = \frac{3}{2D} \tag{3.5.1}$$

Three-pulse *stimulated echo* sequence, is one of the basic pulse sequences used to measure molecular diffusion. Between the first two π/2 pulses, there is evolution of transverse magnetization in the presence of a field gradient. Molecular diffusion takes place between second and third pulses. This interval (Δ) is relatively long, typically 50-200 ms, in order to allow the motional process to occur. Another gradient pulse refocuses the signal. The greater the displacement of the spins during Δ due to diffusion, the less refocused the signal and the more reduced the intensity of the signal. Intensity of NMR signal is proportional to the diffusion coefficient (*D*) in the gradient direction as in Eq. (3.5.2):

$$I \sim exp\left[-(\gamma G\delta)^2 D\left(\Delta - \frac{\delta}{3}\right)\right], \tag{3.5.2}$$

Either a time delay between pulses (Δ), or the gradient length (δ) as well as its strength (*G*) can be incremented. In a typical experiment, the software creates a series of values of *G*, ranging from 95% to 2% of the maximum gradient strength. Plotting *I* vs *G* for a given peak then gives a diffusion curve (Fig. 3.5.1). If the intensity reduction is insufficient or too strong, the diffusion time (Δ) and/or the length of the gradient pulse (δ) must be adjusted. When all the constants are known, the diffusion coefficient can be easily calculated using the slope of the intensity dependence on the squared gradient strength.

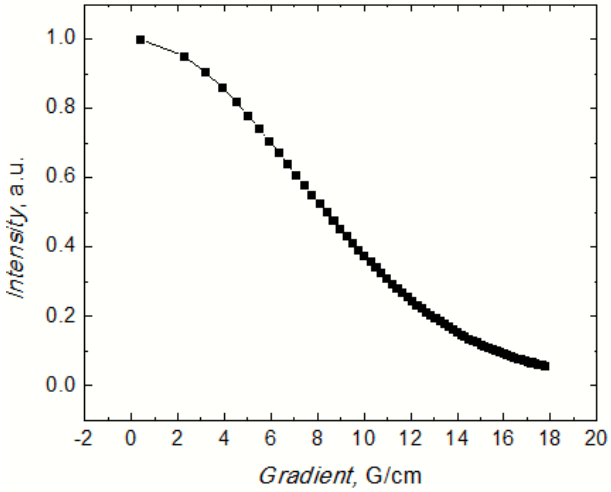

Fig. 3.5.1 An example of a diffusion curve using three-pulse stimulated echo sequence for the NMR diffusion experiment. The gradient strength is incremented from 2% to 95% in 64 steps

If the experiment is repeated with gradient pulses in the three different directions, it is possible to estimate the three diffusion constants $\{D_X, D_Y, D_Z\}$ individually. In an anisotropic medium, such as many body tissues, these constants are not the same. By studying the directions of the fastest diffusion for neighbouring volume elements in an NMR image, it is possible to trace out the pathways of nerves and similar channel-like structures in the human body. This technique is called diffusion tensor imaging [91, 13, 44, 45].

In this dissertation, NMR diffusion measurements were used together with NMR relaxometry for UCNPs analysis. Spin-lattice relaxation rate ($R_1=1/T_1$) of a nuclear spin that interacts with unpaired electron spin of a paramagnetic ion is proportional to the inverse sixth power of the distance between the water proton and paramagnetic ion. This is why processes around the surface of the NPs are at the first importance. Water molecules that are directly coordinated to the paramagnetic center are responsible for the inner sphere relaxation contribution, while bulk water molecules in the nearby environment affect outer sphere relaxation. When surfactant molecules are used, they interact with water, hence diffusion of water molecules must decelerate. This is the reason why diffusion measurements as well as T_1 measurements can give fundamental details of such system when effectiveness of MRI contrast agent is concerned.

4. EXPERIMENTAL DETAILS

4.1 Materials

The preparation of four types of materials analyzed in this dissertation is presented in a forthcoming part of this chapter. The topic includes: metabolites present in prostate, up-converting nanoparticles (UCNPs), sunset yellow (SSY) as a lyotropic chromonic liquid crystal (LCLC) and calcium hydroxyapatites (CaHAs).

4.1.1 Metabolites in prostate

All samples were prepared in Vilnius University Life Sciences Center, Institute of Biotechnology, Department of Biothermodynamics and Drug Design. In order to control pH, sodium citrate and citric acid buffer was prepared. The metabolites were dissolved in water as well as in deuterated water separately. Then, using these solutions, the final samples were prepared containing the following metabolites at physiological concentrations as reported in healthy human prostate [35]: citrate (Cit, 50mM), creatine (Cr, 5mM), choline (Cho, 1mM), spermine (Spm, 6 mM) and 200 mM of sodium formate for scaling. DSS (4,4 - dimethyl - 4- silapentane - 1 - sulfonic acid) as NMR standard was used in capillary for water solutions, or directly dissolved in deuterated water solutions (1 mM).

For NMR experiments, 600 µl of deuterated water solutions and 500 µl of water solutions of metabolites with capillary insert were placed in standard 5 mm Bruker tubes. For MRS measurements, a homemade phantom was prepared: four 50ml tubes were filled with water solutions of metabolites and emerged in 3 l water tank (Fig. 4.1.1). The immobilization of the samples was ensured.

Fig. 4.1.1 An example of 5 mm tube with a Bruker spinner for measuring ^{1}H-NMR spectroscopy (left) and two projections of four 50 ml tubes of metabolites solutions in the 3l water container as MRS phantom (right)

To ensure the exact concentration of metabolites, all solutions were prepared using micropipettes and high-accuracy weighting scales. Digital pH-meter was used for measuring exact pH values of the solutions. Samples were stored at +4C.

4.1.2 Upconverting nanoparticles

Upconverting nanoparticles (UCNPs) were synthesized via a thermal decomposition method. Detailed synthesis route is published in the co-authors article [117]. Hexagonal phase β-$NaGdF_4$ was chosen as host lattice for its ability to combine optical and magnetic properties [118]. Aqueous solutions of two types of nanoparticles were analyzed: core and core-shell UCNPs. Unless stated otherwise, Ytterbium (Yb) and Erbium (Er) doped $NaGdF_4$ nanoparticles were used as a core. Optical inert layer of $NaGdF_4$ was chosen as a coating for core-shell NPs. Both kinds of hydrophobic UCNPs were converted into hydrophilic ones using a nonionic surfactant polysorbate 80 (TWEEN80, polyoxyethylene sorbitan laurate). TWEEN80 was used to make the UCNPs colloidally stable and dispersible in water while protecting the surface from non-specific adsorption of biomolecules. In some cases, excess of surfactant TWEEN80 was removed using centrifugation.

For calculation of relaxivities, at least 4 different concentrations of each CA were measured. The mean diameter of studied core and core–shell nanoparticles varied in a range from 12 to 70 nm, but the most detailed analysis was made for 12 nm core ($NaGdF_4$:Yb,Er) and 19 nm core-shell ($NaGdF_4$:Yb,Er@$NaGdF_4$) nanoparticles. The size of these nanoparticles was confirmed by transmission electron microscopy (TEM). Experiments were carried out using high resolution (maximum resolution: 0.63 Å) transmission electron microscope HRTEM Jeol ARM 200F in NanoBioMedical center, AMU, Poznan. The corresponding TEM images are shown in appendix.

For the comparison, Gadovist (1mmol/ml) also known as Gd-DO3A-butrol ($C_{18}H_{31}GdN_4O_9$) was analyzed as a commercial MRI contrast agent. All samples were placed in standard 5 mm NMR tubes for NMR experiments. Ceramic *Bruker* spinner was used for the temperature dependence measurements.

4.1.3 Sunset Yellow FCF

The commercial Sunset Yellow FCF (SSY) was used from abcr GmbH, Karlsruhe, Germany (www.abcr.de), of 90% purity. The water used was freshly bidistilled. For concentration dependence measurements, the samples

were prepared using micropipette and high-accuracy weighting scales during the preparation to ensure the exact concentration. Then, the samples were placed in standard, 5 or 10 mm, NMR tubes for NMR experiments. The concentrations were chosen according to the phase diagram of SSY to observe all phase transitions in the temperature range from 25 up to 95°C. For measurements at such high temperatures, ceramic Bruker spinner was used. The samples of 0.6−1 mL volume were tightly closed to avoid any changes in composition. No changes in the sample weights were observed after long-lasting experiments at varying temperature.

4.1.4 Calcium hydroxyapatite

The nano-structured calcium hydroxyapatites (CaHAs) were derived in Vilnius University, faculty of Chemistry and Geoscience, department of Inorganic Chemistry applying the sol-gel synthesis routes. Ethylene glycol (EG) and tartaric acid (TA) were used as complexing agents. The water used was deionized and freshly triple-distilled. Detailed steps and conditions are presented in references [119, 120]. The commercial nano-structured CaHA was used from Aldrich, synthetic, 99.999%. All materials were characterized by scanning electron microscopy (SEM) and energy-dispersive X-ray analysis (EDX) using a Helios NanoLab 650 scanning electron microscope coupled with energy-dispersive X-ray spectrometry system, etc. [107, 121].

The samples containing water confined in nano-structured CaHAs (each in amount of ca 2 mg) were mixed in the ratio of 1:100 with KBr powder and pressed into a pellet using 10 tons pressing of manually operated hydraulic press Specac.

4.2 Experimental setup

MRS measurements were performed in Vilnius University Santaros Klinikos (VULSK), center of Radiology, Nuclear Medicine and Medical Physics using 3 T Philips MR scanner operating at 128 MHz for ^{1}H. All other NMR experiments were carried out in Vilnius University, faculty of Physics, institute of Chemical Physics (VU, FF, ChFI) using Bruker AVANCE III HD spectrometer operating at the resonance frequencies of 400 and 40 MHz for ^{1}H and ^{15}N, respectively (magnetic field of 9.4 T). For comparison, additional NMR relaxometry experiments were performed in Adam Mickiewicz University in Poznan, NanoBioMedical center using homemade spectrometer operating at resonance frequency of 16 MHz (magnetic field of 0.4 T).

Prostate MRS was performed using SV-PRESS-144 pulse sequence for single voxel localization. Time of repetition (TR) was 1500 ms, echo time (TE) was 144 ms, the size of voxel was 12x12x12 mm^3 and 112 scans were accumulated (NSA). Since the size of voxel was smaller than 20x20x20 mm^3, iterative shimming was used, even if it took more time during the pre-acquisition. Basing pulse was added to water suppression pulse sequence for additional water suppression of residual water. MRS spectra were processed using Philips *SpectroView* package. Due to limited accessibility to spectral data, a custom-made script for Python programing language as well as Microcal Origin 9 package were used for additional spectra analysis and graphical representation.

One-dimensional ^{1}H-NMR spectra of aqueous solutions were measured using zg pulse sequence. The 90° pulse length was set at 25 μs and up to 1024 scans were accumulated depending on the experiment. Repetition delay was set to 2 s. Unless stated otherwise, the spectral width was 20 ppm with 96 152 points as the size of FID. The temperature in a probe was controlled with an accuracy of ±0.2 deg.

The heteronuclear ^{1}H–^{15}N correlation spectrum was acquired using the multiple-bond *J*-coupling pulse sequence (HMBC experiment) with the additional pulses for the coherence selection. The experiment was acquired with 256 points in the channel F1 and 16 000 points at the channel F2 with the repetition delay of 2 s. The number of scans NS = 80 was found to be appropriate to accumulate enough intense signals of nitromethane (reference) as well as SSY $\geq$ 0.7 mol/kg in water solutions.

For T_1 measurements an inversion-recovery pulse sequence was employed using 16 increments with 2 scans each and the repetition delay was set to $5T_1$. The 90° pulse length was approximately 24 μs and was adjusted for each experiment. For calculation of relaxivities, at least 4 different concentrations of each CA were measured.

A pseudo-2D diffusion experiments were carried out using stimulated echo sequence with two gradient pulses and one spoil gradient. The gradient strength was incremented from 2% to 95% in 64 steps. The diffusion time (Δ) and diffusion gradient length (δ) were 130 ms and 2 ms respectively.

All MAS (magic angle spinning) measurements were performed using Bruker 4 mm H/ X CP-MAS probe-head, which is capable to spin the sample up to 15 kHz rate. NMR MAS spinning rate was set to 10 kHz. For all ^{1}H MAS experiments the 90° pulse length was 2.5 μs and 64 scans were accumulated with a repetition delay of 3 s.

The signal of 4,4-dimethyl-4-silapentane-1-sulfonic acid in the D_2O solution in a capillary insert was used as the reference. The D_2O in the same capillary insert was used for locking. The ^{15}N NMR spectra were referred with respect to CH_3NO_2, also in the capillary insert. All NMR spectra were processed using Topsin 3.2 software. Additional spectra analysis and graphical representation were done using Microcal Origin 9 package.

5. RESULTS AND DISCUSSION

5.1 NMR spectroscopy of metabolites

MRS procedure in VULSK is most frequently used as complimentary technique to prostate MRI. As mentioned in the methodology section, so far, the ratio of prostate metabolites ((Cho + Cr)/Cit) in MRS is the main indicator for malignant tissue. However, getting a good quality spectrum is difficult. Due to poor signal-to-noise ratio (SNR) as well as overlapped spectral lines, some intensities of NMR peaks, like the one of creatine, can be insufficient to be evaluated.

An example of multivoxel prostate MRS is presented in Fig. 5.1.1. Spectra were processed using Philips *SpectroView* package, which automatically calculates the ratio of checked metabolites after the fitting procedure (blue spectra). Ratio can be calculated using the integral or the intensity of NMR peaks. In this case, spectra from two voxels, (3,2) and (4,3), were analyzed. Even without knowing the exact value of (Cho + Cr)/Cit ratios, it can be seen, that the tissue from voxel (3,2) is potentially malignant and the tissue from the voxel (4,3) is potentially healthy. However, in both cases the signal of creatine can not be evaluated and thus, the program calculated only the ratios of Cho/Cit.

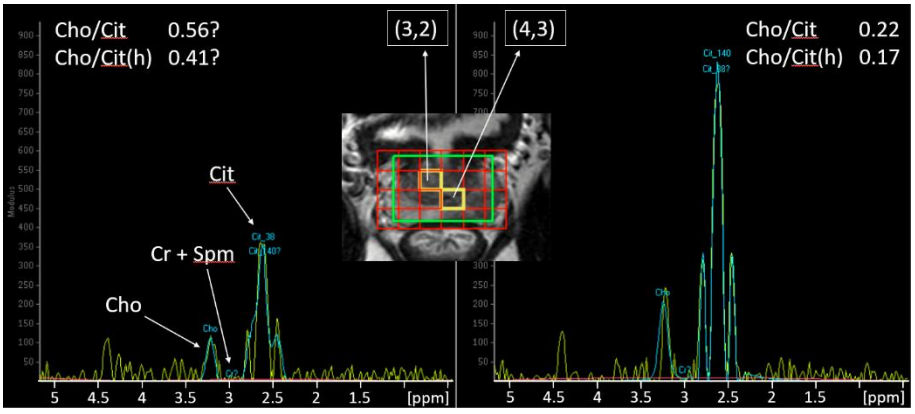

Fig. 5.1.1 An example of multivoxel prostate MRS performed in VULSK. Spectra from two voxels is presented using Philips SpectroView package: on the left – spectrum obtained from voxel (3,2) and on the right – spectrum obtained from voxel (4,3). Two ratios of metabolites were calculated: Cho/Cit presents ratio of integrals of choline and citrate NMR peaks, Cho/Cit(h) – ratio of intensities (height) of the same NMR peaks

The quality of NMR spectra obtained using prostate MRS technique in VULSK is usually poorer than in the shown example above. Thus, methods leading to a better quality of MRS modality are a highly required. For that reason, the solutions of metabolites were firstly analyzed using high resolution ^{1}H-NMR in VU ChFI. The results were later applied to study the methods of sample preparation for MRS measurements. After optimizing the scanning parameters for single-voxel (SV) MRS, a homemade phantom was prepared for further evaluation of MRS in clinics.

5.1.1 High resolution ^{1}H-NMR spectroscopy

Most of the metabolites with their spectral information can be found in various databases, such as http://www.hmdb.ca, which provides search facilities that allow the identification of known metabolites. However, even if a metabolite is confidently identified, it can sometimes still be important to further confirm the identification [35, 122]. In order to accomplish that, first of all, each metabolite (citrate (Cit), spermine (Spm), choline (Cho) and creatine (Cr)) was dissolved in water and measured separately.

According to the literature, the extracellular pH of solid tumors is more acidic in comparison to normal tissue [123, 124]. Tumor acidity is a consequence of high rates of glucose metabolism, combined with poor perfusion. For that reason, aqueous solutions containing all four metabolites were prepared with different pH: one with pH = 6 and another one with pH = 7 imitating malignant and healthy tissue respectively. Deuterated water was used as a solvent in order to reduce the influence of water signal on the spectrum of metabolites. An expansion of all ^{1}H-NMR spectra of the prepared samples is shown in Fig. 5.1.2. Comparing the spectra, it was seen that chemical shifts of metabolites which were measured separately (four spectra from the bottom) match the chemical shifts of solutions containing all metabolites (two spectra from the top). The only exception was citrate. In solutions with two different pH, chemical shift of citrate also differed. Signal of DSS was used as the reference (0 ppm). All chemical shifts of metabolites are summarized in table 5.1.1. Chemical shifts of NMR peaks with highest intensities (written in bold) are assigned to atoms shown in Fig. 5.1.3. The assigned chemical shifts and number of peaks in multiples were in great agreement with the 500 MHz ^{1}H-NMR results presented in database of human metabolites http://www.hmdb.ca. Only some minor peaks of spermine were difficult to distinguish.

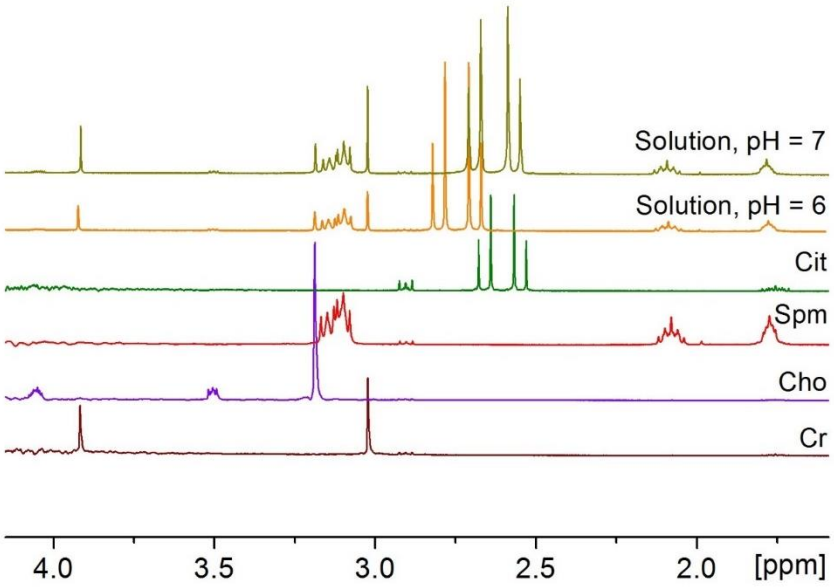

Fig. 5.1.2 An expansion of 400 MHz ^{1}H NMR spectra of prostate metabolites. First two spectra from the top correspond to deuterated water solutions with different pH containing all the studied metabolites: citrate (Cit), spermine (Spm), choline (Cho), creatine (Cr). The other four below present spectra of water solutions each containing different metabolite

Table 5.1.1. ^{1}H NMR spectral lines assignment in the solutions of prostate metabolites (400 MHz, pH = 7).

Metabolite	Chemical formula	δ ^{1}H (ppm) and multiplicity*	Assignment (Moieties)
Citrate	$C_6H_8O_7$	**2.55 (dd):** 2.62 (d), 2.48 (d)	CH_2, CH_2
Spermine	$C_{10}H_{26}N_4$	**3.12 (m)**, 2.08 (m), 1.77 (m)	NCH_2, NCH_2, NCH_2
Choline	$C_5H_{14}NO$	4.06 (m), 3.51 (m), **3.19 (s)**	OCH_2, NCH_2, $N(CH_3)_3$
Creatine	$C_4H_9N_3O_2$	3.92 (s), **3, 02 (s)**	CH_2, CH_3

**s- singlet, d- doublet, dd – doublet of doublets, m – multiplet of more than 5 peaks. Chemical shifts written in bold are used for evaluation of metabolic profiles in MRS.*

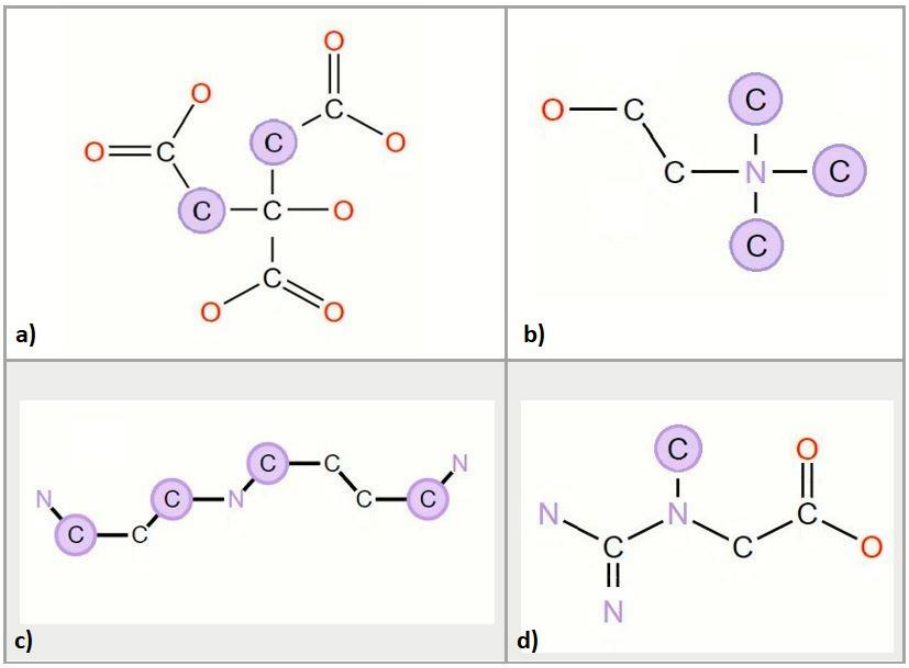

Fig. 5.1.3 Chemical structures of main prostate metabolites: a) citrate, b) choline, c) spermine, d) creatine. The marked atoms correspond to chemical shifts of NMR peaks with highest intensities. (In table 5.1.1 these chemical shifts are written in bold). Pictures adapted from http://www.hmdb.ca

The relationship between pH and changes in chemical shift of citrate was analyzed in more detail. Nine aqueous solutions of citrate with different pH were prepared. The value of pH varied from 4.9 to 7.1. The step of variation was around 0.3. It was not very constant, because even a tiny amount of citric acid changed the pH drastically.

The results of pH dependence are presented in figure 5.1.4. Difference in pH of the sample had a significant influence on citrate. Chemical shift of the middle point of the doublets shifted from 2.67 to 2.55 ppm and the distance between doublets increased from 0.06 to 0.10 ppm when pH of the solution was increased.

Finally, the influence of temperature was evaluated. Measurements of aqueous solutions were started at room temperature (25 ºC) and repeated at each 5 deg till the temperature reached 40 ºC. Since the temperature of human body is around 37 ºC, measurements at higher temperatures were not needed. The idea of these experiments was to check if spectroscopic results are

sensitive to small changes in temperature. In human body temperature may slightly vary and it can not be controlled. Hence, a temperature dependence would cause some difficulties performing NMR spectroscopy in-vivo. However, no significant effect was noticed.

Having all metabolites identified and analyzed, next step was to apply the obtained results in clinics using MRI scanner.

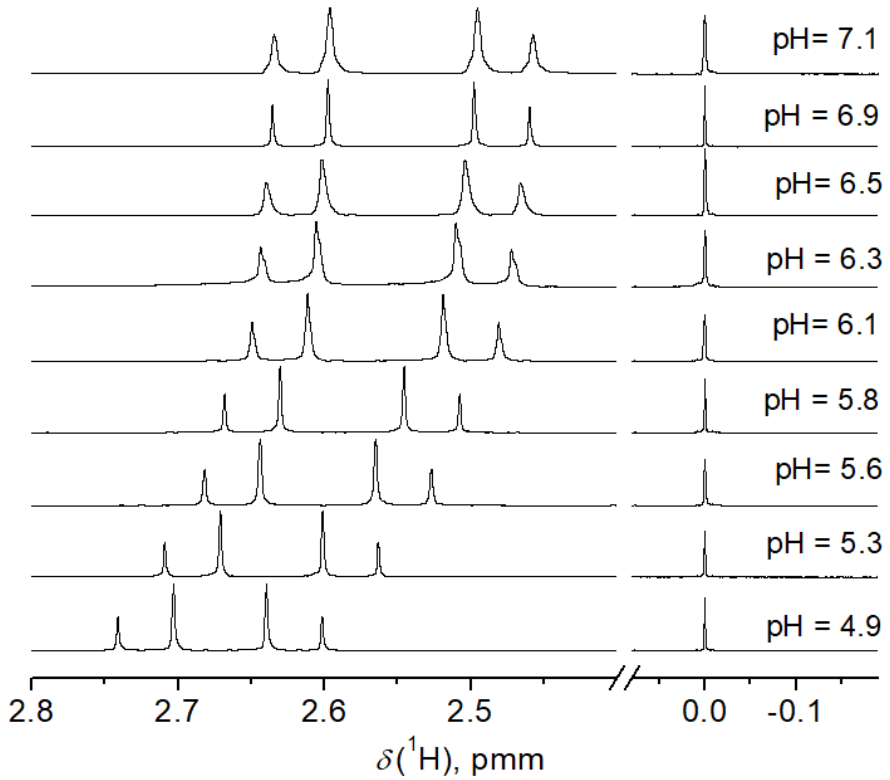

Fig. 5.1.4 An expansion of 400 MHz ^{1}H NMR spectra of citrate (Cit) in water solutions with different pH (DSS at 0 ppm)

5.1.2 MRS measurements in-vivo

First of all, methods for sample preparation were investigated, such as size of sample, effects of its surroundings as well as size and location of the volume of interest (VOI) - voxel. Five different volume containers of the same samples were prepared. Firstly, each metabolite was analyzed separately, as it was done for high resolution NMR experiments

A great amount of MRS experiments were performed changing the size and the location of the voxel in one sample under the same scanning parameters. The measurements of the same solutions were repeated in different volume containers. It was demonstrated that the size of the voxel strongly depends on the size of the sample. Having a large container (at least three times larger than voxel), despite low SNR, NMR peaks still could be distinguished even from a voxel as small as 5x5x5 mm^3, if it was centered. It was also noticed that the closer to the edge the voxel gets, the worse quality of the signal appears. As an example, even if the voxel is large enough, the quality of spectrum might be poor (low SNR, insufficient water suppression) if the size of the voxel becomes comparable to the size of the container. Few examples of mentioned measurements are presented in Fig. 5.1.5 and 5.1.6.

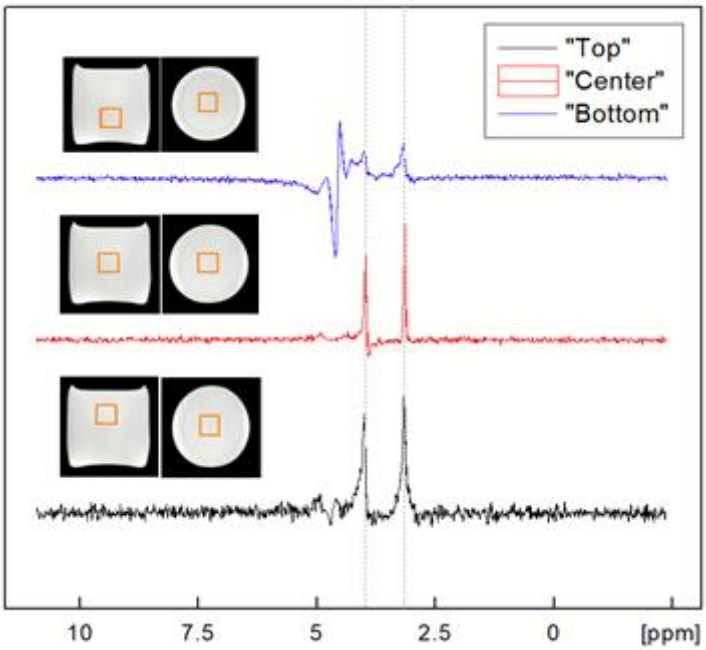

Fig. 5.1.5 128 MHz ^{1}H-NMR spectra of creatine measured using SV MRS procedure. Three spectra were obtained from different locations of the voxel – top, bottom and center of the same sample (see MRI images). The size of the voxel (12x12x12 mm^3) was kept unchanged as well as the scanning parameters (see chapter 4.2). MRI images show two projections of the cylindrically shaped container filled with creatine solution are shown. Note, that when the voxel was at the bottom of the sample ("Bottom" blue spectrum), the water suppression was the poorest, hence a residual peak of water is seen

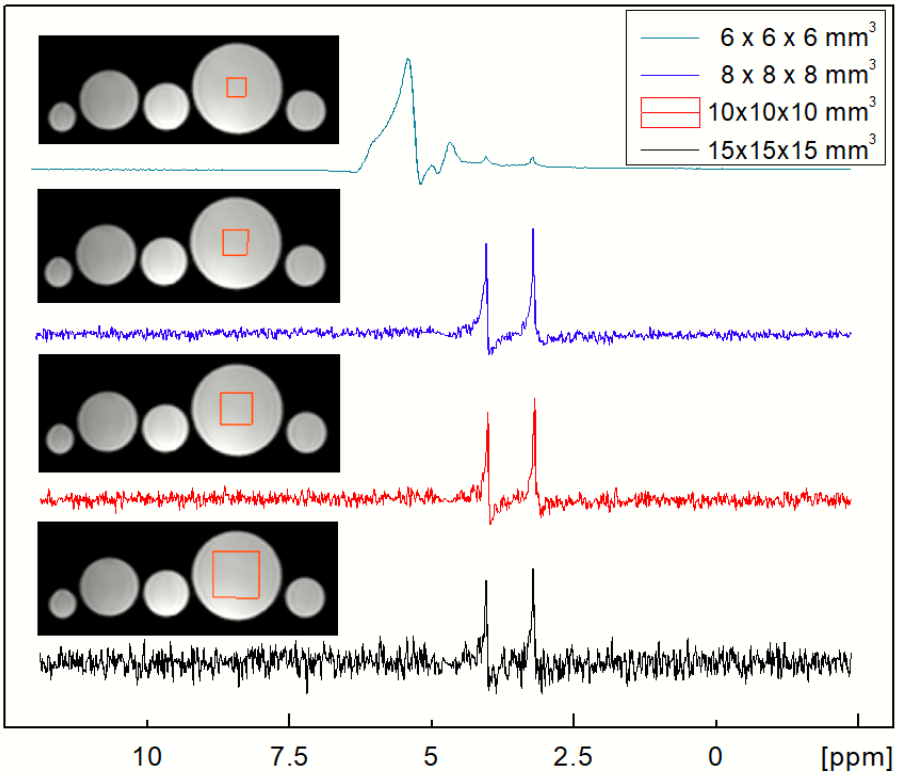

Fig. 5.1.6 128 MHz ^{1}H-NMR spectra of creatine measured using SV MRS procedure. Four spectra obtained from different sized voxel (see the legend) localized in the center of the largest container (see MRI images) are presented

Using Philips *SpectroView* package spectra can be saved only as a picture, like in Fig. 5.1.1. In order to be able to analyze spectral data using other programs such as Microcal Origin 9 package, a custom-made Python3 script was written. Since it reads pixels, the resolution of such spectra is decreased and depends on how zoomed the spectra was before saving it as a picture. Despite that, the quality is good enough for the comparison of the spectra.

From the experiments above, it can be noted that the voxel should be localized in center and its size should be chosen according to the size of the sample – not too big, in order to be further from the edge, and not too small – in order to get a sufficient signal-to-noise ratio. All the experiments mentioned above were done performing MRS on the samples surrounded by air.

Next, the same samples were immersed in a tank of water. The most challenging task was to construct a model in such a way, so that there would

not be any unwanted movement. Using *Philips* Monitoring Display Operating Console, it was noticed that the shimming procedure was much better compared to the one when the samples were surrounded just by air. Hence, the quality of NMR spectra of metabolites measured under the same conditions were as well better (higher SNR, narrower spectral lines). Scanning parameters, such as TR and TE times, NSA, shimming or water suppression techniques, as well as methods for outer volume suppression were also analyzed. However, the standard parameters (see chapter 4.2) seemed to be optimal regarding spectra quality (SNR, FMHM, water suppression) and time consumption.

Considering the results, a homemade phantom was prepared as described in chapter 4.1.1. Phantom testing for quality control remains one of the key techniques for achieving reproducible and accurate MRS results [125]. For further measurements, the size of the voxel was 12x12x12 mm^3.

Having optimized scanning parameters and a prepared phantom, spectrum of a solution containing all metabolites was measured. The comparison of NMR spectra measured using high resolution NMR spectrometer and 3 T MRI scanner is presented in Fig. 5.1.7. The concentrations of metabolites in the solutions for both experiments were identical.

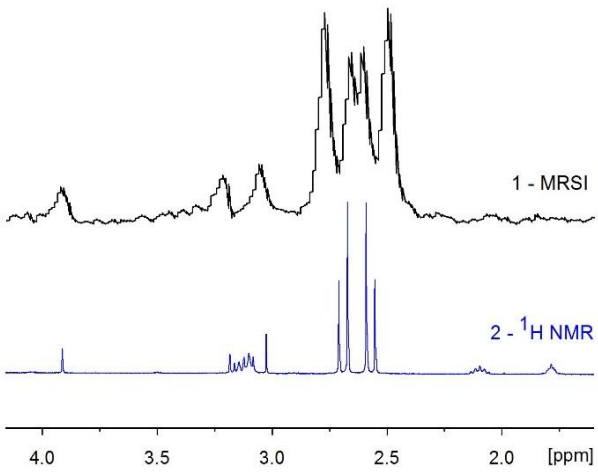

Fig. 5.1.7 An expansion of 128 MHz MRS (1) and 400 MHz ^{1}H NMR (2) spectra of prostate metabolites: citrate (Cit), creatine (Cr), spermine (Spm) and choline (Cho). The concentrations of metabolites (see chapter 4.1) in both samples were the same

Spectral resolution of MRS was noticed to be significantly lower. The broader spectral lines resulted in overlapped NMR peaks and spermine could not be distinguished. Hence, the next step was to check if the resolution would be sufficient for detecting pH dependence. The important thing to note is that in human body there is no DSS for the reference, so pH dependence measurements cannot be implemented simply using the chemical shift of citrate. A pH-independent metabolite is required. ^{1}H NMR results showed that of all metabolites only citrate is pH-dependant (Fig. 5.1.2). However, as it is seen from Fig. 5.1.7, spermine NMR peak is hardly distinguished using MRS even in the phantom studies and creatine usually has a lower intensity in prostate MRS comparing to choline. Therefore, choline was chosen as a pH-independent metabolite for the reference while measuring changes in chemical shift of citrate (Fig. 5.1.8). Because of the significantly lower spectral resolution of MRS, compared to high resolution NMR, only four points were acquired, where pH was 5.5, 6.0, 6.5 and 7.0.

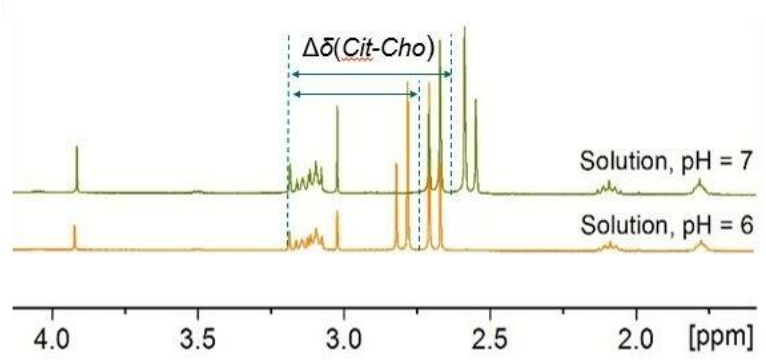

Fig. 5.1.8 An expansion of 400 MHz ^{1}H NMR spectra of prostate metabolites demonstrating the technique for measuring changes in chemical shift of middle point of citrate when there is no DSS for the reference

The pattern of pH dependence measured using MRI scanner was the same as observed using high resolution ^{1}H NMR spectroscopy. Chemical shift of citrate shifts to the left when pH of the solution is decreased, i.e. $\Delta\delta(^{1}\mathrm{H})_{\mathrm{Cit\text{-}DSS}}$ increases while $\Delta\delta(^{1}\mathrm{H})_{\mathrm{Cit\text{-}Cho}}$ decreases (Fig. 5.1.9). Considering spectrum behavior under changes of pH, which occurs if benign tissue becomes malignant, it might be worth taking into account changes of chemical shifts as an additional indicator for malignant tissue. So far, the comparison of ratios of prostate metabolites ((Cho + Cr)/Cit) is the main indicator for malignant tissue in prostate MRS [42, 103, 104]. However, this technique requires a good

quality of NMR spectrum which sometimes is a difficult task to achieve. Besides, different anatomic zones of healthy prostate show different intensities for these metabolites, as well as different metabolic ratios.

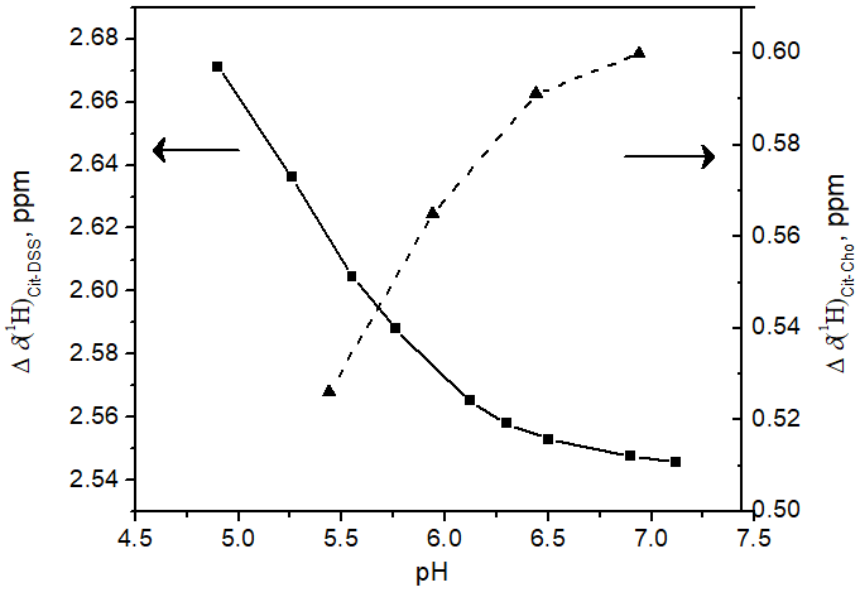

Fig. 5.1.9 Changes in chemical shift of citrate under different pH. Chemical shifts were measured between middle point of Cit and DSS in 400 MHz ^1H NMR spectroscopy (left) and between Cit and Cho in 128 MHz ^1H MRS (right)

Metabolic ratios calculated from in-vivo or ex-vivo (post-biopsy) NMR spectra are usually compared with standardized PI-RADS (Prostate Imaging-Reporting and Data System) classification as well as corresponding Gleason score derived from biopsy samples [42, 126]. PI-RADS uses a 5-point scale to determine the likelihood of clinically significant prostate cancer. Assignment of a PI-RADS assessment category for each lesion is based on the findings of multiparametric MRI (mpMRI), which is a combination of T_2-weighted (T2W), diffusion weighted imaging (DWI) and dynamic contrast-enhanced (DCE) imaging [127, 128]. Sometimes MRS is also included in mpMRI for PIRADS assessment [129], however it is not a standard procedure and is not implemented in all PI-RADS versions. Gleason score is the grading system used to determine the aggressiveness of prostate cancer [130]. Typical Gleason scores range from 6-10 where a score of 6 is low grade and a score of 8 to 10 is high grade cancer.

By finding a probe that marks the acidosis inherent in tumor metabolism, a clinical potential for marking tumors and measuring their aggressive characteristics would be defined. There are different MR methods in measuring tumor pH along with emphasizing the importance of extracellular tumor low pH on different steps of metastasis [123]. One of them is MRS. Both endogenous and exogenous NMR-active compounds, containing ^{1}H, ^{19}F, ^{31}P or ^{13}C isotopes, have been used to measure pH *in vivo.* In general, ^{1}H MRS approaches to measure tumor pH have relied on compounds, such as imidazoles and aromatics, which resonate at higher frequencies compared to endogenous metabolites. However, there are not many studies that analyze chemical shift of the metabolite under the influence of pH. In this dissertation the citrate is suggested to be used for the evaluation of pH in prostate tissue. G. Bellomo et al. reported the different values of chemical shifts (2.6 and 2,5 ppm) of Cit protons at two different values of pH: 5 and 7 respectively [103]. The in-vitro results which were performed using 3 T MRI scanner are similar to the ones presented in this dissertation (Fig. 5.1.9). However, it is not fully clear which NMR peak was used as a reference for estimating chemical shifts of citrate in the work of Bellomo et.al. Another group of P. A. DiCamillo et al. analyzes citrate chemical shift changes in 500 MHz MAS NMR spectra of prostate biopsies. It is reported that the distance between doublets of Cit decreases when pH decreases, i.e. in prostate cancer [131]. The same observations are presented in this dissertation using 400 MHz ^{1}H NMR spectra.

According to the 400 MHz ^{1}H NMR and 128 MHz ^{1}H MRS results, changes in chemical shift of pH-dependent citrate in relation to pH-independent choline might be used as additional indicator for early diagnosis of malignant prostate tissue.

Concluding remarks

- ^{1}H-MRS technique can aid in the management of cancer patients, serving as a noninvasive biomarker of metabolism in tumors. However, MRS needs expertise and is time consuming, which limit its clinical applicability. In this setting, spectra analysis needs to be simplified. Future work should also be concentrated on the evaluation of changes in the spectral patterns.

- High resolution ^{1}H-NMR is fast an accurate method useful for measuring spectral profiles of metabolites before applying them to the MRS technique in clinics. It can be used to check the quality of solutions in homemade phantom.

- Analyzing pH dependence of chemical shifts in prostate MRS is a promising method of immense medical value for additional indication of malignancy, especially when MRI is evolving to higher magnetic fields, hence better resolution.

- The obtained results helped to adapt MRS technique at Vilnius University Hospital Santaros Klinikos (VULSK). However, for clinical routine a deeper analysis of spectrum post-processing as well as installation of innovative techniques for spectrum acquisition would be needed.

- Overall, metabolomics represents an exciting avenue for discovery as the presence of certain metabolites may underscore the importance of highly utilized pathways and help determine future care.

5.2 Gd-based upconverting nanoparticles

To get the idea about how Gd-based upconverting nanoparticles (UCNPs) affect water relaxation processes, NMR experiments were started by measuring temperature dependence of water relaxation rate ($1/T_1$) in aqueous solutions of upconverting nanoparticles (UCNPs). Many samples containing different UCNPs were prepared. Most representative ones will be described in more detail.

As it was mentioned in the methodology part, paramagnetic gadolinium ion in UCNPs is the one responsible for the changes in spin-lattice relaxation time of water. Hence, the more water molecules interact with Gd, the more increased relaxation rate should be observed. First sample (NP1) was prepared using core NPs with no Gadolinium. Second sample (NP2) contained Gd-based core NPs. In order to check the influence of the coating layer containing no gadolinium, core-shell NPs with Gd only in the core were used in the third sample (NP3). The other two samples (NP4 and NP5) were prepared using the same core-shell NPs containing Gd both in the core and in the shell. The idea was to check the reproducibility of the experiment and synthesis of the same NPs. All NPs in the samples were functionalized with surfactant TWEEN80. The excess of it was removed during the centrifugation only in the last sample (NP6). Some of the results of relaxation measurements are summarized in table 5.2.1. Activation energy was calculated using temperature dependence of water relaxation rates which is shown as Arrhenius plots in Fig. 5.2.1.

Table 5.2.1 Spin-lattice relaxation (T_1) and activation energy (ΔE) of water in six aqueous samples of different UCNPs (core and core-shell) all functionalized with surfactant TWEEN80.

Sample	Type of UCNPs	T_1 at 25ºC, s	ΔE, kJ/mol
NP1	$NaYbF_4$:Er	2.248	15.88
NP2	Na**Gd**F_4:Yb,Er	0.697	3.16
NP3	Na**Gd**F_4:Yb,Er@$NaYbF_4$	2.371	16.96
NP4	Na**Gd**F_4:Yb,Er@Na**Gd**F_4 (synthesis I)	1.382	2.33
NP5	Na**Gd**F_4:Yb,Er@Na**Gd**F_4 (synthesis II)	0.246	1.58
NP6	Na**Gd**F_4:Yb,Er@Na**Gd**F_4 (excess of TWEEN80 removed)	1.432	6.32

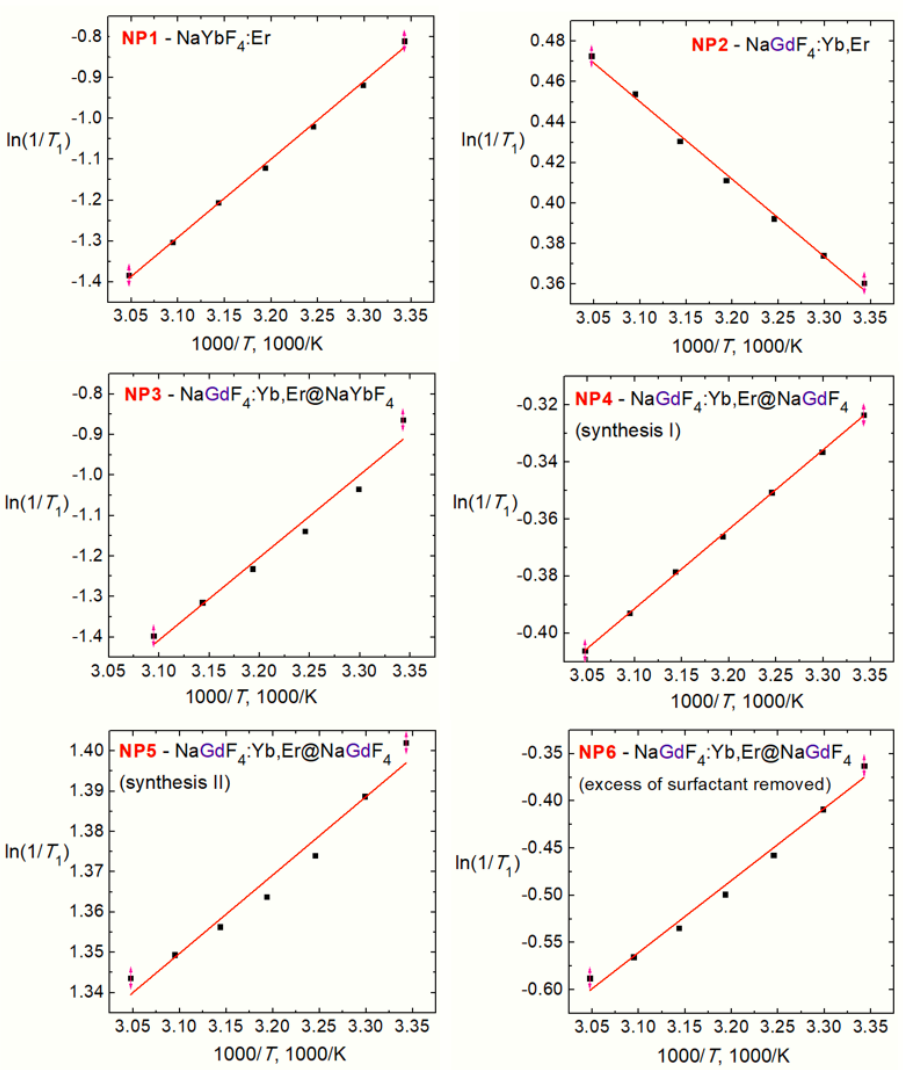

Fig. 5.2.1 Arrhenius plots of six aqueous solutions of different UCNPs. All NPs were coated with surfactant TWEEN80. Temperature varied in range from 25 to 55 ºC

Activation energy (ΔE), which can be calculated using a slope in Arrhenius plot (Eq. 5.2.1), determines how effectively the relaxation process can be initiated.

$$\ln(1/T_1) = 1/T \cdot \Delta E/R \qquad (5.2.1)$$

Here R is the gas constant (8.314 J/mol·K). From the obtained results, it can be seen that the highest activation energy and thus the longest spin-lattice

relaxation time are observed in core-shell NPs (sample NP3), where the effect of Gd in the core is diminished by the coating layer containing no gadolinium. Similar results are seen in the first sample where no gadolinium is present. For comparison, the spin-lattice relaxation time of water was measured in a solution of TWEEN80 with no NPs as well as in bulk water. Values of T_1 at 25 ºC were 2.026 s and 3.067 s respectively. The best relaxation rates were observed in NPs where gadolinium was close to the surface, hence participating in stronger interaction with water. In five of six samples the spin-lattice relaxation time increased with increasing temperature and only in one sample (NP2) the dependence of T_1 on temperature was reversed. It is determined by the $\omega\tau_c$ (eq. 3.4.2). When $\omega\tau_c << 1$, the relaxation rate 1/ T_1 is directly proportional to the correlation time, hence, when the temperature is increased, meaning shorter correlation time, the relaxation rate decreases. Otherwise, when $\omega\tau_c >> 1$, the relaxation rate is inversely proportional to the correlation time.

The results obtained from samples NP4 and NP5 were expected to be similar, since the UCNPs were the same. However, the values of T_1 differed more than 5 times. It could be explained if their synthesis were slightly different or if the concentrations of the UCNPs were not the same. This could happen if the samples were not homogeneous before preparing them for NMR measurements. Evaluating the effectives of UCNP as a potential MRI contrast agent, the known concentration is very important (see eq. 3.4.1). The concentration of NPs in all the samples was supposed to be 1 g/l. However, in some samples the sediment was noticed. For the NMR experiment only 500 μl of the sample is needed, so if the original solution is not properly mixed, the concentration of NPs might be much lower.

For further analysis, two most stable samples, regarding the reproducibility of NMR measurements, were chosen: 12 nm core NPs ($NaGdF_4$:$Yb_{0.18}Er_{0.02}$@ TWEEN80) and 19 nm core-shell NPs ($NaGdF_4$:$Yb_{0.18}$,$Er_{0.02}$@$NaGdF_4$@ TWEEN80). The ultrasonic bath for each sample was applied for 2 minutes before NMR experiment.

5.2.1 NMR Relaxometry

Experiments were started by measuring spin-lattice relaxation (T_1) of bulk water, which was used to prepare different concentrations of our contrast agents. Measurements were performed at 37 ºC imitating the temperature of human body. The obtained value of relaxation rate (R_1 = 0.26 s^{-1}) was later needed for the calculations of relaxivities (Eq. 3.4.1) of our analyzed samples.

The measured T_1 value (3.9 s) of water was in good agreement with the ones from literature [132, 133] (Fig. 5.2.2).

The results showed that relaxivity of CAs increased from 0.684 $mM^{-1}s^{-1}$ for 19 nm NPs to 0.986 $mM^{-1}s^{-1}$ for the 12 nm ones. According to the literature [134-137], for T_1 contrast agents, smaller-sized NPs usually generate greater contrast enhancement. Several research groups reported similar size effects of $NaGdF_4$ NPs on relaxivity. Reported correlations of NPs sizes and their relaxivities showed that contributions from the surface-to-volume ratio increased with decreasing NP size, becoming the dominant contributing factor. However, Gao and co-authors demonstrated that larger NPs possessed higher r_1 value. It was explained by saying that τ_R became lower for larger NPs (>15 nm) and played a dominant role in affecting relaxivity [138]. In this study, even if the size of NPs reached 19 nm, the results showed that it was still in a range where surface-to-volume ratio was the dominant contributing factor.

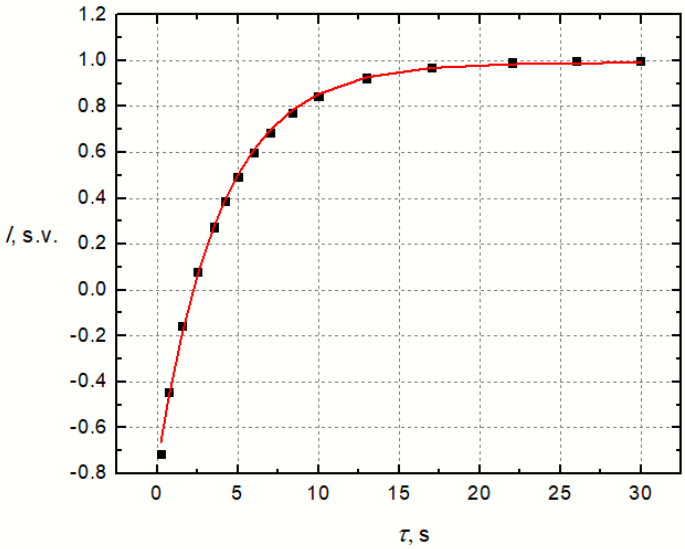

Fig. 5.2.2 Dependence of water NMR peak integral on delay time τ obtained from inversion recovery 400 MHz NMR experiment used for measurements of water spin-lattice relaxation time (T_1 = 3.9 s at 37 ºC)

All research groups mentioned above, worked with magnetic fields of less than 3 T, which is the most common magnetic field strength applied in clinical routine. As mentioned before, NMR experiments in this study were carried out

using spectrometer operating at resonance frequency of 400 MHz. For comparison it was decided to measure r_1 values of NPs at the 0.4 T magnetic field as well. The summarized results of T_1 measurements of two different sized nanoparticles at two different magnetic field strengths are shown in figure 5.2.3.

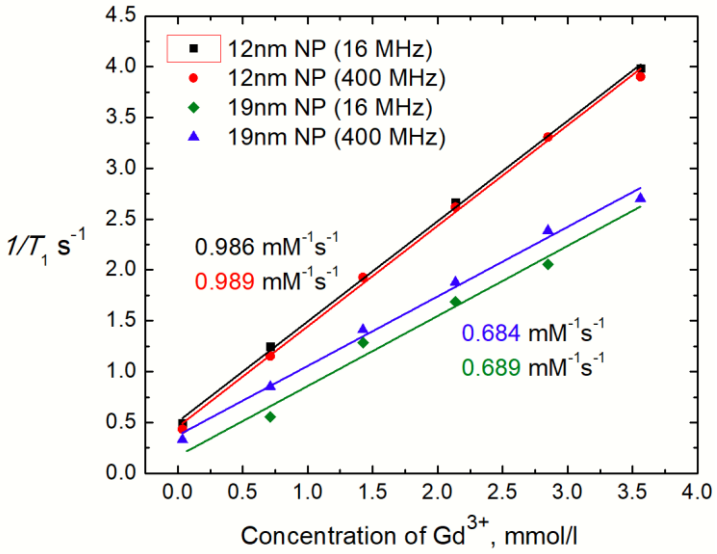

Fig. 5.2.3 Spin-lattice relaxation rates in aqueous solutions of different sized β-NaGdF4 nanoparticles (12 nm core and 19 nm core-shell) as a function of concentration of Gd^{3+} ions measured at two different magnetic fields at the temperature of 37 ºC

It is well known that the spin-lattice relaxivity for Gd-based contrast agent typically decreases with increasing magnetic field [54-55]. However, no significant difference in relaxivity, comparing the r_1 values, measured at 16 MHz and 400 MHz, was noticed. This suggests that relaxivity of analyzed UCNPs will be the same at 3 T MRI scanner.

For comparison, NMR relaxometry for a commercial MRI contrast agent *Gadovist*, was also performed. Samples were prepared with concentrations varying from 0.01 μmol/l to 14 mmol/l. The results are demonstrated in Fig. 5.2.4. Note, that concentrations of UCNPs were given in g/l and were recalculated to mmol/l of Gd^{3+} ions. It was done by presuming that Gd^{3+} ions contribute to 61% of mass of NPs. Relaxivities of analyzed UCNPs were relatively poor comparing to commercial CA (r_1 = 3.2 $mM^{-1}s^{-1}$), because the interaction between Gd^{3+} ions encapsulated in NP and water molecules was

more restricted than the direct interaction between Gd^{3+} ions in chelate and water molecules.

For better understanding of the mechanisms of water spin-lattice relaxation processes, NMR diffusion measurements of water in the same samples of UCNPs was performed.

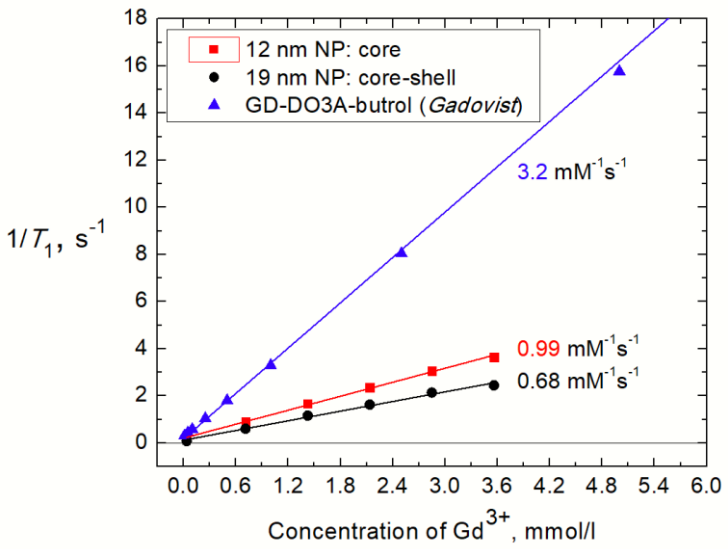

Fig. 5.2.4 Spin-lattice relaxation rates in aqueous solutions of different sized β-$NaGdF_4$ nanoparticles (12 nm core and 19 nm core-shell) and a commercial contrast agent Gadovist as a function of concentration of Gd^{3+} ions measured with 400MHz NMR spectrometer at 37 ºC

5.2.2 Diffusion experiments

The results of NMR diffusion for core-shell 19 nm NPs are demonstrated in Fig. 5.2.5. Instead of one diffusion constant, as expected in most NMR cases, two coefficients (D_1 and D_2) were obtained having different contributions (around 96% and 4% respectively) to the total intensity of NMR signal.

For further analysis of two diffusion coefficients, their dependence on the temperature at two different concentrations (1 g/l and 0.75 g/l) of 19 nm core-shell NPs was measured. Knowing temperature dependence of diffusion coefficient (Eg. 3.5.1), activation energy can be calculated in a similar way as it was done using temperature-dependent $1/T_1$ values obtained from spin-lattice relaxation measurements.

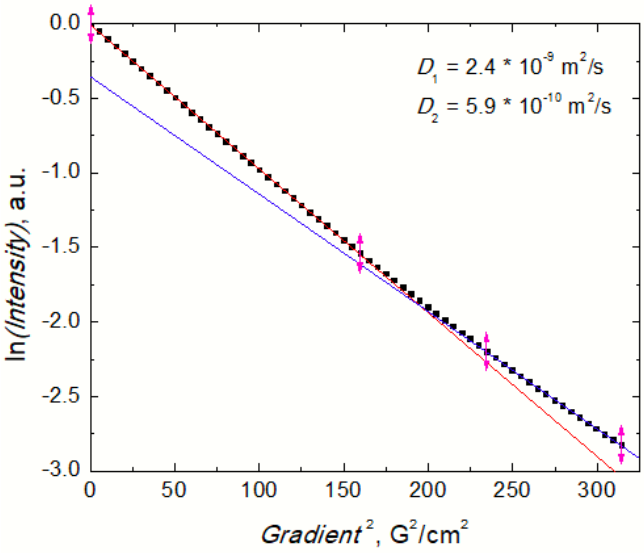

Fig. 5.2.5 Signal decay of aqueous solution of 19 nm core-shell NPs versus squared gradient strength. Two separate diffusion coefficients (D_1 and D_2) were calculated by fitting

It was found that one diffusion coefficient was concentration-dependent, while the other one remained the same for both concentrations (Fig. 5.2.6). Moreover, the activation energy of pure water, calculated using the results from relaxation experiments (20.442 kJ/mol), was comparable to the activation energy of water in NPs samples, calculated using the temperature dependence of D_1 values (21.362 kJ/mol).

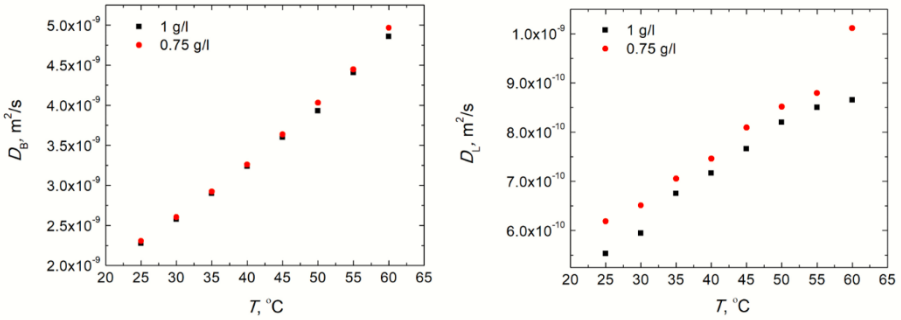

Fig. 5.2.6 Temperature-dependent diffusion coefficients of bulk water D_B (left) and local water D_L (right) for 19 nm core-shell NPs of different concentrations

On the basis of the obtained results, for the later analysis the simplified SBM model will be used assuming that there are only two processes involved in the relaxation mechanism. One of them will reflect the behavior of bulk water having the diffusion coefficient D_B (instead of previously used D_1). The other one will represent local water (water molecules that interacts with Gd^{3+} ions directly) having the diffusion coefficient D_L (instead of D_2). Then the total relaxation rate can be written as in Eg. (5.2.1):

$$R_1 = R_{1B} \cdot I_B + R_{1L} \cdot I_L. \quad (5.2.1)$$

Here I_B and I_L are the contribution of bulk and local water diffusion in CA samples to the total signal intensity. Their values were given by the Topspin 3.2 software together with the calculated diffusion coefficients. If the relaxation rate of bulk water (R_{1B} value) is changed to the relaxation rate of pure water, the relaxation rate of local water at the surface of NPs can be calculated, because all the other parameters are known.

This relationship between relaxation and diffusion opens more possibilities to investigate water molecules near the surface of UCNPs, which deepens our understanding of key factors influencing the relaxivity of contrast agents.

Concluding remarks

- Strategies to achieve high relaxivity of MRI spin-lattice contrast agents are mainly focused on enhancing the interaction between NPs and nearby water protons. This study demonstrated that the diffusion processes of water, measured by NMR spectroscopy, might be related to the SBM model, which is used for explaining relaxation mechanisms of MRI contrast agents. Using such relationship, not only the total impact of NPs on relaxation of water molecules, but also the impact on relaxation of local water molecules, directly connected to the paramagnetic Gd^{3+} ions in NPs, can be calculated.

- An in-depth understanding of these processes can guide the engineering of future NPs finding the most optimal structure for the enhancement of spin-lattice relaxation. The next generation of MRI CAs is being developed based not only on the design principles of NPs, but also on the development of advanced nanotechnology, novel MRI techniques and new clinical applications. This is why it would be

valuable to design multimodal contrast agents that have excellent relaxation properties over a broad range of imaging field strengths and are characterized by effective upcoversion properties.

- In this work it was demonstrated that different magnetic field strengths did not alter the spin–lattice relaxivity of water in presence of Gd-based upconverting nanoparticles (UCNPs). It was also shown that smaller NPs (12 nm comparing to 19 nm) were more favorable regarding the effectiveness of MRI contrast agent.

- On the basis of the results, it follows that Gd-based UCNPs can be developed into high-performance multimodal MRI contrast agents.

5.3 Sunset Yellow FCF

NMR and Raman spectroscopy techniques have already proven to be powerful tools in LCLCs studies. [139-143]. In this work too, already during the first experiments, it was noticed that NMR technique is sensitive to many processes in the samples of SSY. The ^{1}H NMR spectra clearly showed that after the initial mixing in the isotropic phase, there are different kinds of phase behavior and slow self-assembling depending on the concentration, age, and thermal history of the mixtures (Figure 5.3.1).

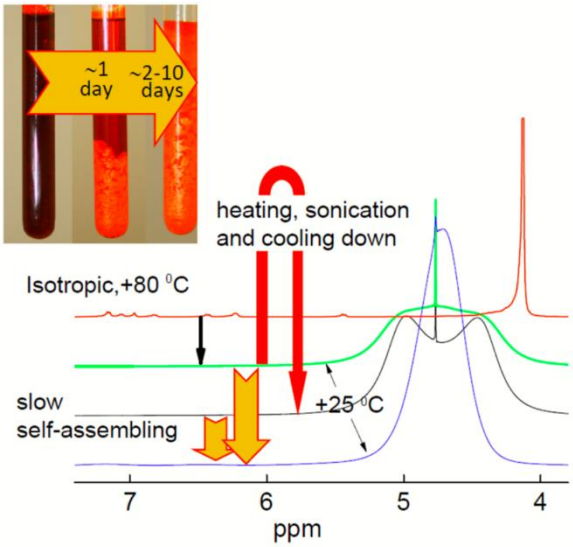

Fig. 5.3.1 Temperature evolution of the ^{1}H NMR spectra in 1.2 mol/kg SSY aqueous mixture at phase transitions and slow self-assembling depending on the degree of mixing and thermal history. The detailed evolution of signal shapes and chemical shifts is shown in Fig. 5.3.4 – 5.3.6. See text for more comments

5.3.1 Tautomeric Equilibrium and Aggregation

The greater stability of the N–H···O form as compared to that of O–H···N in the series of molecular systems with intramolecular H-bonds was noted and discussed in terms of the greater proton affinity of nitrogen with respect to that of oxygen and the resonance assisted H-bonding [144]. The DFT calculations carried out in the present work also predict that the tautomeric equilibrium in SSY should be strongly shifted toward the hydrazone form. It is characterized by the equilibrium constant pK_T = 2.5 as obtained at the DFT SMD level of

theory. However, the DFT-based estimate of the tautomeric equilibrium constant is regarded as a lower bound of the equilibrium. The fact that the hydrazone form is dominant in SSY was deduced also in other works using ^{13}C NMR shifts [141] and Raman spectroscopy [142]. Inspired by the fact that the experimentally observed ^{13}C chemical shift of C4 (Fig. 5.3.2) of 177 ppm [141] falls in the range between presently calculated values of 156.9 and 184.3 ppm for C4 in azo and hydrazone tautomers, respectively, using DFT, it was decided to revisit this problem. Moreover, the DFT-predicted difference in the chemical shifts of N1 nitrogen in those tautomeric forms is very huge – up to 260 ppm – and therefore ^{15}N NMR experiments look to be extremely promising for the detection of possible tautomeric forms. The long-range $^{1}H–^{15}N$ correlation, widely known as HMBC, was applied for this purpose (Fig. 5.3.3).

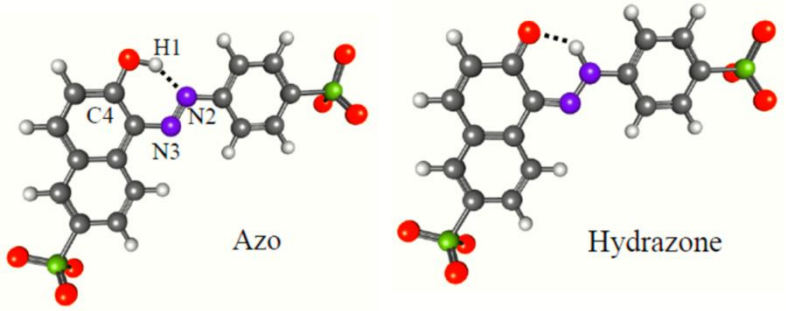

Fig. 5.3.2 Calculated molecular structures of azo- and hydrazine tautomers of dianionic SSY at B3LYP/6-311G level and the labeling of atoms used in the discussion*

The two-dimensional spectrum is smeared out due to the strong solvent signal at 4.7 ppm (H_2O). Nevertheless, the peaks at (6.9 ppm; −178 ppm) and (4.4 ppm; 0 ppm) are clearly seen. They correspond to the ^{1}H and ^{15}N correlations in SSY and in nitromethane (used for reference), respectively. The value of observed chemical shift $\delta(^{15}N)$ = −178 ppm is in fairly good agreement with the DFT-calculated value at −191.5 ppm for N2−H nitrogen in hydrazone tautomer of SSY (Fig. 5.3.2), whereas this peak in the azo tautomer should be observed at +58.4 ppm (see Table A1). This means that ^{15}N NMR data also confirm the dominance of hydrazone form of SSY in the present conditions (0.7 M of SSY in water at 293 K). Unfortunately, the ^{15}N NMR signal of N3 that should be present at −8.9 ppm or +122 ppm for

hydrazone and azo tautomers, respectively, was not found experimentally. Most probably, this is due to the too long correlation with protons, as it is evident from the molecular structure of SSY (Fig. 5.3.3).

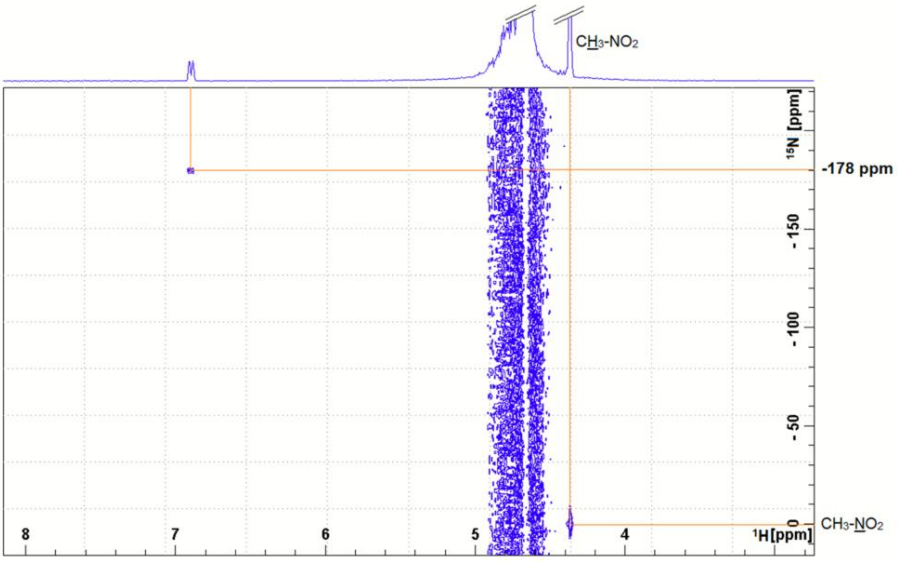

Fig. 5.3.3 ^{1}H-^{15}N correlation (HMBC) trough long-range couplings in 0.7 mol/kg SSY aqueous solution at 25 °C

The chemical shift of the N−H···O bridge proton (H1, see Fig. 5.3.2) is expected to be another very sensitive NMR spectral feature because it can provide the direct information on the tautomeric dynamics and the strength of H-bond in SSY. The chosen DFT level using the PBE0 (*The Perdew–Burke–Ernzerhof*) exchange correlation functional has proven to be one of most successful choices for NMR shielding calculations, particularly for the nuclei involved in strong H-bonds [145, 146]. A perfect agreement between the calculated and experimentally observed ^{1}H chemical shift was obtained in many cases, e.g., picolinic acid N-oxide (PANO) dissolved in various solvents [146]. PANO and SSY can be considered as closely related systems because strong intramolecular H-bonds are formed in both. The success of DFT application for the first system makes it promising for SSY as well. The calculations predict that the chemical shifts of H1 proton of SSY are 15.4 and 16.8 ppm, depending on the tautomeric form (Table AI). Note the shift values covering the range from 14.1 to 18.4 ppm were determined experimentally for series of N−H···O bonds as the N···O distance shortens from 2.51 to 2.56 Å [144]. A problem of experimental observation of this signal in SSY aqueous

solution may arise because of the solvent, which is water. It is usually expected that protons involved in H-bonding should undergo fast exchange with water. Thus, their NMR signals are consequently broadened and not observed. A nice example of such a behavior was observed in PANO: the peak of O−H···O proton at 17−19 ppm is clearly observed in a series of solutions in traditional solvents and even in some ionic liquids, but not in aqueous solution [146]. Such a priori knowledge leads to certain pessimism, so that the researchers even do not struggle much to find this peak.

However, in the case of chromonic liquid crystals, one peculiar feature of these systems is met – a strong self-assembling. It is known that chromonics are lyotropic liquid crystals, but in general, they do not possess a critical micelle concentration, [64, 73, 147] as it is usually in many cases of amphiphilic molecules forming the lyotropic liquid crystalline phases and gels [145, 148 and references therein]. Hence, unlike many lyotropic liquid crystals, self-assembly in chromonics occurs at very low concentrations [149]. The self-assembling leads to the formation of rod-like aggregates, also more complex geometries with "stacking faults" [69, 150]. These structures are stabilized by the $\pi-\pi$ stacking interactions between the aromatic rings [64, 73, 149]. Thus, one can expect that water molecules can interact and thus get into an exchange with H1 protons of SSY placed on the aggregate surfaces only. But water does not penetrate into the bulk of the aggregate. It could mean that the N−H···O bridges are confined inside the aggregates and if the lifetime of those aggregates is $\geq 10^{-7}-10^{-8}$ s, which is the typical NMR time scale or even longer, the corresponding ^{1}H NMR signal can be expected to appear in the spectrum. And indeed, the peak at 14.2−14.7 ppm was found at all compositions studied in the present work and in all phases, except at three lowest temperatures 25, 30, and 35 °C of the cooling cycle (Fig. 5.3.4A). After the system has evolved via long-lasting self-assembling to the equilibrium, this peak was seen even at those temperatures (Fig. 5.3.4B).

First, these values of chemical shifts are slightly below the DFT-predicted ones (Table 1). For one thing, DFT calculations of the NMR shielding have been carried out for isolated molecules, and solvent effects remain unaccounted for. On the other hand, this could indicate that some H1 protons of SSY, most probably, on the aggregate surfaces, exchange with water indeed. The observed slope $\Delta\delta/\Delta T$ ~-0.022 ppm/deg (Fig. 5.3.4C) is significantly higher than could be expected in the case of solely H-bond effect. $\Delta\delta/\Delta T$ values usually observed for various H-bonded systems are spread from ca. -0.006 ppm/deg (e.g., pyridine N-oxide/acids complexes and PANO) to

-0.012 ppm/deg (the neat water) [146, 151]. The steep increase in the chemical shift δ(N−H) with decreasing temperature in the M phase (Fig. 5.3.4C) can be explained to be due to the growth of SSY aggregates (columnar stacks) accompanied by the segregation of water in the intercolumnar regions, and thus drastically reducing the exchange between water and N−H protons.

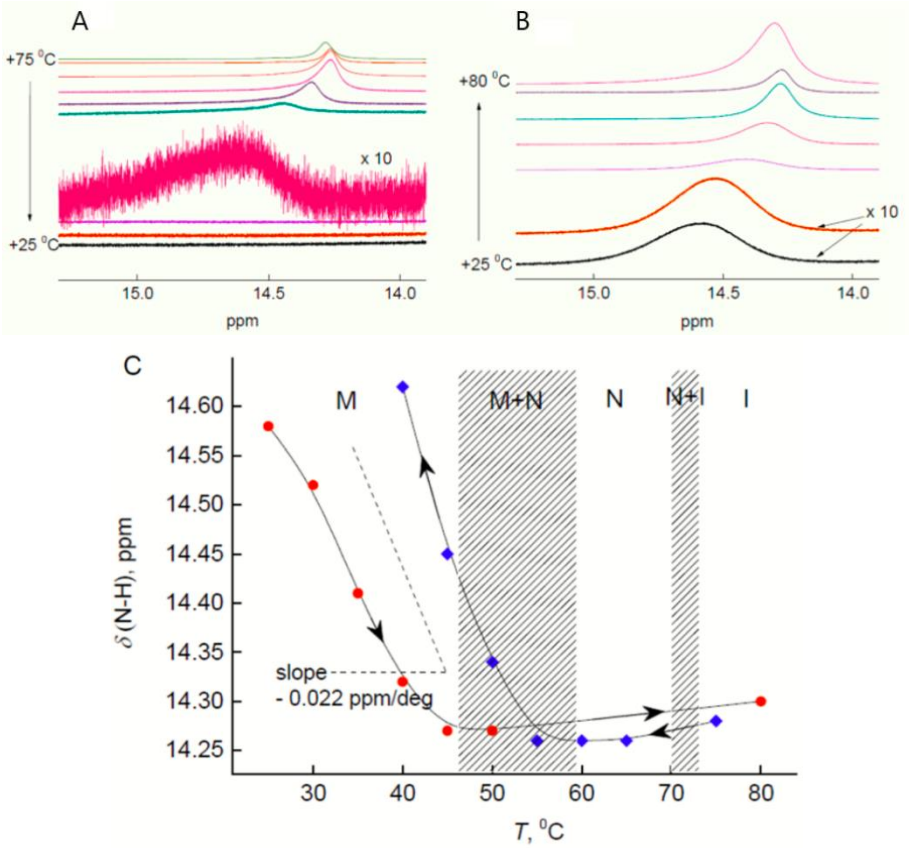

Fig. 5.3.4 Evolution of ^{1}H NMR signal shape at cooling (A) and heating (B) cycles and the dependencies of chemical shift of N−H···O proton on temperature in 1.2 mol/kg SSY aqueous solution (C)

The broadening of the H1 signal with decrease in temperature is caused by several overlapping factors. The main contribution to the signal broadening comes from the slowdown of an overall rotational motion with increasing size of the SSY aggregates. Nuclear Overhauser enhancement spectroscopy experiments [143] have shown that the SSY molecules are in the intermediate tumbling regime with the rotational correlation time of ~300 ps in the

isotropic phase. However, the slow tumbling and slow spin-diffusion regimes, which are characteristic for large molecules with long rotational correlation times, are reached in this system at increasing concentration of SSY [143]. As the peak at 14.2−14.7 ppm was not found at the lowest temperatures of the cooling cycle (Fig. 5.3.4A), it can be stated that the nonequilibrium fluctuations in the local environment can also contribute to the signal broadening.

All other ^{1}H NMR peaks of SSY protons disappeared at the lowest studied temperatures for the same reasons too (Fig 5.3.5), but not the peak of water (Fig. 5.3.6). Moreover, the signal shape and the chemical shift $\delta(H_2O)$ depend not only on the concentration and temperature, but – what is the most important – on the thermal history (Fig. 5.2.1). Thus, it can be effectively used to study the slow self-assembling when the borders between N, N + M and M phases are crossed.

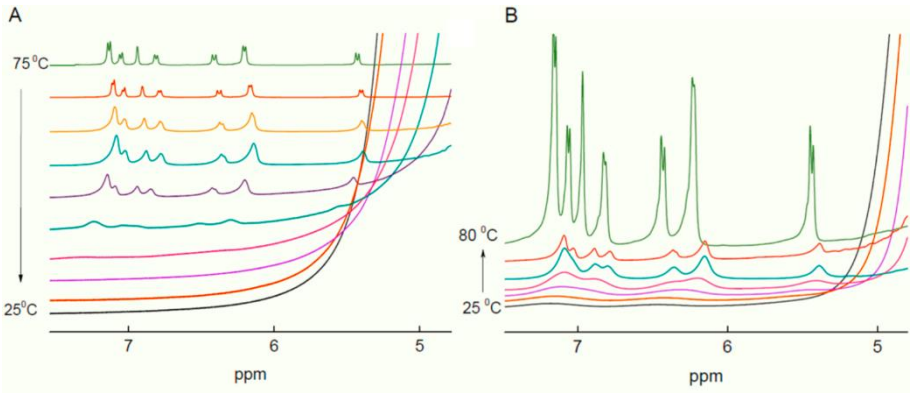

Fig. 5.3.5 Temperature evolution of ^{1}H NMR spectra of SSY protons in 1.2 mol/kg SSY aqueous solution at cooling (A) and heating (B) cycles

5.3.2 Slow Self-Assembling

Going through the experimental details published in literature, it becomes evident that the temperature variation rates traditionally used in the experiments where phase behavior in LCLC systems is studied are in the range of 0.2 - 0.4 deg/min [64, 69]. In some cases, the heating/cooling cycles were carried out using a much higher rate of 5 deg/min, although it used to be reduced to 1 deg/min near the phase transitions. The results presented in Fig. 5.3.4 and 5.3.6 show that such rates indeed look to be properly working within I, N, and the coexisting I + N phases.

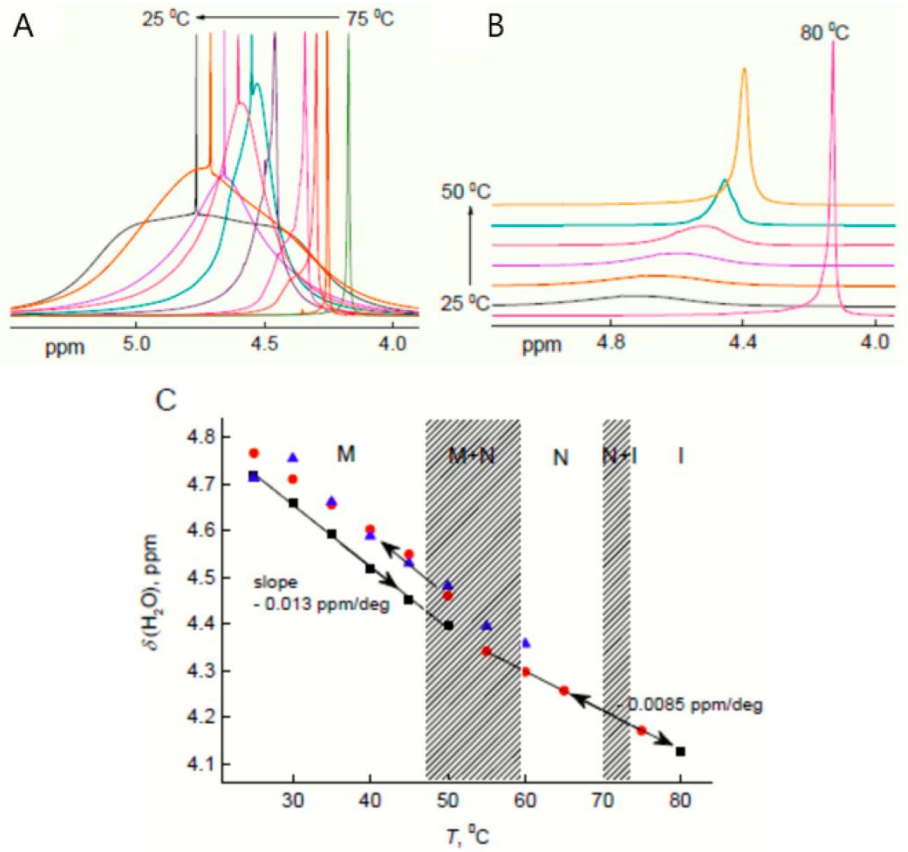

Fig. 5.3.6 Evolution of ^1H NMR signal shape of H_2O protons at cooling (A) and heating (B) cycles and the dependency of H_2O chemical shift on temperature (C). The spectra in the cooling cycle were normalized for better visualization to maximal peak height. The points corresponding to the chemical shifts of "broad" and "narrow" signal components are marked by blue triangles and red circles, respectively

The measured dependencies of the chemical shifts δ(N−H) and δ(H_2O) on temperature are practically identical, both for the cooling and the heating cycles. However, it is obvious that such rates at the cooling and at the crossing of N + M to M phase border are too high. The equilibration time for N + M → M process is very long, most probably because of supramolecular restructuring, i.e., the growing of aggregates (columnar stacks) in the M phase. Hence, if the sample is cooled down relatively fast to the temperature below N → M transition, the structural changes are behind, and the system falls to the supercooled state. In that case, the system evolves via slow self-assembling

from this state to the equilibrium. This process is very clearly reflected in the ^{1}H NMR spectra via the appearance of the wide "podos" around the peak of H_2O at 4.1−4.8 ppm (Fig. 5.3.1 and 5.3.6). The signal can be decomposed into narrow and broad components. If the sample is kept at the constant temperature in the M phase (+25 °C) for a day or tens of days, in some cases, the complex signal shape collapses to the single contour having a moderate width. Such an evolution of the ^{1}H NMR signal shape at a slow self-assembling is shown in Fig. 5.3.1. Visually it looks like an extremely slow phase separation (see the insert photo in Fig. 5.3.1) that can last over a day or tens of days. The samples start to look as if the bulk water was gone (evaporated) and the samples were dried. It is possible that the observed phenomenon can be related to a certain stage of the drying of liquid crystal droplets that was very recently discovered dealing also with the SSY aqueous solutions [152]. However, note that the process observed in the present work is reversible, i.e., the spectra return to the initial look after the sample is heated. It means no water was gone from the samples, and this was confirmed by repeatedly weighting the samples.

A quite logical question arises – what are the state and properties of water after slow self-assembling is completed. It is obvious to assume that the growing of columnar stacks is accompanied by the segregation of water molecules in the intercolumnar areas. The state of confined water was studied by analyzing the temperature dependencies of the ^{1}H NMR shift of H_2O. After the slow self-assembling was completed, the slope of the dependency of the ^{1}H chemical shift of water on temperature during the heating cycle was deduced to be −0.013 ppm/deg, i.e., practically the same as for the neat water (−0.012 pm/deg, [151 and references therein]). Similar observation was reported analyzing the temperature dependencies of the Raman band shape (Fig. AII). In the vicinity of the N → N + M phase transition, the observed changes of the Raman band shape in the range of 2800−3800 cm−1 are mimicking the *v*O−H···O band intensity evolution in the neat water at the melting point [153]. These findings allow to conclude that (i) water in the intercolumnar areas can be considered as neat and (ii) the degrees of freedom of molecular motion in confined water are changing at the border to M phase in similar manner as at the melting of ice. However, the former process takes place at $T \sim 55$ °C, i.e., at a significantly higher temperature than the melting point of water. On the other hand, it is well known that the geometric confinement can cause the shifts in the melting point, e.g., water in mesoporous carbon materials [81].

The LCLCs can appear to be very intriguing systems to study H-bonding and proton transfer (PT) phenomena. Discussions and recent works show persisting or even boosting interest in these phenomena [155 and refs therein]. The hydrazone form of SSY, according to the equilibrium constant $pK_T = 2.5$, can be considered as the protonated H-bond system N2–H1...O (Fig. 1), where 1H proton is most of the time located main time in the energy minimum near the N2 nitrogen, and jumps to the O–C4 oxygen are rare. However, there are many other LCLCs with the intramolecular H-bonds (e.g. Acid Red 27, RU31156, etc, [68]) in which the low-barrier H-bond could be formed and thus the bridge proton motion of much larger amplitude could be expected. The reversing of the system to the N...H–O bond could be realized then by various external stimuli (solvent, added ions, temperature, *etc*). Crucial role of medium in PT processes is stressed almost in all studies on this topic. Therefore, in the most optimistic scenario the chromonic phases could provide a unique possibility to study the effect of crossover from the solvent reaction field, which acts in highly diluted LCLC, to the crystal force field in large molecular stacks in the M-phase on PT processes.

Concluding remarks

- The joint application of NMR, Raman spectroscopy and DFT methods allowed to reveal fine details in temperature and composition effects passing through various phases of SSY aqueous solutions from the isotropic (I) to the principal chromonic phases – nematic (N) and columnar (M) ones.

- The phase transitions I $\leftrightarrow$ I+N $\leftrightarrow$ N look to be 'soft' enough from the point of view that no drastic discontinuous changes have been noticed in both Raman as well as in NMR spectra. The changes of spectral parameters covering these phase transitions are reversible in both direction (heating and cooling) at the traditionally used temperature variation rates. The equilibration time for N+M $\rightarrow$ M transition is very long, most probably because of slow supramolecular restructuring, i.e. the growing of hexagonal stack arrays in M phase.

- The growing of SSY aggregates is accompanied by the segregation of water in the intercolumnar areas. This restricts the exchange between

H_2O and N–H protons in the internal layers of the columnar stacks. The N–H signal in ^1H NMR spectra observed in the present work for the first time supports this statement. The joint analysis of temperature dependences of H_2O chemical shift and Raman νO–H band shape has shown that water confined in intercolumnar areas behaves as in a neat substance.

- Water molecules in the intercolumnar space are confined possibly in a form of droplets or 'water pockets', as it was found recently in some ionic liquid/water solutions. Since LCLC molecules and ionic liquids have ionic groups at the periphery, such from the first sight far analogy between them can have a sense and can be a challenging goal for future experiments.

- The tautomeric equilibrium in SSY is strongly shifted towards the hydrazone form – less than one azo tautomer is present among ~ 100 hydrazone tautomers. The dominance of hydrazone form was confirmed experimentally using the long-range $^1H–^{15}N$ correlation (HMBC) and by the DFT SMD calculation.

5.4 Hydroxyapatite

H-bond clustering of water molecules confined in nano-structured calcium hydroxyapatites ($Ca_{10}(PO_4)_6(OH)_2$, CaHA) was studied by means of ^{1}H MAS NMR spectroscopy and FTIR. Knowledge about water clustering processes in inert matrices can be very helpful assigning the bands and recognizing the states of water in *terra incognita*, i.e. in much less investigated cases - water in nano-structured and other advanced/smart materials.

2DCOR analysis [156, 157] was applied as the novelty to study water in argon matrix. This allowed to reveal the correct number of overlapping bands being sure no fine details were missed. Namely, FTIR spectra for 2DCOR analysis have been measured using thermal perturbation by heating the sample from T = 9 K to 40 K stepping by 2 K (Fig. AIII). The mathematical formalism and the further steps of 2D FTIR absorption correlation analysis were the same as in the earlier matrix isolation work on 1-propanol [156]. The band maximum positions determined from the crosspeaks positions in 2D asynchronous spectrum (Fig. AIV) were used as the initial input parameters of the non-linear curve fitting routine and were refined during the next iterations for each temperature. The fitting result is shown in figure AV. The peaks of monomer, dimer and higher clusters up to hexamers have been perfectly resolved and easily identified comparing their positions with those in other works determined experimentally and supported by high-level theoretical calculations [75, 77, 158 - 160].

However, it has to be noted that the matrix isolation experiments are carried out at very low temperatures, whereas the main interest for many processes and innovative technologies lays in the range around room temperature. It was shown [79] that small water clusters can be detected at room temperature by FTIR spectroscopy dissolving water in hydrophobic solvent CCl_4. Besides the water monomer, a dimer, a cyclic trimer, a cyclic tetramer, and a large hydrogen-bonded structure (supposed - a cage hexamer) were found. However, some revision of the assignment of the bands seemed to be necessary. After few corrections heightening the cluster size: dimer $\rightarrow$ trimer, trimer $\rightarrow$ tetramer, *etc*., a good agreement between the matrix and the hydrophobic solvent experiments was achieved. The environmental and thermal effects on the cluster band positions were less than 20 - 30 cm^{-1}, except the cases of dimer and the clusters with $n \geq 6$. These data can be useful moving

from very low- to ambient temperature range, as well as explaining FTIR and NMR features of water in series of nano-CaHAs.

Some of spectral features of the NMR and FTIR spectra of CaHAs are well-known. Namely, a strong and narrow line centered at approximately 0 ppm in the ^{1}H MAS NMR spectra (Fig. 5.4.1) is corresponding to hydroxyl groups localized in the channels along the *c* axis in CaHA crystallites, i.e. in the bulk [86, 87, 161]. M.B. Osman et.al. for the first time showed an experimental spectroscopic feature based on ^{1}H NMR that accounts for the presence of two types of bulk OH at 0.10 and -0.13 ppm. Their study proposed two models for the orientations of the OH dipole in the channels (Fig. 5.4.2). The two different types of bulk hydroxyl groups $OH_{B\text{-}1}$ and $OH_{B\text{-}2}$ might correspond to the so-called "up" and "down" orientations, leading to two different distances between two protons of adjacent hydroxyl groups, and between two protons oriented in the same way. A unique *ν*O–H stretching vibration at 3572 cm^{-1} can be also observed by infrared (Fig. 5.4.3). Its narrowness is indicative of the absence of hydrogen bonding and it is consistent with the distances between two adjacent O belonging to the $O–H^{-}$ groups inside the channels (0.344 nm) [162].

A special attention has to be paid to water surface (dangling) modes. Theoretical calculations, supported by experimental studies, suggest that water molecules in the dangling mode, denoted as dH, are bi- or tri-coordinated, presenting one free OH bond dangling at the surface [163]. This mode can be recognized in the FTIR spectra of water in nano-CaHAs at 3640 - 3651 cm^{-1}. Another spectral features within 3700 - 3850 cm^{-1}, which slightly shift depending on the samples, can be assigned to the O–H stretching vibration of the P-O-H groups of surface HPO_4^{2-} and/or $H_2PO_4^{-}$ ions produced by the protonation of PO_4^{3-} ions [162, 164]. The presence of protonated ions on the crystallite surfaces in the studied materials was confirmed by ^{1}H–^{31}P CP MAS kinetics experiments [121]. The quite diffuse contribution, ranging from 8 to 13 ppm in ^{1}H MAS NMR, is in line with the numerous surface *ν*P-O-H contributions observed by infrared [86]. This might be explained by different local surface structure and different protonation levels. Note, the bands at ≥ 3800 cm^{-1}, that were observed in the home-made CaHAs and not seen in the commercial sample, as far as it is known, were never reported in the literature. Thus, their origin has to be studied in the future works.

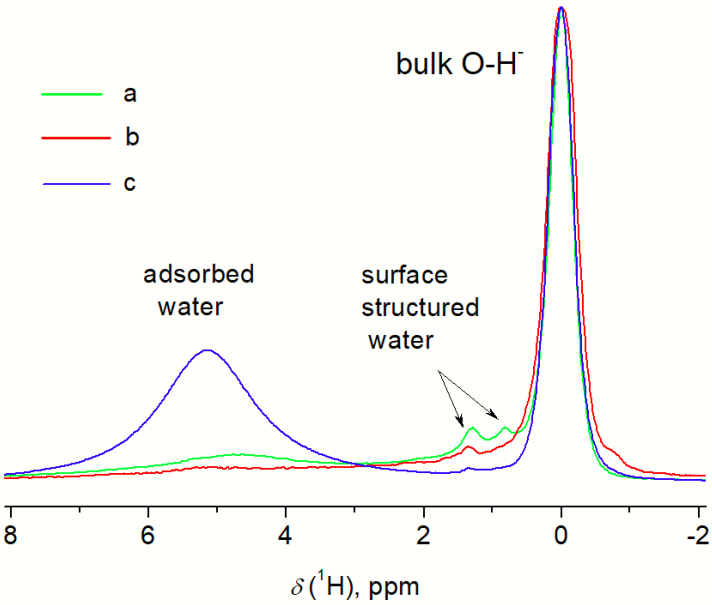

Fig. 5.4.1 ^{1}H MAS NMR spectra of CaHAs prepared via the sol-gel synthesis routes using various complexing agents: a - ethylene glycol; b - tartaric acid; c - commercial. The intensities were normalized respect to the peak of $O–H^{-}$ protons in the bulk at ~0 ppm

Several minor peaks in ^{1}H MAS NMR spectra at 0.5 - 3.0 ppm are often observed in various CaHAs and related materials [87]. In the present study, two narrow signals in ^{1}H MAS NMR spectra at 0.8 and 1.3 ppm were observed as well (Fig. 5.4.1). Since these peaks do not appear in cross-polarization (CP) MAS NMR spectra, most probably, they are originated from the highly mobile protons. Besides, the lines are very narrow which is quite unusual for surface species. A well-structured surface species should rather be considered. However, their assignment presented in literature was long time controversial. Only recently in the work [86] it was shown that these peaks were originated to the structured external water molecules stacking up in the alignment with bulk OH present inside the channels. Unlike the previous authors also proposing water assignment for the 1.1 ppm line, these new experimental results enable to discuss the bulk or surface location of the 0.8 and 1.3 ppm lines and to explain their differentiation with chemi/physisorbed water involved in the broad line at 5.1 ppm (Fig. 5.4.1). These lines are all greatly impacted by the water content in the samples. At increased hydration level,

only a single line at 1.1. ppm is detected, while at low water content, the structural H_2O_{UP} and H_2O_{DOWN} lines split into two (0.8 and 1.3 ppm).

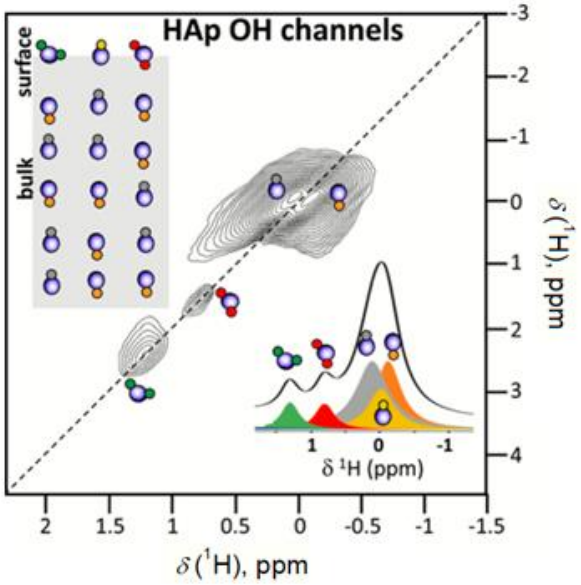

Fig. 5.4.2 Combination of ^{1}H 2D DQ-SQ spectrum, ^{1}H MAS NMR spectrum and a schematic representation of the possible configurations of different columnar OH channels in hydroxyapatite crystalline particles (in the bulk and at the surface) as well as organization of structured surface water molecules aligned with OH inside the channels. More details in the text. (adapted from M.B. Osman et.al. [86])

The H-bonded O–H stretching band in FTIR spectra was identified in many works on CaHAs and related systems [87, 161-164]. However, this band usually is taken as the unity without getting into its shape and structure. Water clusters were revealed in nano-CaHAs in the present work for the first time. The bands of water dimer, tetramer, hexamer and in the commercial sample maybe even $n \geq 6$ were resolved at 2900 - 3600 cm^{-1} (Fig. 5.4.3). The structure and size of formed cluster depends on the hydration level. Hexamer- or even higher structures were observed only in the samples containing significant amount of adsorbed water (Fig. 5.4.3 a, c). The amount of adsorbed water in the studied nano-CaHAs was probed using the intensity of the broad ^{1}H signal at ca 5.1 ppm normalized with respect to OH^- peak at ~ 0 ppm. Thus, the NMR data perfectly correlate with those obtained by FTIR spectroscopy.

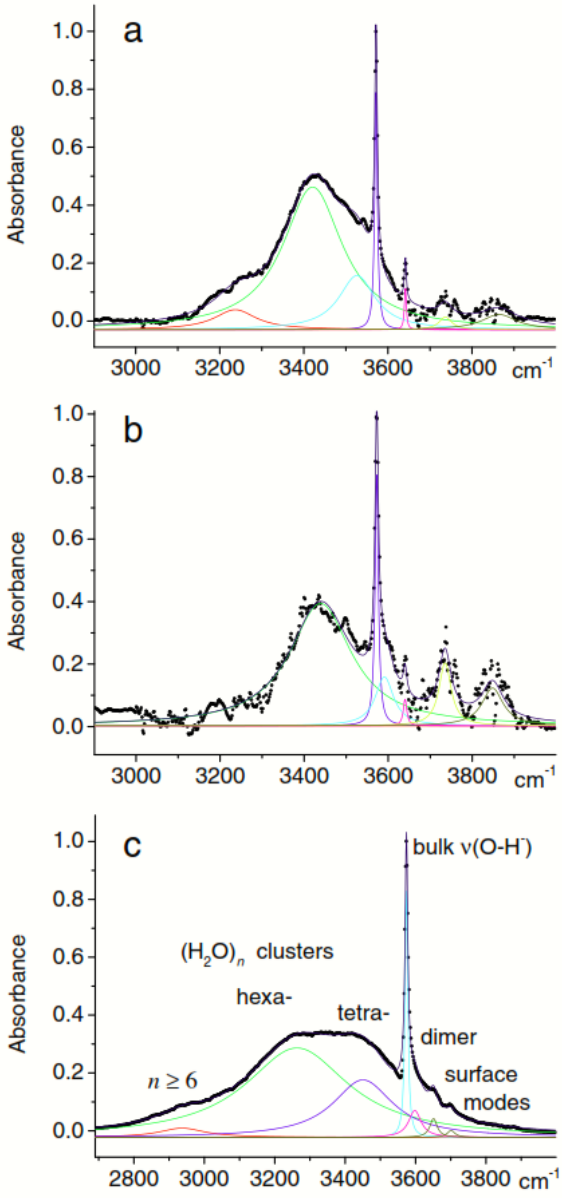

Fig. 5.4.3 FTIR spectra of nano-structured CaHAs prepared via the sol-gel synthesis routes using various complexing agents: a - ethylene glycol; b - tartaric acid; c - commercial. The base line was corrected drawing the line through the end points of this range. The intensities were normalized with respect to the peak of ν(O-H⁻)in the bulk at 3573 ± 1 cm^{-1}

Concluding remarks

- The joint application of FTIR and NMR methods allowed to reveal very fine details in the state of water and in the structural organization of OH groups. This could not be achieved applying these methods separately either because of difficulties assigning the observed spectral features or due to the overflow of information.

- Being able to probe the presence of PO_4, H_XPO_4, OH, and water at the surface of hydroxyapatite samples, could be very useful in describing the respective role of these various surface entities in different fields of application of the biomimetic hydroxyapatite systems.

- Water cluster structure was revealed by FTIR spectroscopy in nano-structured CaHAs for the first time. The bands of water dimer, tetramer, hexamer and several surface O–H and P–O–H modes were resolved at 2900 - 3900 cm^{-1} and assigned comparing with the spectra of water in argon matrix and in CCl_4.

CONCLUDING REMARKS OF DISSERTATION

The results of this dissertation demonstrated the versatility of NMR spectroscopy addressing potential future developments of nano-structure materials and NMR-based methods applied in clinical routine. Four fields of research showing the utility of NMR spectroscopy were covered:

1. NMR-based imaging modality (MRS) for prostate malignance identification analyzing spectral behaviour of present metabolites.

2. Water diffusion and spin–lattice relaxation processes in aqueous solutions of gadolinium (Gd)-based upconverting nanoparticles (UCNPs) as potential multimodal MRI contrast agents (CAs) working over a broad range of imaging field strengths used in clinical routine.

3. Temperature and composition effects on the phase behavior, slow self-assembling processes and tautomeric equilibrium in aqueous solutions of Sunset yellow (SSY) as one of the lyotropic chromonic liquid crystals, which promise the innovations in the drug-delivery as well as in the creation of a new generation of medical diagnostic tools - small and portable biosensors.

4. States of water and hydrogen-bond clustering process of molecules confined in series of calcium hydroxyapatites (CaHAs) as modern nano-structured materials that are used in reconstructive surgery for the treatment of enamel and bone defects.

REFERENCES

[1] D. Patkar, V. Jadhav, Ch. Jathar, New Advances in MRI, JIMSA, **26**, 59-64, (2013).

[2] P.D. Afonso, V.V. Mascarenhas, Imaging techniques for the diagnosis of soft tissue tumors, Reports in Medical Imaging, **8**, 63–70, (2015).

[3] A.E. Chang, Y.L. Matory, A.J. Dwyer, S.C. Hill, M.E. Girton, S.M. Steinberg, R.H. Knop, J.A. Frank, D. Hyams, J.L. Doppman, Magnetic resonance imaging versus computed tomography in the evaluation of soft tissue tumors of the extremities, Ann Surg. **205**, 340–348, (1987).

[4] D.V. Hingorani, A.S. Bernstein, M.D. Pagel, A review of responsive MRI contrast agents: 2005-2014. Contrast Media Mol Imaging, **10**, 245–265, (2014).

[5] S.S. Alshowiman, A.K. Alswailem, O.A. Almohizy, A.A. Alfawaz, A. Aziz, I. Alshaikh, MRI Contrast Agents: Developments, Challenges, and Future Trends, IOSR Journal of Pharmacy, **8**, 15-26, (2018).

[6] J. Kudr, Y. Haddad, L. Richtera, Z. Heger, M. Cernak, V. Adam, O. Zitka, Magnetic Nanoparticles: From Design and Synthesis to Real World Applications, Nanomaterials, **7**, 243 (29), (2017).

[7] Y. Luo, W. Zhang, Z. Liao, S. Yang, S. Yang, X. Li, F. Zuo, J. Luo, Role of Mn^{2+} Doping in the Preparation of Core-Shell Structured Fe_3O_4@upconversion Nanoparticles and Their Applications in T1/T2-Weighted Magnetic Resonance Imaging, Upconversion Luminescent Imaging and Near-Infrared Activated Photodynamic Therapy, Nanomaterials, **8**, 466 (15), (2018).

[8] T.F. Budinger, M.D. Bird, L. Frydman, J.R. Long, T. H. Mareci, W.D. Rooney, B. Rosen, J.F. Schenck, V.D. Schepkin, A.D. Sherry, D.K. Sodickson, Toward 20 T magnetic resonance for human brain studies: opportunities for discovery and neuroscience rationale, MAGMA, **29**, 617-639, (2016).

[9] A. Nowogrodzki, The world's strongest MRI machines are pushing human imaging to new limits, Nature, **563**, 24-26, (2018).

[10] M. Priola, S.M. Priola, D. Gned, E. Piacibello, D. Sardo, G. Parvis, D. Torti, F. Ardissone, A. Veltri. JMRI, **44**, 758-769, (2016).

[11] S. Verma, A. Rajesh, J. J. Fütterer, B. Turkbey, T.W.J. Scheenen, Y. Pang, P.L. Choyke, J. Kurhanewicz, Prostate MRI and 3D MR spectroscopy: how we do it, AJR, **194**, 1414-1426, (2010).

[12] C.M. Rios, M.P. McAndrews, W. Logan, T. Krings, D. Lee, E. Widjaja, MRI in the evaluation of localization-related epilepsy, JMRI, **44**, 12-22, (2016).

[13] S.C. Partridge, N. Nissan, H. Rahbar, A.E. Kitsch, E.E. Sigmund, Diffusion-weighted breast MRI: Clinical applications and emerging techniques, JMRI, **45**, 337-355, (2017).

[14] A. Capati, O. B. Ijare, T. Bezabeh, Diagnostic Applications of Nuclear Magnetic Resonance–Based Urinary Metabolomics, Magnetic Resonance Insights, **10**, 1-12, (2017).

[15] A. Fillmer, T. Kirchner, D. Cameron, A. Henning, Constrained Image-Based B_0 Shimming Accounting for "Local Minimum Traps" in the Optimization and Field Inhomogeneities Outside the Region of Interest, Magn Reson Med, **73**, 1370-1380, (2015).

[16] A. Hock, L. Valkovic, A. Geier, T. Kuntzen, P. Boesiger, A. Henning, Navigator based respiratory gating during preparation and acquisition phases for proton liver spectroscopy at 3T, NMR Biomed, **27**, 348-355, (2014).

[17] A. Marsman, V. O. Boer, P. Luijten, H. Pol, D. W.J. Klomp, R. Mandl, Detection of glutamate alterations in the human brain using 1H-MRS: Comparison of STEAM and sLASER at 7T, Frontiers in Psychiatry, **8**, 60-68, (2017).

[18] G. Oeltzschner, N. Puts, K.L. Chan, V.O. Boer, P. Barker, R. Edden, Richard, Dual-volume excitation and parallel reconstruction for J-difference-edited MR spectroscopy, Magnetic resonance in medicine, **77**, 16-22, (2016).

[19] B. Blasiak, F.C.J.M. van Veggel, B. Tomanek, Applications of Nanoparticles for MRI Cancer Diagnosis and Therapy, Journal of Nanomaterials, **2013**, 1-12, (2013).

[20] N. Zhu, H. Ji, P. Yu, J. Niu, M.U. Farooq, M.W. Akram, I.O. Udego, H. Li, X. Niu, Surface Modification of Magnetic Iron Oxide Nanoparticles, Nanomaterials, **8**, 810 (27), (2018).

[21] L. Jacques, S.A. Dean, Advances in gadolinium-based MRI contrast agent designs for monitoring biological processes in vivo, Curr Opin Chem Biol, **45**, 121-130, (2018).

[22] K.H. Choi, K.C. Nam, U.H. Kim, G. Cho, J.S. Jung, B.J. Park, Optimized Photodynamic Therapy with Multifunctional Cobalt Magnetic Nanoparticles. Nanomaterials, **7**, 144 (13), (2017).

[23] A. Kiania, A. Esquevina, N. Lepareurc, P. Bourguetc, F. Le Jeunec, J.Y. Gauvrit, Main applications of hybrid PET-MRI contrast agents: a review, Contrast Media Mol. Imaging, **11**, 92–98, (2016).

[24] Y.J. Lu, P.Y. Lin, P.H. Huang, C.Y. Kuo, K. Shalumon, M.Y. Chen, J.P. Chen, Magnetic Graphene Oxide for Dual Targeted Delivery of Doxorubicin and Photothermal Therapy, Nanomaterials, **8**, 193 (20), (2018).

[25] F. Leng, F. Liu, Y. Yang, Y. Wu, W. Tian, Strategies on Nanodiagnostics and Nanotherapies of the Three Common Cancers, Nanomaterials, **8**, 202 (15), (2018).

[26] E. Cazares-Cortes, M. Nerantzaki, J. Fresnais, C. Wilhelm, N. Griffete, C. Ménager, Magnetic Nanoparticles Create Hot Spots in Polymer Matrix for Controlled Drug Release, Nanomaterials, **8**, 850 (11), (2018).

[27] K. Dukenbayev, I.V. Korolkov, D.I. Tishkevich, A.L. Kozlovskiy, S.V. Trukhanov, Y.G. Gorin, E.E. Shumskaya, E.Y. Kaniukov, D.A. Vinnik, M.V. Zdorovets, et.al, Fe_3O_4 Nanoparticles for Complex Targeted Delivery and Boron Neutron Capture Therapy, Nanomaterials, **9**, 494 (19), (2019).

[28] I. Giouroudi, G. Kokkinis, Recent Advances in Magnetic Microfluidic Biosensors, Nanomaterials, **7**, 171 (10), (2017).

[29] Y. Luo, E. C. Alocilja, Portable nuclear magnetic resonance biosensor and assay for a highly sensitive and rapid detection of foodborne bacteria in complex matrices, J Biol Eng, **11**, 1-8, (2017).

[30] H. Lee, E. Sun, D. Ham, R. Weissleder, Chip-NMR biosensor for detection and molecular analysis of cells, Nat Med, **14**, 869–874, (2008).

[31] W.C. Lin, C.C. Chuang, C.J. Chang, Y.H. Chiu, M. Yan, C.M. Tang, The Effect of Electrode Topography on the Magnetic Properties and MRI Application of Electrochemically-Deposited, Synthesized, Cobalt-Substituted Hydroxyapatite, Nanomaterials, **9**, 200 (14), (2019).

[32] E. Díaz, M.B. Valle, S. Ribeiro, S. Lanceros-Mendez, J.M. Barandiarán, Development of Magnetically Active Scaffolds for Bone Regeneration, Nanomaterials, **8**, 678 (16), (2018).

[33] N. Agarwal, M.S. Nair, A. Mazumder, K.M. Poluri, *Characterization of Nanomaterials: Advances and Key Technologies*, Woodhead Publishing, pp 61-102, (2018).

[34] L.C. Costello, R.B. Franklin, The clinical relevance of the metabolism of prostate cancer; zinc and tumor suppression: connecting the dots, Mol Cancer, **5**, 17 (13), (2006).

[35] J.K. Furuyama, N.E. Wilson, B.L. Burns, R. Nagarajan, D.J. Margolis, M.A. Thomas, Application of Compressed Sensing to Multidimentional Spectroscopic Imaging in Human Prostate, Magnetic resonance in medicine, **67,** 1499-1505, (2012).

[36] R.S. Kelly, J.A. Sinnott, J.R. Rider, E.M. Ebot, T. Gerke, M. Bowden, A. Pettersson, M. Loda, H.D. Sesso, P.W. Kantoff, et al, The role of tumor metabolism as a driver of prostate cancer progression and lethal disease: results from a nested case-control study, Cancer Metab, **4**, 22 (9), (2016).

[37] E. Eidelman, J. Twum-Ampofo, J. Ansari, M.M. Siddiqui, The Metabolic Phenotype of Prostate Cancer, Front Oncol, **7,** 1-6, (2017).

[38] M.A. Hussain, G. Juergen, O. Rima, The role of choline in prostate cancer, Clinical Biochemistry, **45**, 1548-1553, (2012).

[39] L.A. Vandergrift, E.A. Decelle, J. Kurth, S. Wu, T.L. Fuss, E.M. DeFeo, E.F. Halpern, M. Taupitz, W.S. McDouga, A.F. Olumi, et al, Metabolomic Prediction of Human Prostate Cancer Aggressiveness: Magnetic Resonance Spectroscopy of Histologically Benign Tissue, Scientific reports, **8**, 4997 (12), (2018).

[40] R.S. Kelly, M.G. Vander Heiden, E. Giovannucci, L.A. Mucci, Metabolomic Biomarkers of Prostate Cancer: Prediction, Diagnosis, Progression, Prognosis, and Recurrence, Cancer Epidemiol Biomarkers Prev, **25**, 887–906, (2016).

[41] L.R. Euceda, M.K. Andersen, M.B. Tessem, S.A. Moestue, M.T. Grinde, T.F. Bathen, NMR-Based Prostate Cancer Metabolomics, In: *Prostate Cancer. Methods in Molecular Biology*, Culig Z. (Ed), vol 1786, Humana Press, New York, NY, pp 237-257, (2018).

[42] R. García-Figueiras, S. Baleato-González, A.R. Padhani, L. Oleaga, J.C. Vilanova, A. Luna, J.C. Cobas Gómez, Proton magnetic resonance spectroscopy in oncology: the fingerprints of cancer?, Diagn Interv Radiol, **22**, 75–89, (2015).

[43] F. De Martino, F. Esposito, P.F. van de Moortele, N. Harel, E. Formisano, R. Goebel, K. Ugurbil, E. Yacoub, Whole brain high-resolution functional imaging at ultrahigh magnetic fields: an application to the analysis of resting state networks, Neuroimage, **57**, 1031–1044, (2011).

[44] V. Brandejsky, C. Boesch, R. Kreis, Proton diffusion tensor spectroscopy of metabolites in human muscle in vivo, **73**, 481-487, (2015).

[45] A.E. Ercan, A. Techawiboonwong, M.J. Versluis, A.G. Webb, I. Ronen, Diffusion-Weighted Chemical Shift Imaging of Human Brain Metabolites at 7T, Magnetic Resonance in Medicine, **73**, 2053–2061, (2015).

[46] R. A. de Graaf, H. M. de Feyter, D. L. Rothman, High-sensitivity, broadband-decoupled (13) C MR spectroscopy in humans at 7T using two-dimensional heteronuclear single-quantum coherence, Magn Reson Med. **74,** 903–914, (2015).

[47] T.A.D. Smith, S.M. Phyu, K.S. Alzyoud, C.C. Tseng, Response Detection of Castrate-Resistant Prostate Cancer to Clinically Utilised and Novel Treatments by Monitoring Phospholipid Metabolism, BioMed Research International, **2017**, 4793465 (7), (2017).

[48] A. Santos-Díaz, M. D. Noseworthy, Comparison of compressed sensing reconstruction algorithms for ^{31}P magnetic resonance spectroscopic imaging, Magnetic Resonance Imaging, **59**, 88-96, (2019).

[49] I. Chatnuntawech, B. Gagoski, B. Bilgic, S.F. Cauley, K. Setsompop, E. Adalsteinsson, Accelerated ^{1}H MRSI using randomly undersampled spiral-based k-space trajectories, MRM, **74**, 13–24 (2015).

[50] I.K. Steinseifer, J.J. van Asten, E. Weiland, T.W. Scheenen, M.C. Maas, A. Heerschap, Improved volume selective (1) H MR spectroscopic imaging of the prostate with gradient offset independent adiabaticity pulses at 3 tesla, MRM, **74**, 915-924, (2015).

[51] J. Near, R. Edden, C.J. Evans, R. Paquin, A. Harris, P. Jezzard, Frequency and phase drift correction of magnetic resonance spectroscopy data by spectral registration in the time domain, MRM, **73**, 44-50, (2015).

[52] G. Öz, J.R. Alger, P.B. Barker, R. Bartha, A. Bizzi, C. Boesch, P.J. Bolan, K.M. Brindle, C. Cudalbu, A. Dinçer, et al, Clinical Proton MR Spectroscopy in Central Nervous System Disorders, Radiology, **270**, 658-679, (2014).

[53] G.A. Pereira, C.F.G.C. Geraldes, Design and Optimization of Gadolinium Based Contrast Agents for Magnetic Resonance Imaging, Ann. Magn. Reson, **6**, 1–33, (2007).

[54] M. Rohrer, H. Bauer, J. Mintorovich, M. Requardt, H.J. Weinmann, Comparison of magnetic properties of MRI contrast media solutions at different magnetic field strengths, Invest. Radiol, **40**, 715–724, (2005).

[55] P. Caravan, Ch.T Farrar, L. Frullano, R. Uppal, Influence of molecular parameters and increasing magnetic field strength on relaxivity of gadolinium- and manganese-based T1 contrast agents,Contrast Media Mol Imaging, **4**, 89–100, (2009).

[56] V. Jacques, S. Dumas, WCh. Sun, J.S. Troughton, M.T. Greenfeld, P. Caravan, High relaxivity MRI contrast agents part 2: Optimization of inner- and second-sphere relaxivity, Invest. Radiol, **45**, 613–624, (2010).

[57] A.M. Panich, N.A. Sergeev, Towards Determination of Distances Between Nanoparticles and Grafted Paramagnetic Ions by NMR Relaxation, Appl. Magn. Reson, **49**, 195-208, (2018).

[58] F.C.J.M. van Veggel, C. Dong, N.J.J. Johnson, J. Pichaandi, Ln^{3+}-doped nanoparticles for upconversion and magnetic resonance imaging: some critical notes on recent progress and some aspects to be considered, Nanoscale, **4**, 7309-7321, (2012).

[59] L. Dongdong, S. Qiyue, D. Yan, J. Jianqing, Phase-, shape- and size-controlled synthesis of $NaYF_4$:Yb^{3+},Er^{3+} nanoparticles using rare-earth acetate precursors, J. Rear Earths, **32**, 1032-1036, (2014).

[60] C. Liu, Z. Gao, J. Zeng, Y. Hou, F. Fang, Y. Li, R. Qiao, L. Shen, H. Lei, W. Yang, M. Gao, Magnetic/upconversion fluorescent $NaGdF_4$:Yb,Er nanoparticle-based dual-modal molecular probes for imaging tiny tumors in vivo, ACS Nano, **7**, 7227-7240, (2013).

[61] Q. Li, *Liquid Crystals Beyond Displays: Chemistry, Physics, and Applications*, Q. Li (Ed), Wiley: Hoboken, p 600, (2012).

[62] Y.S. Lee, *Self-Assembly and Nanotechnology: A Force Balance Approach*, Wiley: Hoboken, p 344, (2008).

[63] H.S. Park, O.D. Lavrentovich, Lyotropic Chromonic Liquid Crystals: Emerging Applications, In: *Liquid Crystals Beyond Displays: Chemistry, Physics, and Applications*; Q. Li (Ed), Wiley: Hoboken, 449−484, (2012).

[64] V. R. Horowitz, L. A. Janowitz, A. L. Modic, P. A. Heiney, P. J. Collings, Aggregation Behavior and Chromonic Liquid Crystal Properties of an Anionic Monoazo Dye, Phys. Rev, E, **72**, 041710 (10). (2005).

[65] J.F. De Souza, K.D.S. Pontes, T.F.R. Alves, V.A. Amaral, M.D.A. Rebelo, M.A. Hausen, M.V. Chaud, Spotlight on Biomimetic Systems Based on Lyotropic Liquid Crystal, Molecules, **22**, 419 (1-15), (2017).

[66] Y.S. Lee, Assembly of Lyotropic Liquid Crystals with Solid Crystal's Structural Order Translated from the Lipid Rafts in Cell Membranes, J. Am. Chem. Soc, **139**, 17044−17051, (2017).

[67] J. Lydon, Chromonic Review, J. Mater. Chem, **20**, 10071−10099, (2010).

[68] J. Lydon, Chromonic Liquid Crystalline Phases, Liq. Cryst, **38**, 1663−1681, (2011).

[69] H. S. Park, S. W. Kang, L. Tortora, Y. Nastishin, D. Finotello, S. Kumar, O.D. Lavrentovich, Self-Assembly of Lyotropic Chromonic Liquid Crystal Sunset Yellow and Effects of Ionic Additives, J. Phys. Chem. B, **112**, 16307−16319, (2008).

[70] S.V. Shiyanovskii, O.D. Lavrentovich, T. Schneider, T. Ishikawa, I.I. Smalyukh, C.J. Woolverton, G.D. Niehaus, K.J. Doane, Lyotropic Chromonic Liquid Crystals for Biological Sensing Applications, Mol. Cryst. Liq. Cryst, **434**, 259−270, (2005).

[71] P. Popov, L. Honaker, E. Kooijman, E. Mann, A. Jákli, A liquid crystal biosensor for specific detection of antigens, Sensing and Bio-Sensing Research, **8**, 31-35, (2016).

[72] E. Otón, J. Otón, M. Caño-García, J. Escolano, X. Quintana, and M. Geday, Rapid detection of pathogens using lyotropic liquid crystals, Opt. Express, **27**, 10098-10107, (2019).

[73] F. Chami, M.R. Wilson, Molecular Order in a Chromonic Liquid Crystal: A Molecular Simulation Study of the Anionic Azo Dye Sunset Yellow, J. Am. Chem. Soc, **132**, 7794−7802, (2010).

[74] A. Yamaguchi, G. P. Smith, Y. Yi, C. Xu, S. Biffi, F. Serra, T. Bellini, C. Zhu, N.A. Clark, Phases and Structures of Sunset Yellow and Disodium Cromoglycate Mixtures in Water, Phys. Rev. E, **93**, 012704. (2016).

[75] S. Coussan, P. Roubin, J.P. Perchard, Infrared induced isomerizations of water poly- mers trapped in nitrogen matrix, Chem. Phys, **324**, 527–540, (2006).

[76] I. Doroshenko, G. Pitsevich, V. Sablinskas, J. Ceponkus, V. Pogorelov, V. Balevicius, The initial stages of clustering of water molecules: matrix isolation FTIR/2DCOR study and the concept of combinatorial band broadening, *Book of Abstracts of XXIth International Conference*

Horizons in Hydrogen Bond Research, Wroclaw University, Wroclaw, Poland, P5 September, pp 13–18, (2015).

[77] J. Ceponkus, P. Uvdal, B. Nelander, Water tetramer, pentamer, and hexamer in inert matrices, J. Phys. Chem. A, **116**, 4842–4850, (2012).

[78] J. Ceponkus, A. Engdahl, P. Uvdal, B. Nelander, Structure and dynamics of small water clusters, trapped in inert matrices, Chem. Phys. Lett, **581**, 1–9, (2013).

[79] T. Köddermann, F. Schulte, M. Huelsekopf, R. Ludwig, Formation of water clusters in a hydrophobic solvent, Angew. Chem. Int. Ed, **42**, 4904–4908, (2003).

[80] Martí, M.C. Gordillo, Effects of confinement on the vibrational spectra of liquid water adsorbed in carbon nanotubes, Phys. Rev. B, **63**, 165430 (5), (2001).

[81] Y. Xu, T. Watermann, H.H. Limbach, T. Gutmann, D. Sebastiani, G. Buntkowsky, Water and small organic molecules as probes for geometric confinement in well-ordered mesoporous carbon materials, Phys. Chem. Chem. Phys, **16**, 9327–9336, (2014).

[82] B.Grünberg, T. Emmler, E. Gedat, I. Shenderovich, G.H. Findenegg, H.H. Limbach, G. Buntkowsky, Hydrogen bonding of water confined in mesoporous silica MCM-41 and SBA-15 studied by ^{1}H solid-state NMR, Chem. Eur. J, **10**, 5689–5696, (2004).

[83] R.Z. Le Geros, J.P. Le Geros, Hydroxyapatite, In: *Bioceramics and their Clinical Applications*, T. Kokubo (Ed), Woodhead Publishing, Cambridge, pp 367–394, (2008).

[84] R.Z. Le Geros, *Calcium Phosphates in Oral Biology and Medicine*, Karger, Basel, 201 p, (1991).

[85] P.W. Brown, B. Constantz, *Hydroxyapatite and Related Materials*, CRC Press, 368 p, (1994).

[86] M. Ben Osman, S. Diallo-Garcia, V. Herledan, D. Brouri, T. Yoshioka, J. Kubo, Y. Millot, G. Costentin, Discrimination of surface and bulk structure of crystalline hydroxyapatite nanoparticles by NMR, J. Phys. Chem. C, **119**, 23008–23020, (2015).

[87] J. Kolmas, A. Jaklewicz, A. Zima, M. Bućko, Z. Paszkiewicz, J. Lis, A. Ślosarczyk, W. Kolodziejski, Incorporation of carbonate and magnesium ions into synthetic hydroxyapatite: the effect on physicochemical properties, J. Mol. Struct, **987**, 40–50, (2011).

[88] N. A. Zakharov, I. A. Polunina, K. E. Polunin, N. M. Rakitina, E. I. Kochetkova, N. P. Sokolova, V. T. Kalinnikov, Calcium

Hydroxyapatite for Medical Applications, Inorganic Materials, **40**, 641-648, (2004).

[89] E. M. Purcell, H. C. Torrey, and R. V. Pound, Resonance Absorption by Nuclear Magnetic Moments in a Solid, Phys. Rev, **69**, 37-38, (1946).

[90] F. Bloch, W. W. Hansen, Martin Packard, Nuclear Induction, Phys. Rev, **69**, 127, (1946).

[91] M.H. Levit, *Spin Dynamics: Basics of Nuclear Magnetic Resonance*, 2nd edition, John Wiley and Sons Ltd, 724 p, (2008).

[92] P.C.Lauterbur, Image formation by induced local interactions: examples employing nuclear magnetic resonance, Nature, **242**, 190-191, (1973).

[93] P.A. Bottomley, T.H. Foster, R.E. Argersinger, LM. Pfeiffer, A review of normal tissue hydrogen NMR relaxation times and relaxation mechanisms from 1–100 MHz: Dependence on tissue type, NMR frequency, temperature, species, excision, and age, Med Phys, **11**, 425-448, (1984).

[94] M. J. de Bazelaire, G. D. Duhamel, N. M. Rofsky, D. C. Alsop, MR Imaging Relaxation Times of Abdominal and Pelvic Tissues Measured in Vivo at 3.0 T: Preliminary Results Cedric, Radiology, **230**, 652-659, (2004).

[95] U. Klose, Measurement sequences for single voxel proton MR spectroscopy, European Journal of Radiology, **67**, 194-201, (2008).

[96] T.W.J. Scheenen, G. Gambarota, E. Weiland, D.W.J. Klomp, J.J. Fütterer, J.O. Barentsz, A. Heerschap, Optimal timing for in vivo ^{1}H-MR spectroscopic imaging of the human prostate at 3T, Magn Reson Med, **53**, 1268-1274, (2005).

[97] S.F. Keevil, Spatial localization in nuclear magnetic resonance spectroscopy, Phys. Med. Biol, **51**, R579–R636, (2006).

[98] A. Skoch, F. Jiru, J. Bunke, Spectroscopic imaging: Basic principles, European Journal of Radiology, **67**, 230–239, (2008).

[99] M. Hajek, M. Dezortova, Introduction to clinical in vivo MR spectroscopy, European Journal of Radiology, **67**, 185–193, (2008).

[100] S. Verma, A. Rajesh, J.J. Fütterer, B. Turkbey, T.W.J. Scheenen, Y. Pang, P.L. Choyke, J. Kurhanewicz, Prostate MRI and 3D MR spectroscopy: how we do it, AJR, **194**, 1414-1426, (2010).

[101] D. Bertholdo, A. Watcharakorn, M. Castillo, Brain Proton Magnetic Resonance Spectroscopy Introduction and Overview, Neuroimag Clin N Am, **23**, 359–380, (2013).

[102] M.E. Mycielska, A. Patel, N. Rizaner, M.P. Mazurek, H. Keun, A. Patel, V. Ganapathy, M.B. Djamgoz, Citrate transport and metabolism in mammalian cells. Prostate epithelial cells and prostate cancer, BioEssays, **31**, 10-20, (2009).

[103] G. Bellomo, F. Marcocci, D. Bianchini, E. Mezzenga, V. D'Errico, E. Menghi, R. Zannoli, A. Sarnelli, MR Spectroscopy in Prostate Cancer: New Algorithms to Optimize Metabolite Quantification, PLoS ONE, **11**, 1-18, (2016).

[104] J. Weis, C. von Below, A. Tolf, F. Ortiz-Nieto, C. Wassberg, M. Häggman, S. Ladjevardi, H. Ahlström, Quantification of metabolite concentrations in benign and malignant prostate tissues using 3D proton MR spectroscopic imaging, J. Magn. Reson. Imaging, **45**, 1232-1240, (2017).

[105] M. Piotto, F.M. Moussallieh, A. Neuville, J.P. Bellocq, K. Elbayed, I.J. Namer, Towards real-time metabolic profiling of a biopsy specimen during a surgical operation by 1H high resolution magic angle spinning nuclear magnetic resonance: a case report, J Med Case Rep, **6**, 6-22, (2012).

[106] O. Beckonert, M. Coen, H.C. Keun, Y. Wang, T.M.D. Ebbels, E. Holmes, J.C. Lindon, J.K. Nicholson, High-resolution magic-angle-spinning NMR spectroscopy for metabolic profiling of intact tissues, Nature Protocols, **5**, 1019–1032, (2010).

[107] V. Klimavicius, A. Kareiva, V. Balevicius, Solid-State NMR Study of Hydroxyapatite Containing Amorphous Phosphate Phase and Nanostructured Hydroxyapatite: Cut-Off Averaging of CP-MAS Kinetics and Size Profiles of Spin Clusters, The Journal of Physical Chemistry C, **118**, 28914-28921, (2014).

[108] K. Hammami, J. Elloumi, S. Aifa, C. Drouet, H.E. Feki, Synthesis and Characterization of Hydroxyapatite Ceramics Organofunctionalized with ATP (Adenosine Triphosphate), Journal of Advances in Chemistry, **9**, 1787-1797, (2014).

[109] T. Polenova, R. Gupta, A. Goldbourt, Magic angle spinning NMR spectroscopy: a versatile technique for structural and dynamic analysis of solid-phase systems, Anal Chem, **87**, 5458–5469, (2015).

[110] S. Penzel, A. Oss, M.L. Org, A. Samoson, A. Böckmann, M. Ernst, B.H. Meier, Spinning faster: protein NMR at MAS frequencies up to 126 kHz, J Biomol NMR, **73**, 19-29, (2019).

[111] Y. Vasavi, N. Parthiban, S. Dinakaran, D. Banji, N. Srisutherson, S. Ghosh, M. Vinay, K. Chakravarthy, Heteronuclear Multible Bond Correlation Spectroscopy-An Overview, International Journal of PharmTech Research, **3**, 1410-1422, (2011).

[112] J.Keeler, Chapter 7, Two-Dimensional NMR, In: *Understanding NMR Spectroscopy*, University of Cambridge, Department of Chemistry, pp 1-30, (2002).

[113] P.J. Hore, *Nuclear Magnetic Resonance*, 2nd edition, Oxford University Press, pp 93-99, (2015).

[114] R.D.A. Alvares, A. Gautam, R.S. Prosser, F.C.J.M. van Veggel, P.M. Macdonald, Shell versus Core Dy^{3+} Contributions to NMR Water Relaxation in Sodium Lanthanide Fluoride Core–Shell Nanoparticles. An Investigation Using O-17 and H-1 NMR, J. Phys. Chem, **121**, 17552-17558, (2017).

[115] V.C. Pierre, S.M. Harris, S.L. Pailloux, Comparing Strategies in the Design of Responsive Contrast Agents for Magnetic Resonance Imaging: A Case Study with Copper and Zinc, Acc. Chem. Res, **51**, 342-351, (2018).

[116] D. Ni, W. Bu, E.B. Ehlerding, W. Cai, J. Shi, Engineering of inorganic nanoparticles as magnetic resonance imaging contrast agents, Chem. Soc. Rev, **46**, 7438-7468, (2017).

[117] D. Baziulyte-Paulaviciene, V. Karabanovas, M. Stasys, G. Jarockyte, V. Poderys, S. Sakirzanovas, R. Rotomskis. J. Beilstein, Synthesis and functionalization of $NaGdF_4$:Yb,Er@$NaGdF_4$ core-shell nanoparticles for possible application as multimodal contrast agents, Nanotechnol, **8**, 1815-1824, (2017).

[118] M. Ding, D. Chen, S. Yin, Z. Ji, J. Zhong, Y. Ni, C. Lu, Z. Xu, Simultaneous morphology manipulation and upconversion luminescence enhancement of β-$NaYF_4$:Yb^{3+}/Er^{3+} microcrystals by simply tuning the KF dosage, Sci. Rep, **5**, 12745 (14), (2015).

[119] J. Ceponkus, A. Engdahl, P. Uvdal, B. Nelander, Structure and dynamics of small water clusters, trapped in inert matrices, Chem. Phys. Le, **581**, 1–9, (2013).

[120] T. Köddermann, F. Schulte, M. Huelsekopf, R. Ludwig, Formation of water clusters in a hydrophobic solvent, Angew. Chem. Int. Ed. **42**, 4904–4908, (2003).

[121] S. Kareiva, V. Klimavicius, A. Momot, J. Kausteklis, A. Prichodko, L. Dagys, F. Ivanauskas, S. Sakirzanovas, V. Balevicius, A. Kareiva, Sol-

gel synthesis, phase com- position, morphological and structural characterization of $Ca_{10}(PO_4)_6(OH)_2$: XRD, FTIR, SEM, 3D SEM and solid-state NMR studies, J. Mol. Struct, **1119**, 1–11, (2016).

[122] A. C. Dona, M. Kyriakides, F. Scott, E. A.Shephard, D. Varshavi, K. Veselkov, J. R. Everett, A guide to the identification of metabolites in NMR-based metabonomics/metabolomics experiments, Computational and Structural Biotechnology Journal, **14**, 135–153, (2016).

[123] A.I. Hashim, X. Zhang, J.W. Wojtkowiak, G.V. Martinez, R.J. Gillies, Imaging pH and Metastasis, NMR Biomed, **24**, 582-591, (2011).

[124] N.T. Viola-Villegas, S.D. Carlin, E. Ackerstaff, K.K. Sevak, V. Divilov, I. Serganova, N. Kruchevsky, M. Anderson, R.G. Blasberg, O.A. Andreev, et al, Understanding the pharmacological properties of a metabolic PET tracer in prostate cancer, PNAS, **111**, 7254-7259, (2014).

[125] N.M. Pedrosa, J. Sloboom, Quality management in in-vivo proton MRS, Analytical Biochemistry, **529**, 98-116, (2017).

[126] K.M. Selnæs, I.S. Gribbestad, H. Bertilsson, A. Wright, A. Angelsen, A. Heerschap, M. Tessem, Spatially matched *in vivo* and *ex vivo* MR metabolic profiles of prostate cancer – investigation of a correlation with Gleason score, NMR Biomed, **26**, 600-606, (2013).

[127] I.G. Schoots, MRI in early prostate cancer detection: how to manage indeterminate or equivocal PI-RADS 3 lesions, Transl Androl Urol, **7**, 70-82, (2018).

[128] S.H. Polanec, K.P. Domenig, P. Brader, D. Georg, Sh. Shariat, C. Spick, M. Susani, Th. H. Helbich, P. A. Baltzer, Multiparametric MRI of the prostate at 3 T: limited value of 3D 1H-MR spectroscopy as a fourth parameter, World J Urol, **34**, 649-656, (2016).

[129] S. Ghai, M.A. Haider, Multiparametric-MRI in diagnosis of prostate cancer, Indian J Urol, **31**, 194–201, (2015).

[130] T.A. Flood, N. Schieda, Beyond the Gleason score: the prognostic significance of prostate cancer subtypes, Transl Androl Urol, **7**, S260–S261, (2018).

[131] P.A. DiCamillo, M.G. Swanson, Z.L. Tabatabai, J. Kurhanewicz, S.J. Nelson, Measurement of citrate chemical shift changes in HR-MAS NMR Spectra of Prostate Biopsies, Proccedings of ISMRM, **15**, (2007).

[132] E. Von Goldammer, H. G. Hertz, Molecular motion and structure of aqueous mixtures with nonelectrolytes as studied by nuclear magnetic relaxation methods, J. Phys. Chem, **74**, 3734-3755 (1970).

[133] V.I. Chizhik, Y.S. Chernyshev, A.V. Donets, V.V. Frolov, A.V. Komolkin, M.G. Shelyapina, *Magnetic Resonance and Its Applications*, Springer, p 206, (2014).

[134] X.Y. Zheng, K. Zhao, J. Tang, X.Y. Wang, L.D. Li, N.X. Chen, Y.J. Wang, S. Shi, X. Zhang, S. Malaisamy, et.al, Gd-Dots with Strong Ligand–Water Interaction for Ultrasensitive Magnetic Resonance Renography, ACS Nano, **11**, 3642-3650, (2017).

[135] F. Chen, W. Bu, S. Zhang, X. Liu, J. Liu, H. Xing, Q. Xiao, L. Zhou, W. Peng, L. Wang, J. Shi, Positive and Negative Lattice Shielding Effects Co-existing in Gd (III) Ion Doped Bifunctional Upconversion Nanoprobes, Adv. Funct. Mater, **21**, 4285-4294 (2011).

[136] N.J. Johnson, S. He, V.A. Nguyen Huu, A. Almutairi, Compact Micellization: A Strategy for Ultrahigh T1 Magnetic Resonance Contrast with Gadolinium-Based Nanocrystals, ACS Nano, **10**, 8299-8307, (2016).

[137] N.J.J. Johnson, W. Oakden, G.J. Stanisz, R.S. Prosser, F.C.J.M. van Veggel, Size-Tunable, Ultrasmall NaGdF4 Nanoparticles: Insights into Their T1 MRI Contrast Enhancement, Chem. Mater, **23**, 3714-3722, (2011).

[138] Y. Hou, R. Qiao, F. Fang, X. Wang, C. Dong, K. Liu, C. Liu, Z. Liu, H. Lei, F. Wang, M. Gao, $NaGdF_4$ Nanoparticle-Based Molecular Probes for Magnetic Resonance Imaging of Intraperitoneal Tumor Xenografts in Vivo, ACS Nano, **7**, 330-338, (2013).

[139] X. Ding, T.C. Stringfellow, J. R. Robinson, Self-Association of Cromolyn Sodium in Aqueous Solution Characterized by Nuclear Magnetic Resonance Spectroscopy, J. Pharm. Sci, **93**, 1351-1358, (2004).

[140] E. Troche-Pesqueira, M.M. Cid, A. Navarro-Vazquez, Disodium Cromoglycate: Exploiting its Properties as a NMR Weakaligning Medium for Small Organic Molecules, Org. Biomol. Chem, **12**, 1957−1965, (2014).

[141] D.J. Edwards, J.W. Jones, O. Lozman, A.P. Ormerod, M. Sintyureva, G.J.T. Tiddy, Chromonic Liquid Crystal Formation by Edicol Sunset Yellow, J. Phys. Chem. B, **112**, 14628−14636, (2008).

[142] X. Yao, K. Nayani, J.O. Park, M. Srinivasarao, Orientational Order of a Lyotropic Chromonic Liquid Crystal Measured by Polarized Raman Spectroscopy, J. Phys. Chem. B, **120**, 4508-4512, (2016).

[143] M.P. Renshaw, I.J. Day, NMR Characterization of the Aggregation State of the Azo Dye Sunset Yellow in the Isotropic Phase, J. Phys. Chem. B, **114**, 10032−10038, (2010).

[144] P. Gilli, V. Bertolasi, V. Ferretti, G. Gilli, Evidence for Intramolecular N−H···O Resonance-Assisted Hydrogen Bonding in β-Enaminones and Related Heterodienes. A Combined CrystalStructural, IR and NMR Spectroscopic, and Quantum-Mechanical Investigation, J. Am. Chem, Soc, **122**, 10405−10417, (2000).

[145] V. Klimavicius, Z. Gdaniec, J. Kausteklis, V. Aleksa, K. Aidas, V. Balevicius, NMR and Raman Spectroscopy Monitoring of Proton/Deuteron Exchange in Aqueous Solutions of Ionic Liquids Forming Hydrogen Bond: A Role of Anions, Self-Aggregation, and Mesophase Formation, J. Phys. Chem. B, **117**, 10211−10220, (2013).

[146] V. Balevicius, Z. Gdaniec, K. Aidas, NMR and DFT Study on Media Effects on Proton Transfer in Hydrogen Bonding: Concept of Molecular Probe with an Application to Ionic and Super-polar Liquids, Phys. Chem. Chem. Phys, **11**, 8592−8600, (2009).

[147] L. Joshi, S.W. Kang, D.M. Agra-Kooijman, S. Kumar, Concentration, Temperature, and pH Dependence of Sunset-Yellow Aggregates in Aqueous Solutions: An X-Ray Investigation, Phys. Rev. E, **80**, 041703 (8), (2009).

[148] V. Klimavicius, V. Bacevicius, Z. Gdaniec, V. Balevicius, Pulsed-field Gradient 1H NMR Study of Diffusion and Selfaggregation of Long-chain Imidazolium-based Ionic Liquids, J. Mol. Liq, **210**, 223−226, (2015).

[149] L. Wu, J. Lal, K.A. Simon, E. A. Burton, Y.Y. Luk, Nonamphiphilic Assembly in Water: Polymorphic Nature, Thread Structure, and Thermodynamic Incompatibility, J. Am. Chem. Soc, **131**, 7430−7443, (2009).

[150] S. Zhou, K. Neupane, Y.A. Nastishin, A.R. Baldwin, S. Shiyanovskii, O.D. Lavrentovich, S. Sprunt, Elasticity, Viscosity, and Orientational Fluctuations of a Lyotropic Chromonic Nematic Liquid Crystal Disodium Cromoglycate, Soft Matter, **10**, 6571-6581, (2014).

[151] V. Balevicius, K. Aidas, Temperature Dependence of ^{17}O NMR Shifts of Water: Entropy Effect, Appl. Magn. Reson, **32**, 363−376, (2007).

[152] Z.S. Davidson, Y. Huang, A. Gross, A. Martinez, T. Still, C. Zhou, P.J. Collings, R.D. Kamien, A.G. Yodh, Deposition and Drying Dynamics of Liquid Crystal Droplets, Nat. Commun, **8**, 15642 (7), (2017).

[153] I. Đurickovic, R. Claverie, P. Bourson, M. Marchetti, J.M. Chassot, M.D. Fontana, Water − Ice Phase Transition Probed by Raman Spectroscopy, J. Raman Spectrosc, **42**, 1408−1412, (2011).

[154] K. Saihara, Y. Yoshimura, S. Ohta, A. Shimizu, Properties of Water Confined in Ionic Liquids, Sci. Rep, **5** 10619 (10), (2015).

[155] J. Lu, I. Hung, A. Brinkmann, Z. Gan, X. Kong, G. Wu, Solid State ^{17}O NMR Reveals Hydrogen-Bonding Energetics: Not All LowBarrier Hydrogen Bonds Are Strong, Angew. Chem., Int. Ed, **56**, 6166−6170, (2017).

[156] V. Balevicius, V. Sablinskas, I. Doroshenko, V. Pogorelov, Propanol clustering in argon matrix: 2D FTIR correlation spectroscopy, Ukr. J. Phys, **56**, 855-860, (2011).

[157] I. Noda, Advances in two-dimensional correlation spectroscopy, Vibr. Spectrosc, **36**, 143-165, (2004).

[158] R.M. Bentwood, A.J. Barnes, W.J. Orville-Thomas, Studies of Intermolecular interactions by Matrix isolation Vibrational Spectroscopy. Self-association of Water, J. Mol. Spectr, **84**, 391-404, (1980).

[159] A. Engdahl, B. Nelander, On the structure of the water trimer. A matrix isolation study, J. Chem. Phys, **86**, 4831-4837, (1987).

[160] K. Ohno, M. Okimura, N. Akai, Y. Katsumoto, The effect of cooperative hydrogen bonding on the OH stretching-band shift for water clusters studied by matrix-isolation infrared spectroscopy and density functional theory, Phys. Chem. Chem. Phys, **7**, 3005-3014, (2005).

[161] L. Dagys, V. Klimavicius, J. Kausteklis, A. Chodosovskaja, V. Aleksa, A. Kareiva, V.Balevicius, Solid-state ^{1}H and ^{31}P NMR and FTIR spectroscopy study of static and dynamic structures in sol-gel derived calcium hydroxyapatites, Lith. J. Phys, **55**, 1-9, (2015).

[162] S. Diallo-Garcia, M. Ben Osman, J.M. Krafft, S. Boujday, C. Guylène, Discrimination of infrared fingerprints of bulk and surface POH and OH of hydroxyapatites, Catalysis Today, **226**, 81–88, (2014).

[163] J.A. Noble, C. Martin, H.J. Fraser, P. Roubin, S. Coussan, Unveiling the Surface Structure of Amorphous Solid Water via Selective Infrared Irradiation of OH Stretching Modes, J. Phys. Chem. Lett, **5**, 826-829, (2014).

[164] T. Ishikawa, A. Teramachi, H. Tanaka, A. Yasukawa, K. Kandori, Fourier Transform Infrared Spectroscopy Study of Deuteration of Calcium Hydroxyapatite Particles, Langmuir, **16**, 10221-10226, (2000).

APPENDIX

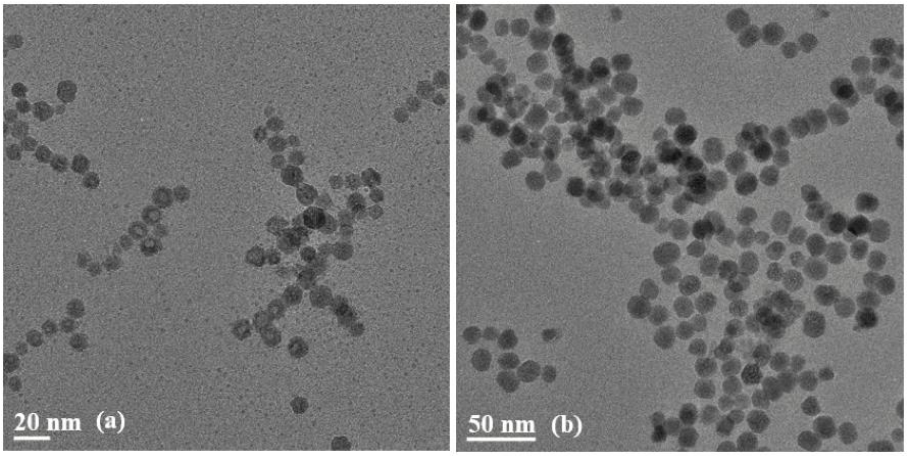

Fig. AI. TEM images of two different UCNPs: a) 12 nm $NaGdF_4$:Yb,Er core and b) 19 nm $NaGdF_4$:Yb,Er@ $NaGdF_4$ core-shell

Table AI. Calculated and Experimental Chemical Shifts of Dianionic SSY Nuclei Closely Involved in Tautomeric Equilibrium Process

atom	azo	hydrazone	experimental
H1	15.4[a]	16.8	14.2–14.7
N2	58.4	−191.5	−178
N3	122.3	−8.9	
C4	156.9	184.3	177.9–178.7[b]

[a]All calculated chemical shifts are given in the δ-scale as the difference between the isotropic part of magnetic shielding tensor (σ_{ISO}) and that of tetramethylsilane 31.6 ppm (^{1}H) and 187.9 ppm (^{13}C), respectively, and nitromethane (CH_3NO_2) for the nitrogen shifts (-144.7 ppm).
[b]Taken from D.J. Edwards et al [141].

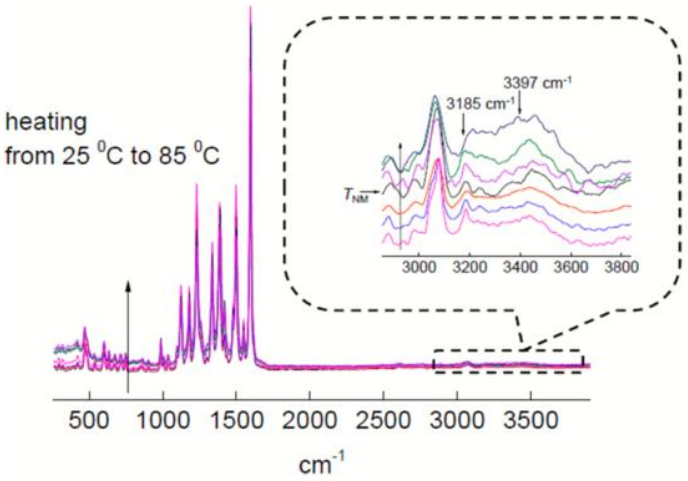

Fig. AII. Temperature evolution of Raman spectra of 1.2 mol/kg SSY aqueous solution by heating from 25 to 85 °C (25, 35, 45, 55, 65, 75, and 85 °C) covering N → N + M phase transition at T ~ 55 °Cin the whole range and around the stretching O-H vibrations of the water molecules (zoom sector)

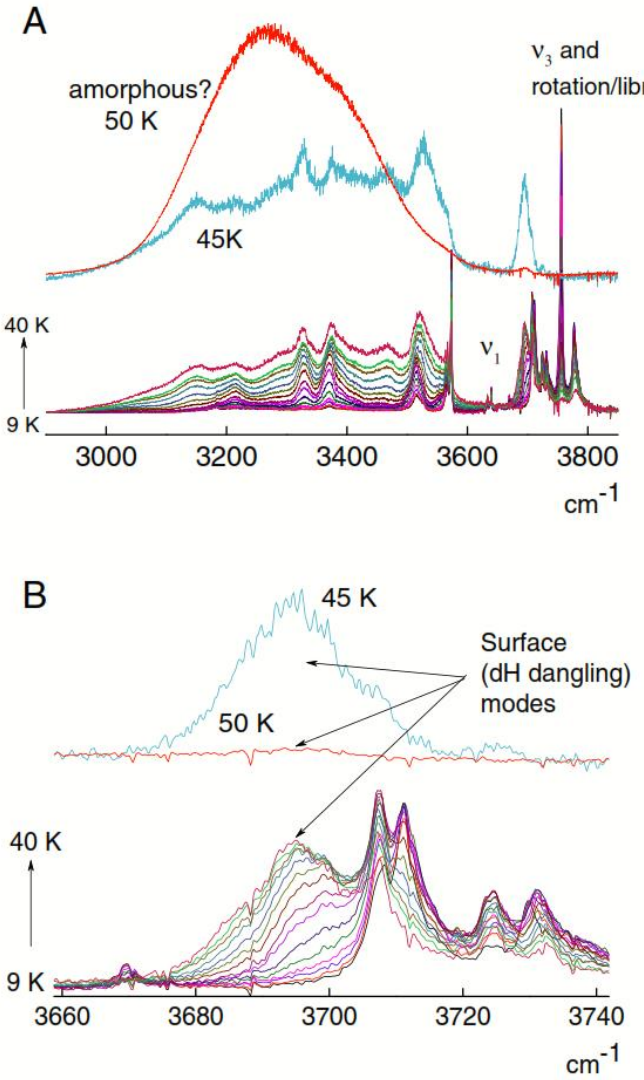

Fig. AIII. Part A: Measured FTIR spectra of water in argon matrix in O–H stretching region over the temperature range 9 - 40 K (from bottom to upper, by stepping ΔT = 2 K). The base line was corrected drawing the line through the end points of this range. The spectrum at 50 K was added to support the assignment of surface (dangling) modes. Part B: the zoomed range 3660–3740 cm^{-1} in order to better display the peculiar thermal evolution of these modes

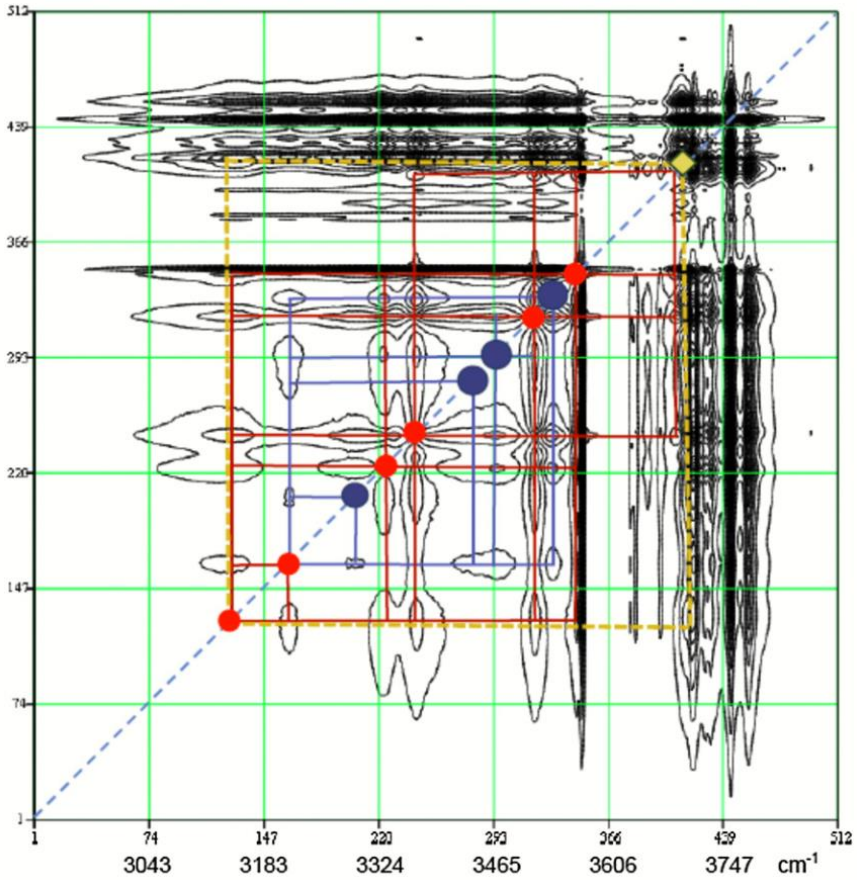

Fig. AIV. 2D asynchronous FTIR correlation spectrum of water in argon matrix in nO–H region. Note, the huge number of points (4096) in each 1D spectrum (Fig. 1) was reduced decimating by factor of 8, and thus the correlation matrix 512 x 512 was processed

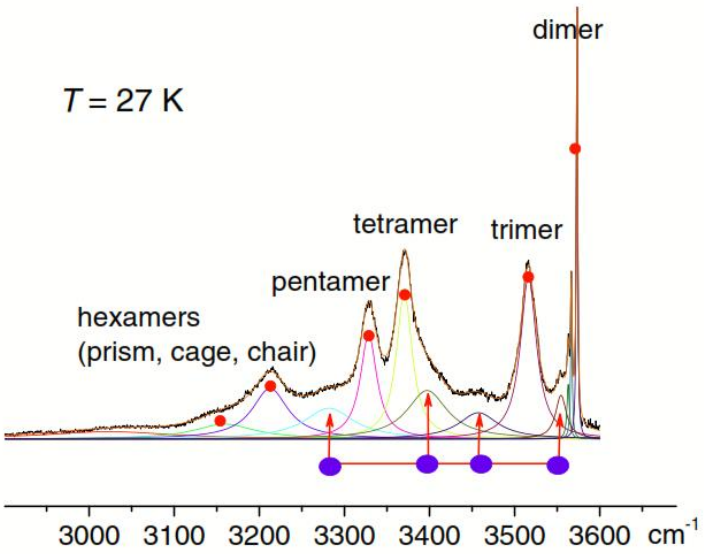

Fig. AV. Non-linear curve fitting of νO–H spectral contour by Lorentz functions (T = 27 K, as example) in the spectral range of 3000 - 3600 cm^{-1}. The maximum positions obtained from the cross-peaks in 2D correlation analysis were used as the zero-order approach for the fitting parameters. The meaning of red and blue bolls is the same as in Fig. AIII.

SANTRAUKA

Įvadas

Branduolių magnetinio rezonanso (BMR) spektrometrija tapo nepakeičiamu įrankiu medicininės diagnostikos bei gydymo srityse, kur ypatingas vaidmuo tenka vaizdinimo metodams. Tarp daugybės radiologinių tyrimų, BMR tomografija (MRT) yra viena pažangiausių ir saugiausių neinvazinių metodikų [1]. Skirtingai nuo konvencinės radiologijos, kompiuterinės tomografijos (KT) ar branduolinės medicinos tyrimų, įskaitant pozitronų emisijos tomografiją (PET), MRT metu nėra naudojama jonizuojančioji spinduliuotė. Kitas nenuginčijamas privalumas yra tai, kad minkštų audinių kontrastas, išgaunamas MRT procedūros metu, dažnu atveju neprilygsta kitoms metodikoms [2]. Be to, MRT pirmauja kontrastinių medžiagų (KM) pasirinkimo gausa [3]. Pažangių KM kūrimas ypatingo dėmesio susilaukė žengiant link galingesnių magnetinių laukų [4,5]. Daugelio pasaulio ligoninėse naudojamų MRT aparatų magnetinio lauko stipris yra nuo 1,5 iki 3 teslų. Mokslinėse laboratorijose 7 T MRT nėra naujovė, tačiau tik 2017 m buvo pristatytas pirmasis 7 T tomografas, skirtas naudojimui klinikoje. Kalbant apie kraštutinumus, jau yra sukurta MRI aparatų, skirtų žmogaus vaizdinimui, kurių magnetinio lauko stipris viršija 10 T [6].

Sparti technologinė pažanga skatina MRT teikiamų diagnostinių galimybių augimą. Spektroskopijos, perfuzijos, difuzijos (įskaitant difuzijos tenzoriaus vaidinimą) bei funkciniai MRT tyrimai sąlygoja dar didesnį MRT jautrumą bei specifiškumą. Šių metodų dėka, ne tik fiksuojami anatominiai pokyčiai, bet ir suteikiama reikšminga papildoma informacija apie naviko charakteristikas, jo progresavimą, bei atsaką į gydymą. Turbūt labiausiai diskutuotina MRT metodika yra magnetinio rezonanso spektroskopija (MRS). Ši metodika remiasi BMR spektroskopijos principais, taikomais *in-vivo* matavimuose. Metabolitų ^{1}H-BMR spektras yra užregistruojamas tiesiogiai iš pasirinktos žmogaus organizmo vietos. Tai suteikia galimybę aptikti cheminius navikinio audinio pokyčius iki atsirandant morfologiniams pakitimams [7]. Nepaisant to, kad MRS klinikinė nauda yra plačiai aprašoma publikacijose, rutininėje praktikoje ši metodika nėra naudojama plačiu mastu, o labiau vertinama mokslo tyrimų centruose. MRS atlikimo technika, bei rezultatų interpretavimas nėra standartizuotas. Kuriami pažangūs technologiniai sprendimai [8], padedantys kovoti su iškylančiais MRS sunkumais, tačiau jų pritaikymas klinikoje yra ribotas. Be to, jiems įgyvendinti

reikalingas kvalifikuotas specialistas. Tinkamai surinkti bei apdoroti MRS duomenys yra perspektyvus įrankis ankstyviems navikinių procesų pokyčiams diagnozuoti.

Ankstyva diagnostika itin svarbi ligos gydymui, todėl daugelių šiuolaikinių mokslinių tyrimų tikslas yra naujų ankstyvos ligų diagnostikos būdų paieška. Nanotechnologijos, kartu su kitomis disciplinomis, tokiomis kaip molekulinė biologija ir vaizdinimo metodai, suteikia unikalias nanomedžiagų pritaikymo galimybes šiuolaikinėje diagnostikoje ir terapijoje. Technologinio proveržio kuriant naujas magnetines nanodaleles dėka, šios atrado įvairiapusį pritaikymą pradedant įprastomis bei multimodalinėmis MRT kontrastinėmis medžiagomis, baigiant šiuolaikiškomis nanodalelių sistemomis, galinčiomis selektyviai transportuoti vaistus į ligos paveiktą audinio vietą [5, 9, 10]. Nemažiau svarbi sparčiai besivystanti platforma yra biojutikliai. Veikdami molekuliniame lygmenyje, jie gali tiksliai identifikuoti labai mažus medžiagų, tokių kaip bakteriniai toksinai ar baltymai, kiekius [11]. Molekuliniams detektoriams gali būti naudojami įvairūs metodai bei medžiagos, pavyzdžiui, MNPs ar liotropiniai chromoniniai skystieji kristalai. Nano-struktūrizuotos medžiagos, tokios kaip hidroksiapatitai (HA), įgauna pagreitį pritaikant šias medžiagas kaulų inžinerijoje, skatinant kaulinio audinio regeneraciją bei ląstelių augimą [12]. Nano-struktūriškumo nustatymas svarbus siejant artimosios tvarkos efektus su makroskopinėmis charakteristikomis, siekiant pagerinti HA mechanines bei biologinio suderinamumo savybes.

Platus nanomedžiagų panaudojimas inovatyvioje medicinoje patvirtina šios technologijos įvairiapusį naudingumą. Kuriamiems naujiems aukštųjų technologijų gaminiams reikia vis aukštesnius reikalavimus atitinkančių šiuolaikinių medžiagų, todėl didelis dėmesys turi būti skiriamas fundamentinių tyrimų plėtrai naujų medžiagų sintezės ir jų charakterizavimo srityje [13]. Atsižvelgus į BMR eksperimentinių metodų įvairovę, BMR spektrometrija atrodo vienas tinkamiausių metodų tiriant nano-struktūrizuotų medžiagų bei BMR pagrindu sukurtų klinikinių metodų pritaikymo medicinoje aktualumą ir ateities perspektyvas.

Pagrindiniai darbo tikslai ir uždaviniai

1. Pritaikyti MRS metodiką Vilniaus Universiteto Santaros Klinikose (VULSK) ir įvertinti alternatyvius šios metodikos pritaikymus prostatos piktybiškumo įvertinimui.
2. Įvertinti MRI kontrastinių medžiagų efektyvumą nagrinėjant skirtingo dydžio gadolinio up-konversinių nanodalelių (UCNPs) įtaką vandens difuzijos ir sukinio-gardelės relaksacijos procesams esant skirtingai magnetinio lauko indukcijai.
3. Tiksliai išanalizuoti temperatūros ir bandinio sudėties įtaką faziniams virsmams, lėtai saviorganizacijai bei tautomerinei pusiausvyrai liotropinių chromoninių skystųjų kristalų (LCLCs) vandeniniuose tirpaluose pritaikant aukštos skyros ^{1}H ir ^{15}N BMR spektrometriją.
4. Ištirti vandens būsenas bei vandens molekulių, izoliuotų nanostruktūrizuotuose kalcio hidroksiapatitų (CaHAs) bandiniuose, klasterių susiformavimą pritaikant kieto kūno BMR spektrometriją. Gautus rezultatus palyginti su FTIR rezultatais analizuojant vandens klasterių susidarymą tirpaluose bei inertinėse matricose.

Ginamieji teiginiai

1. Prostatos metabolitų BMR spektro elgsena priklauso nuo bandinio pH. Šios savybės panaudojimas gali būti perspektyvus papildomas indikatorius prostatos audinio piktybiškumo įvertinimui ankstyvoje diagnostikoje.

2. Skirtingos indukcijos magnetinis laukas nedaro poveikio vandens sukinių-gardelės relaksacijai, įtakotai gadolinio (Gd) up-konversinių nanodalelių (UCNPs). Tai leidžia manyti, kad gadolinio UCNPs gali būti išvystytos į aukštos kokybės dvejopo panaudojimo magnetinio rezonanso tomografijoje (MRT) naudojamas kontrastines medžiagas, efektyviai veikiančias plačiuose magnetinio lauko stiprumo rėžiuose, kas tampa vis aktualiau šiuolaikinėje medicinoje.

3. Tautomerinė pusiausvyra saulėlydžio geltonojo FCF (SSY) bandinyje yra stipriai pasislinkusi link hidrazono tautomero, kurio dominavimas patvirtintas eksperimentiškai pritaikius toliveikę ^{1}H–^{15}N koreliaciją, plačiai žinomą kaip HMBC. Atitinkama pusiausvyros konstanta pK_T = 2.5 nustatyta kvantinės chemijos DFT SMD modeliu.

4. SSY agregatų augimas vyksta kartu su vandens segregacijos procesu tarpkoloninėse ertmėse, dėl ko yra apribojami mainai tarp vandens molekulių ir N-H protonų, esančių vidiniuose kristalinių darinių, išsidėsčiusių kolonomis, sluoksniuose. Šių agregatų gyvavimo trukmė yra $\geq 10^{-8}$ s.

5. Lėtas sistemos grįžimas į pusiausvyrą, fazinei būsenai pereinant iš nematinės į kristalinę, siejamas su lėta molekulių restruktūrizacija, t.y. agregatų augimu suformuojant heksagoninius, kolonomis išsidėsčiusius, sluoksnius. Šie procesai įtakoja lengvai registruojamus ^{1}H BMR spektrinių juostų cheminius poslinkius bei formą.

6. Vandens klasterių struktūra ir dydis priklauso nuo vandens kiekio nanostruktūrizuotuose kalcio hidroksiapatitų bandiniuose (CaHAs). Heksamerai, ar net aukštesnio lygio klasteriai, buvo užregistruoti tik tuose bandiniuose, kuriuose buvo pakankamai adsorbuoto vandens. Adsorbuoto bei paviršinio vandens kiekis gali būti įvertintas pritaikius ^{1}H MAS BMR metodą.

Darbo naujumas ir aktualumas

1. Pagrindinių prostatos metabolitų cheminių poslinkių priklausomybė nuo pH buvo ištirta apjungus aukštos skyros 400 MHz ^{1}H BMR spektrometriją ir 128 MHz MRS metodiką, kuri registruojama magnetinio rezonanso tomografu. Parengtas prostatos MRS fantomas, skirtas užtikrinti procedūros kokybę pritaikant ją Vilniaus Universiteto Ligoninėje Santaros Klinikose.

2. Pasinaudojus supaprastintu Solomon–Bloembergen–Morgan (SBM) modeliu parodyta, kad išmatuoti du skirtingi vandens difuzijos koeficientai gali būti siejami su procesais, vykstančiais šalia UCNPs paviršiaus, ir su procesais, būdingais grynam vandeniui. Darbo metu nustatytas ryšys tarp relaksacijos ir difuzijos leidžia tirti ne tik gadolinio nanodalelės įtaką pilnutinei vandens sukinio-gardelės relaksacijai, bet ir įtaką vietinei, šalia NP paviršiaus esančio vandens molekulių, tiesiogiai sąveikaujančių su paramagnetiniais Gd^{3+} jonais, relaksacijai.

3. ^{1}H BMR spektrinė juosta ties 14.5 ppm, priskiriama tarpmolekuliniam N–H…O ryšiui, buvo aptikta pirmą kartą. Šio signalo buvimas parodo, kad SSY agregatų augimas yra lydimas vandens atskyrimo stulpelių pavidalo tarpkristalinėse ertmėse. Dėl to, vandens molekulės neturi galimybės dalyvauti mainuose su N-H protonais, esančiais vidiniuose stulpelinių darinių sluoksniuose.

4. Atsižvelgus į vandens cheminio poslinkio priklausomybę nuo temperatūros ir Ramano O–H valentinių virpesių juostos formą buvo nustatyta, kad vandens, izoliuoto tarpkristalinėse SSY ertmėse, elgsena sutampa su gryno vandens elgsena. Įvykus faziniam M $\rightarrow$ N virsmui bandinio šildymo metu, vandens molekulių judėjimas primena vandens tirpimo procesą.

5. Jeigu SSY bandinys yra sąlyginai greitai atšaldomas iki temperatūros, žemesnės negu fazinio virsmo N $\rightarrow$ M temperatūra, sistema pereina į peršaldytą būseną ir struktūriniai pokyčiai nestebimi. Tokiu atveju, į pusiausvyros padėtį sistema grįžta lėto saviorganizacijos proceso metu, kurio stebėjimui pirmą kartą panaudota ^{1}H BMR spektrometrija.

Disertacijos sandara

Disertaciją sudaro įvadas, apžvalga, eksperimentinė dalis, rezultatai, išvados ir literatūros sąrašas. Įvade pristatoma disertacijos tema, problematika bei galimybės, iškeliami darbo tikslai ir jų įgyvendinimui suformuluojami uždaviniai. Taip pat įvade pateikiami ginamieji teiginiai, darbo aktualumas ir naujumas. Apžvalgoje trumpai pristatomos tiriamųjų medžiagų grupės ir aptariami su disertacijos tematika susiję BMR metodai. Eksperimentinėje dalyje supažindinama su tirtomis medžiagomis bei taikytų BMR eksperimentinių metodų parametrais. Pasiekti rezultatai aprašomi paskutinėje santraukos dalyje, kurios pabaigoje pateikiamos apibendrintos išvados.

Atsižvelgiant į aptartą BMR pagrindu veikiančių metodų bei medžiagų panaudojimą inovatyvioje medicinoje, darbui pasirinktos keturios grupės tiriamųjų objektų: metabolitai, aptinkami prostatoje; dvigubo panaudojimo gadolinio nanodalelės (UCNPs), kaip potencialios kontrastinės MRT medžiagos; liotropiniai chromoniniai skystieji kristalai (SSY) ir kalcio hidroksiapatitai (CaHA). Pirmos dvi grupės medžiagų gali būti tiesiogiai pritaikytos diagnostikoje naudojant vaizdinimo metodus (MRS, MRT), pagrįstus BMR spektrometrijos principu. Kitos dvi grupės medžiagų buvo pasirinktos kaip inovatyvios medžiagos, aktualios medicinoje, kurių analizei didelę svarbą turi BMR spektrometrijos metodai. Toliau šiame skyriuje bus trumpai pristatyti pagrindiniai disertacijoje naudojami BMR eksperimentiniai metodai.

BMR pritaikymas klinikoje

Klinikoje yra susitarta BMR tomografiją vadinti magnetinio rezonanso tomografija (MRT). Kaip ir BMR spektrometrijoje, MRT veikimas pagrįstas tuo, kad sukinio Larmoro dažnis tiesiogiai proporcingas magnetiniam laukui, kuriame yra tas sukinys. Skirtumas tas, kad BMR spektrometrijos atveju yra reikalingas vienalytis magnetinis laukas, o tomografijos atveju yra naudojami kruopščiai parenkami magnetinio lauko gradientai trimis kryptimis, taip sukuriant nevienalyti tolygiai besikeičiantį erdvėje magnetinį lauką. Tokiu atveju skirtingose erdvės vietose esantys protonai yra veikiami skirtingų magnetinių laukų ir rezonuoja ties skirtingais dažniais. Taigi žinodami magnetinio lauko gradientą, žinome, iš kur ateina BMR signalas. Skirtingose aplinkose esantys sukinių ansambliai, paveikti kintamo magnetinio lauko, į pusiausvyros padėtį grįš ne vienodu greičiu, t.y. išilginės ir skersinės relaksacijos trukmės, atitinkamai T_1 ir T_2, bus skirtingos. Taip gaunamas MRT audinių kontrastas, kuriam pagerinti dažnai naudojamos kontrastinės medžiagos. Labiausiai paplitusios KM yra paramagnetinio gadolinio jono (Gd^{3+}) turintys druskų chelatai. Jų paskirtis yra paspartinti aplinkinių vandens molekulių relaksaciją T_1. Vis daugiau dėmesio susilaukia nanodalelės, kurios galėtų būti taikomos medicinoje, kaip dvejopos KM, pavyzdžiui, naudojamos tiek MRT, tiek optiniame vaizdiniame.

Kitas pažangus BMR pritaikymo klinikoje pavyzdys yra BMR spektrometrija *in vivo*, vadinama magnetinio rezonanso spektroskopija (MRS). MRT atveju, sukinių rezonansinių dažnių skirtumas buvo naudojamas

erdviniam kodavimui, MRS atveju – protonų cheminio poslinkio nustatymui. Prieš atliekant MRS tyrimą, pirmiausia nuskenuojamas MRT anatominis vaizdas ir pasirenkamas norimas vokselis, taip nurodant kurios anatominės srities metabolitų spektras mus domina. Vokselio lokalizacijai yra sukurta daug pažangių impulsų sekų, tačiau pagrindinės naudojamos yra STEAM ir PRESS [14, 15]. Atliekant prostatos MRS, audinio piktybiškumo įvertinimo standartu yra laikomas metabolitų (cholino, kreatino ir citrato) BMR juostų intensyvumų santykis ((Cho + Cr)/Cit) [16].

Kieto kūno BMR spektrometrija

Kietame kūne, molekulių judėjimas yra apribotas, dėl to atsiranda cheminio poslinkio priklausomybė nuo molekulių orientacijos magnetinio lauko atžvilgu. Kristalo atveju, kuriame molekulės yra išlygiuotos viena kryptimi, visų molekulių rezonansinis dažnis bus toks pat ir priklausys nuo kristalo orientacijos. Pasukus kristalą, molekulių cheminis poslinkis pasikeis. Sudėtingesnė situacija stebima, kai kietas kūnas yra miltelių pavidalo ir molekulės yra orientuotos visomis įmanomomis kryptimis magnetinio lauko atžvilgiu, kurių kiekviena atitinka skirtingą rezonansinį dažnį. Tokiu atveju visų BMR signalų superpozicija sąlygos labai išplitusią BMR spektrinę juostą. Anizotropines sukinių sąveikas galima panaikinti arba sumažinti bandinį sukant magiškuoju kampu (54.74°) pastovaus magnetinio lauko krypties atžvilgiu. Tokia technika yra vadinama magiškojo kampo sukimo (MAS) BMR technika. Paprastai MAS sukimo dažnis kinta nuo kelių šimtų hercų iki maždaug 70 kHz [17]. Didžiausias šiuo metu (2019 m.) pasiektas sukimo dažnis yra 126 kHz [18]. Jei bandinys sukamas pakankamai dideliu dažniu, yra įmanoma pasiekti kieto kūno BMR spektro skiriamąją gebą, panašią į užregistruojamą skysčių BMR atveju, tačiau prarandama informacija apie struktūrą ir dinaminius procesus.

2D BMR spektrometrija

Dvimatė BMR spektrometrija yra nepakeičiama priemonė interpretuojant kompleksinių molekulių BMR spektrus [19]. Tinkamai parinkus radijo dažnio impulsų sekas, cheminius poslinkius galima išskleisti vienoje koordinačių ašyje, o sukinių sąveikas – kitoje. 2D BMR spektruose vertikalios ir horizontalios linijos, išvestos per nediagonalius maksimumus parodo, kuriuos branduolius tarpusavyje sieja sukinių sąveika. Priklausomai nuo impulsų sekos (COSY, HMQC, HMBC ir k.t.), galime matyti koreliacijas tarp protonų arba tarp skirtingų branduolių, pavyzdžiui, tarp ^{1}H ir ^{13}C. Taip pat galime

išskirti sąveikas tarp sukinių, nutolusių vienas nuo kito per vieną cheminę jungti, arba per kelias. Šie metodai leidžia tirti labai sudėtingus sukinių sąveikos ir jų dinamikos pasireiškimus [20].

BMR relaksometrija

Relaksacijos procesai skirstomi į sukinio-gardelės relaksaciją (T_1), dar vadinama išilgine relaksacija, ir į sukinio-sukinio relaksacija (T_2), dar žinomą kaip skersinė relaksacija. Relaksaciją gali nulemti šie mechanizmai: dipolinė sąveika, kvadrupolinė sąveika ir chemino poslinkio anizotropija, tačiau dažniausiai dominuoja vienas mechanizmas. Branduoliams, kurių sukinai yra 1/2, paprastai dominuoja dipolinė sąveika. Kai medžiagoje esama stiprių paramagnetinių centrų, neretai yra įvedama sukinių-elektronų sąveika, kurią aprašo trijų sluoksnių *Solomom-Bloembergen-Morgan* (SBM) modelis [21]. Tiriant MRT kontrastines medžiagas, dažniau naudojamas supaprastintas dviejų sluoksnių SBM modelis [22]: pirmąjį koordinacinį sluoksnį sudaro vandens molekulės, kurios tiesiogiai sąveikauja su gadolinio jonu nanodalelėje, antrąjį sluoksnį sudaro tūrinio vandens molekulės, kurios yra labiau nutolusios nuo nanodalelės ir su ja reaguoja mažiausiai.

Šioje disertacijoje, sukinio-gardelės relaksacijos matavimai buvo naudojami siekiant įvertinti nanodalelių, kaip MRT kontrastinės medžiagos, efektyvumą. Iš temperatūrinės relaksacijos spartos ($1/T_1$) priklausomybės, pagal gautos tiesės krypties koeficientą, randamas relaksingumas, kuris yra pagrindinė charakteristika lyginant KM efektyvumą.

BMR difuzija

Neretai molekulinis judėjimas yra siejamas su relaksaciniais sukinių ansamblio procesais. Vienas iš makroskopinių parametrų, nusakančių sukinių judėjimą, yra difuzijos koeficientas, kuris gali būti tiesiogiai išmatuojamas BMR metodu, sukūrus magnetinio lauko gradientą z kryptimi. Tokiu atveju, vykstant difuzijai ir sukiniams migravus iš vieno erdvės taško į kitą, jų precesijos dažnis pasikeis. Kuo didesnis difuzijos koeficientas, tuo stipresnis koherentiškumo praradimas, o tai savo ruožtu paspartina BMR signalo gesimą. Difuzijos koeficiento nustatymui, dažniausiai taikoma sužadintojo sukinių aido BMR impulsų seka, kurioje naudojami impulsiniai magnetinio lauko gradientai. Keičiant magnetinio lauko gradientų dydį, jų trukmę, arba vėlinimą tarp šių impulsų, matuojama BMR signalo intensyvumo priklausomybė, iš kurios, žinant kitas eksperimento metu nustatytas konstantas, apskaičiuojamas difuzijos koeficientas.

Metodika

Tirtosios medžiagos

Disertacijai pasirinktos keturios grupės tiriamųjų objektų:

- Pagrindinių metabolitų, aptinkamų prostatoje, vandeniniai tirpalai: citratas (Cit, 50 mM), kreatinas (Cr, 5 mM), cholinas (Cho, 1 mM), sperminas (Spm, 6 mM). Aukštos skyros BMR matavimams naudojamos 5 mm Bruker ampulės. MRS matavimamas parengtas fantomas, sudarytas iš keturių 50 ml bandinių indelių pamerktų į 3 l vandens indą.
- Skirtingų dydžių retaisiais žemės metalais (Yb^{3+}, Er^{3+}) legiruotos $NaGdF_4$ up-konversinės nanodalelės (UCNPs), modifikuotos polimeru TWEEN80, ir, kai kurios iš jų, papildomai dengtos $NaGdF_4$ apvalkalu. Palyginimui ištirta klinikinė kontrastinė medžiaga Gadovist@ ($C_{18}H_{31}GdN_4O_9$).
- Skirtingų koncentracijų 90% grynumo Saulėlydžio geltonojo FCF (SSY) vandeniniai tirpalai. Koncentracijos pasirinktos atsižvelgiant į fazinę diagramą, siekiant aptikti fazinius virsmus 25-95 ^{0}C temperatūrų intervale.
- Kompleksiniai nano-struktūrizuoti kalcio hidroksiapatitai (CaHA), susintetinti naudojant vandeninę zolių-gelių metodiką, panaudojus skirtingus kompleksadarius: etilenglikolį (EG) ir vyno rūgštį (TA), taip pat komercinis nano-struktūrizuotas CaHA.

BMR eksperimentiniai metodai

BMR spektrometrija *in-vivo* buvo atlikta naudojant 3 T klinikinį tomografą (128 MHz Larmoro dažnis protonams). Kiti matavimai atlikti aukštos skyros BMR spektrometru, kurio rezonancinis dažnis yra 400 MHz protonams ir 40 MHz ^{15}N branduoliams (9.4 T), taip pat 0.4 T BMR spektrometru. ^{1}H–^{15}N koreliacinis spektras buvo išmatuotas naudojant HMBC impulsų seką. Relaksometrijos eksperimentai atlikti pasitelkus apgrąžos atstatymo impulsų seką (180^0-τ-90^0) parinkus 16 skirtingų vėlinimo trukmių (τ). Difuzijos koeficiento nustatymui taikoma sužadintojo sukinių aido BMR impulsų seka, keičiant magnetinio lauko gradientų dydį nuo 2% iki 95% per 64 žingsnius. Kieto kūno eksperimentams naudota MAS BMR technika sukant bandinį 10 kHz dažniu. DSS ir CH_3NO_2 medžiagos buvo pasirinktos, kaip Larmoro dažnio etalonai ^{1}H-BMR ir ^{15}N-BMR spektrams atitinkamai.

Metabolitų BMR tyrimų rezultatai

Šiame skyriuje nagrinėjami prostatos metabolitų bandiniai ir pateikiami pagrindiniai BMR tyrimų rezultatai. Skyrių sudaro du poskyriai. Kaip aptarta literatūros apžvalgoje, atliekant prostatos MRS, audinio piktybiškumo įvertinimo standartu yra laikomas pagrindinių metabolitų BMR juostų intensyvumų santykis ((Cho + Cr)/Cit). Deja, neretai pasitaiko situacijų, kai dėl išplitusių BMR juostų, mažos metabolitų koncentracijos ar nepakankamo signalo-triukšmo santykio, yra sudėtinga išskirti tam tikrų metabolitų spektrines juostas ir negalime paskaičiuoti intensyvumų santykio. Siekiant pagerinti MRS procedūros, atliekamos VULSK, kokybę, metabolitų bandiniai pirmiausia buvo išanalizuoti aukštos skyros BMR spektrometru. Gauti rezultatai pritaikyti MRS procedūros parametrų optimizavimui ir fantomo kūrimui.

Aukštos skyros BMR spektrometrija

Metabolitų analizė pradėta nuo BMR juostų identifikavimo. Kiekvieno tiriamojo metabolito vandeninio tirpalo ^{1}H-BMR spektras užregistruotas atskirai ir palygintas su visų metabolitų skirtingo pH (6 ir 7) tirpalų BMR spektrais (1 pav.).

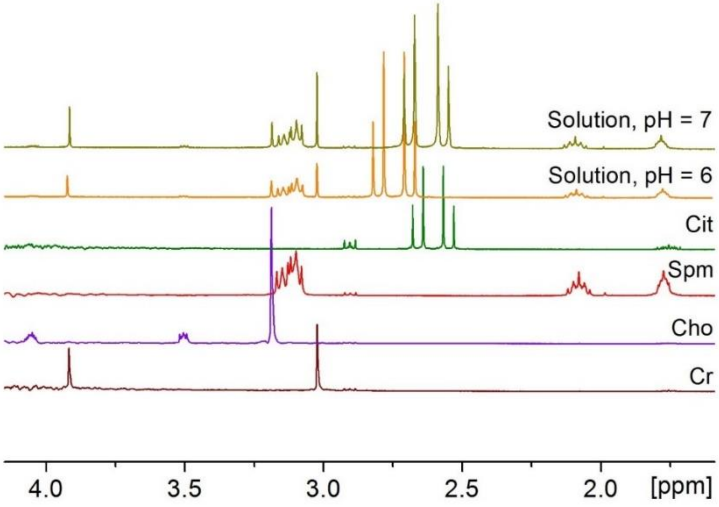

1 pav. *Išplėsti metabolitų 400 MHz ^{1}H-BMR spektrai. Viršutiniai du spektrai atitinka metabolitų deuteruoto vandens tirpalus (*pH = 6 *ir* pH = 7*), likusieji – vandeninius tirpalus kiekvieno metabolito atskirai: citrato (Cit), spermino (Spm), cholino (Cho) ir kreatino (Cr)*

Esant skirtingiems pH, pastebėtas skirtingas citrato cheminis poslinkis. Kitiems metabolitams tirpalo rūgštingumas įtakos neturėjo. Detalesnė citrato cheminio poslinkio priklausomybė nuo pH pavaizduota 2 paveiksle. Keičiant tirpalo pH nuo 4.9 iki 7.1, citrato BMR juostų centro cheminis poslinkis pakito nuo 2.67 iki 2.55, o atstumas tarp dubletų padidėjo nuo 0.06 iki 0.10. Temperatūros įtaka metabolitų BMR spektrams nepastebėta.

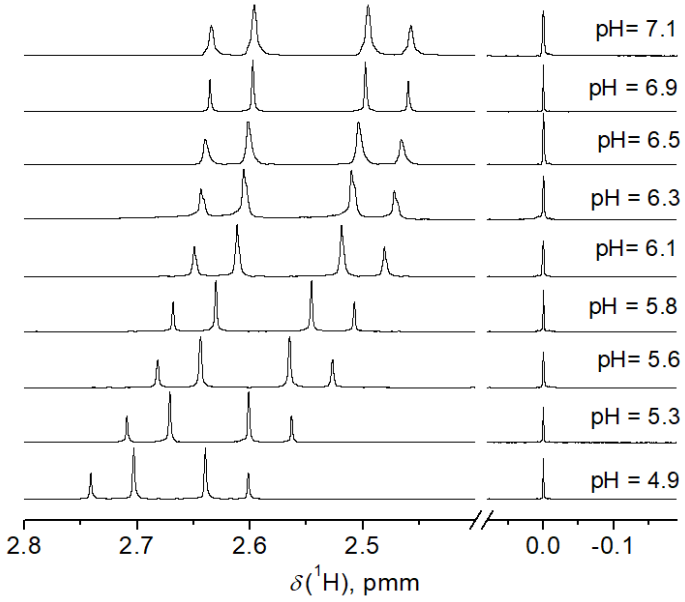

2 pav. *Išplėsti citrato vandeninių tirpalų 400 MHz ^{1}H-BMR spektrai esant skirtingiems tirpalų pH*

MRS matavimai

Tolimesnis žingsnis buvo patikrinti, ar BMR spektrų, užregistruotų *in-vivo,* spektrinė skyra taip pat yra pakankama citrato cheminio poslinkio priklausomybei nuo pH aptikti. Prieš atliekant matavimus, pirmiausia buvo išanalizuoti bandinio paruošimo būdai bei skenavimo parametrai. Atlikta visa eilė matavimų esant skirtingo tūrio bandiniais. Ištirta vokselio dydžio bei jo padėties bandinio atžvilgiu įtaka BMR spektrui (3 pav.). Nustatyta, kad vokselio dydis labai priklauso nuo bandinio dydžio. Jei bandinys yra bent 3 kartus didesnis už pasirinkto vokselio dydį, BMR juosta gali būti išskirta net esant 5x5x5 mm^3 dydžio vokseliui. Taip pat pastebėta, kad kuo pasirinktas vokselis yra arčiau bandinio krašto, tuo prastesnės kokybės spektras, t.y.

mažesnis signalo-triukšmo santykis, intensyvesnis nesupresuoto vandens BMR signalas. Taigi, per didelis vokselis bus taip pat negerai, kaip ir per mažas, nes vokselis bus per arti bandinio krašto. Tai ypač jaučiasi, jei bandinys yra apsuptas oro.

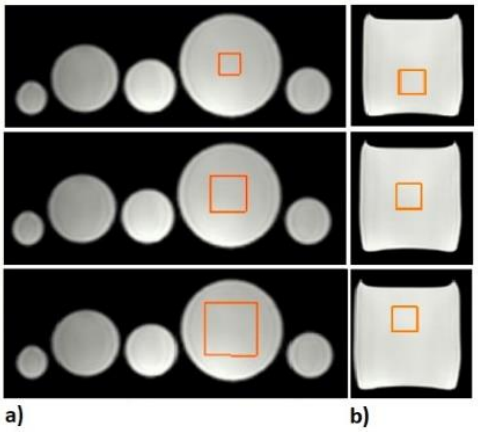

***3 pav**. MRS matavimų pavyzdys tiriant vokselio dydžio (a) ar vokselio padėties bandinio atžvilgiu (b) įtaką 128 MHz BMR spektrui*

MRS impulsų sekų parametrai, tokie kaip laiko intervalai tarp impulsų (TR, TE), skenavimų skaičius (NSA), taip pat vandens ar riebalų signalo slopinimo, šimavimo technikos, buvo analizuojami panardinus bandinį į vandens pripiltą indą. Pastebėta, kad optimalūs parametrai atitinka parinktus gamintojo (SV-PRESS impulsų sekai: TR = 1500 ms, TE = 144 ms, NSA = 112).

Atsižvelgiant į atliktų matavimų rezultatus, buvo parengtas prostatos MRS fantomas. Keturi 50 ml indeliai su metabolitų tirpalais panardinti į 3 l vandens indą. Tolimesniems matavimams naudotas 12x12x12 mm^3 dydžio vokselis. BMR spektras, užregistruoti klinikiniu 3 T tomografu, buvo palyginti su tų pačių metabolitų tirpalų spektru, užregistruotu aukštos skyros 400 MHz BMR spektrometru (4 pav.). Nors metabolitų koncentracijos abiem atvejais buvo vienodos, spermino BMR juosta buvo išskiriama tik aukštos skyros BMR spektrometru.

Svarbu paminėti, kad žmogaus organizme nėra DSS, todėl matuojant pH priklausomybes MRS procedūros metu yra reikalingas kitas atskaitos taškas – metabolitas, kurio cheminis poslinkis nepriklausytų nuo pH. Tam buvo pasirinktas cholinas, nes prostatos MRS atveju jo BMR juostos intensyvumas yra didesnis nei kreatino ar spermino.

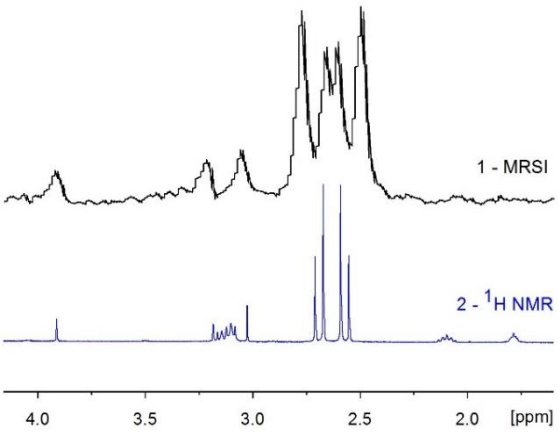

***4 pav**. Prostatos metabolitų vandeninių tirpalų ^{1}H-BMR spektrų palyginimas juos registruojant klinikiniu 128 MHz tomografu (1) ir 400 MHz BMR spektrometru (2)*

Keičiant tirpalo pH, pastebėta tokia pati 128 MHz ^{1}H-BMR spektro elgsena, kaip ir 400 MHz ^{1}H-BMR atveju. Mažėjant pH, citrato cheminis poslinkis pasistumia į kairę, t.y. $\Delta\delta(^1\text{H})_{\text{Cit-DSS}}$ padidėja, kai tuo tarpu $\Delta\delta(^1\text{H})_{\text{Cit-Cho}}$ sumažėja (5 pav.). Kadangi yra žinoma, jog navikinio audinio pH yra mažesnis nei sveiko audinio [23], informacija apie cheminius poslinkius gali būti naudinga identifikuojant ankstyvuosius navikinių procesų pokyčius.

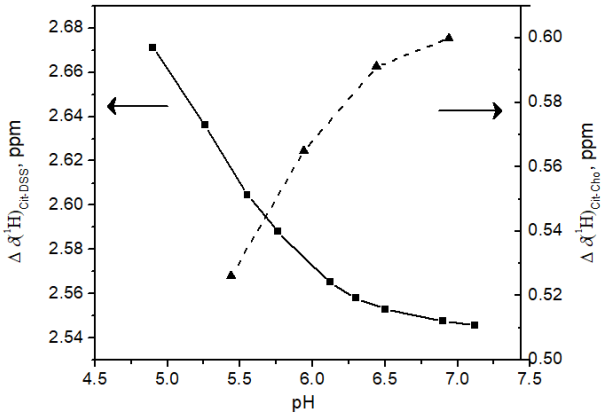

***5 pav**. Citrato cheminio poslinkio priklausomybė nuo pH. 400 MHz ^{1}H BMR spektrometrijos atveju, cheminiai poslinkiai buvo matuojami tarp citrato dubletų vidurio taško ir DSS (kairėje). 128 MHz ^{1}H MRS atveju – tarp citrato dubletų vidurio taško ir cholino (dešinėje)*

- ^{1}H-MRS metodika gali ženkliai pasitarnauti onkologijos srityje, kaip neinvazinė procedūra, suteikianti informacijos apie navikinių procesų metabolizmą. Vis dėl to, tai gilių žinių ir laiko reikalaujantis tyrimas, kas apriboja šios procedūros pritaikymą klinikoje. Ateityje spektrų analizės supaprastinimas, bei naujų standartizuotų metodų įgyvendinimas būtų siekiamybė.

- Metabolitų ^{1}H-BMR spektrų analizė aukštos skyros BMR spektrometru yra greitas ir tikslus metodas, suteikiantis vertingos informacijos pritaikant MRS metodiką klinikoje. Tai gali būti panaudojama ruošiant MRS fantomą, kuris reikalingas MRS procedūros kokybės užtikrinimui.

- Prostatos pH įvertinimas analizuojant metabolitų cheminius poslinkius MRS metodu, gali būti perspektyvus papildomas piktybiškumo rodiklis, ypač žengiant link galingesnių klinikoje naudojamų magnetinių laukų, o tuo pačiu ir link geresnės spektrinės skiriamosios gebos.

- Šiame darbe gauti rezultatai padėjo pritaikyti MRS metodiką Vilniaus Universiteto Ligoninėje Santaros klinikose, tačiau rutininiam MRS naudojimui reikalinga gilesnė spektrų apdorojimo analizė bei inovatyvių MRS procedūros spektrų užregistravimo metodų įdiegimas.

- Visumoje, metabolomika yra svarbi ir įdomi mokslinių tyrimų šaka, turint omenyje, kad tam tikrų metabolitų būvimas gali atskleisti metabolinių procesų seką ir padėti atitinkamai parinkti tolimesnę paciento priežiūrą.

Gadolinio nanodalelių BMR tyrimų rezultatai

Nanodalelė, kuri yra papildomai padengta išoriniu sluoksniu, pasižymi ypač geromis optinėmis savybėmis (našesnė up-konversija). Norint įvertinti, kaip tai įtakoja vandens sukinio-gardelės relaksaciją, įvedama sąvoka relaksingumas (r_1). Relaksingumas yra pagrindinis parametras lyginant MRT kontrastinių medžiagų (KM) efektyvumą, kuris aprašomas:

$$\frac{1}{T_1} = \frac{1}{T_{10}} + r_1 C; \quad (1)$$

čia T_{10} yra vandens išilginė relaksacijos trukmė, kai bandinyje nėra kontrastinės medžiagos, o C yra KM koncentracija (mM). KM efektyvumo analizė esant skirtingo dydžio nanodariniams atlikta pasirinkus bandinius, kurių BMR eksperimento atkartojamumas buvo geriausias: 12 nm $NaGdF_4$:Yb^{3+},Er^{3+} nanodalelės modifikuotas TWEEN80 polimeru ir tokios pačios NP papildomai dengtos $NaGdF_4$ apvalkalu (19 nm).

BMR relaksometrija

Pirmiausia išmatuota gryno vandens, naudojamo NPs bandinių skiedimui, išilginė relaksacija (T_{10}), kurios vertė (3.9 s esant 37 ºC) sutapo su literatūros duomenimis [24]. NPs bandinių BMR relaksometrijos rezultatai parodė, kad KM relaksingumas padidėjo nuo 0.684 $mM^{-1}s^{-1}$ iki 0.989 $mM^{-1}s^{-1}$ lyginant atitinkamai 19 nm ir 12 nm nanodaleles. Šie dydžiai apskaičiuoti pagal gadolino jonų koncentraciją tirpale, laikant, jog gadolinio masės dalis nanodalelėje yra 61 %. Literatūros duomenimis [25, 26], kalbant apie T_1 kontrastines medžiagas, mažesnio dydžio NPs paprastai sąlygoja geresnį kontrasto stiprinimą. Publikacijose pateikiama NPs dydžių ir jų relaksingumo koreliacija parodė, kad paviršiaus-tūrio santykis mažėjant nanodalelės matmenims tampa dominuojančiu faktoriumi, įtakojančiu relaksingumą. Nepaisant to, Gao ir bendraautoriai pademonstravo, kad didesnis relaksingumas buvo pasiektas esant didesnėms NPs. Tai buvo paaiškinta teigiant, kad esant didesnei nanodalelei (>15 nm), rotacinė koreliacinė trukmė (τ_R) tampa dominuojančiu veiksniu, įtakojančiu relaksingumą [27]. Atsižvelgiant į šioje disertacijoje gautus rezultatus, galima teigti, kad, nors NPs dydis siekė 19 nm, dominuojančiu veiksniu išliko paviršiaus-tūrio santykis.

Aptartose publikacijose magnetinio lauko stipris neviršijo 3 teslų, kas yra plačiausiai naudojamas MRT magnetinio laukas klinikinėje praktikoje. Kadangi šiame darbe BMR matavimai buvo atlikti 400 MHz spektrometru,

kas atitinka 9.4 T, tolimesnis žingsnis buvo įvertinti magnetinio lauko indukcijos įtaką. Papildomi relaksometrijos matavimai buvo atlikti su 16 MHz spektrometru. Yra žinoma, kad kuo stipresnis magnetinis laukas, tuo prastesnis Gd kontrastinių medžiagų efektyvumas – mažesnis relaksingumas [28], tačiau lyginant 16 MHz ir 400 MHz BMR matavimų rezultatus, reikšmingas skirtumas nepastebėtas: apskaičiuotos r_1 vertės skirtingiems NPs bandiniams buvo atitinkamai 0.689 $mM^{-1}s^{-1}$, 0.986 $mM^{-1}s^{-1}$ ir 0.684 $mM^{-1}s^{-1}$, 0.989 $mM^{-1}s^{-1}$ (6 pav.). Tai leidžia manyti, jog magnetinio lauko indukcija $NaGdF_4$ nanodalelių efektyvumui įtakos neturi ir galima tikėtis panašių rezultatų dirbant su klinikiniu 3T BMR tomografu.

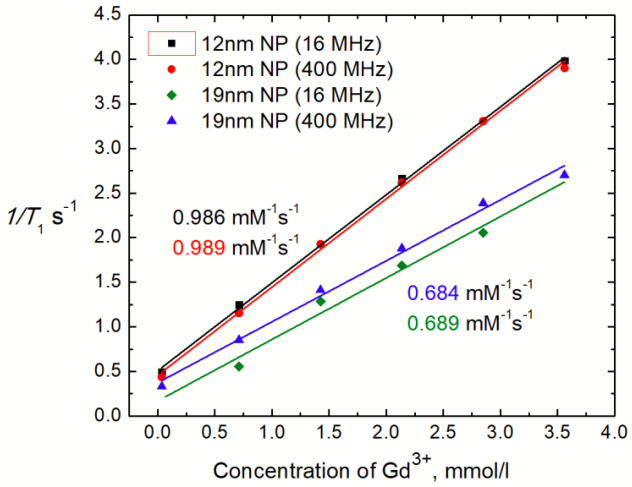

***6 pav**. Skirtingo dydžio β-$NaGdF_4$ nanodalelių (12 nm be apvalkalo ir 19 nm su apvalkalu) vandeninių tirpalų sukinio-gardelės relaksacijos spartos priklausomybė nuo Gd^{3+} jonų koncentracijos esant skirtingiems magnetiniams laukams. (T = 37 ºC)*

Palyginimui ištirta ir klinikinė Gd kontrastinė medžiaga Gadovist. Reikėtų atkreipti dėmesį, kad UCNPs koncentracija buvo pateikta g/l, o Gadovist atveju – mmol/l (nuo 0.01 µmol/l iki 14 mmol/l). Lyginant su komerciniu Gadovist (r_1 = 3.2 $mM^{-1}s^{-1}$), gadolinio nanodarinių relaksingumas yra sąlyginai prastas, nes viduje esantis gadolinis sunkiau kontaktuoja su vandeniu. Tuo tarpu kontrastinių medžiagų rinkoje plačiai naudojamos aktyviosios druskos gali tiesiogiai reaguoti su vandens molekulėmis. Nepaisant šių priežasčių, gadolinio nanodariniai pasižymi svarbiomis optinėmis savybėmis, kurios didina jų perspektyvumą dėl dvigubo panaudojimo galimybių.

Siekiant geriau suprasti vandens sukinio-gardelės relaksacijos mechanizmus, taip pat išanalizuoti difuzijos procesai vandeniniuose 19 nm $NaGdF_4$ nanodalelių tirpaluose. BMR metodu tiesiogiai išmatuoti du difuzijos koeficientai (D_1 ir D_2) (7 pav.), turintys skirtingą įnašą į bendrą BMR signalo intensyvumą (apie 96% ir 4% atitinkamai).

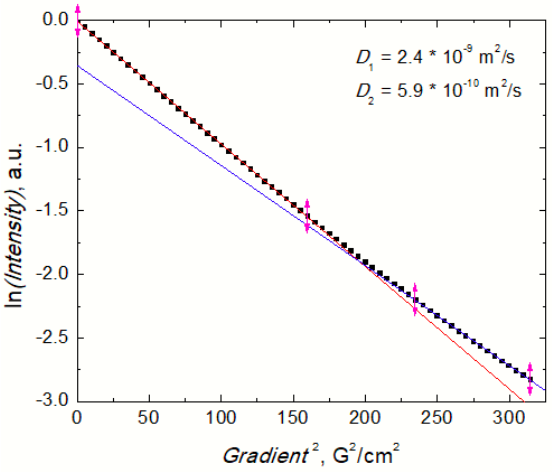

7 pav. *^{1}H-BMR juostos intensyvumo priklausomybė nuo gradiento kvadrato sužadintojo sukinių aido eksperimento metu gadolinio 19 nm nanodalelių vandeniniuose tirpaluose*

Tolimesnei analizei paruošti dviejų skirtingų koncentracijų (1 g/l ir 0.75 g/l) 19 nm UCNPs tirpalai. Pastebėta, kad tik vieno difuzijos koeficiento temperatūrinė priklausomybė buvo jautri bandinio koncentracijai (8 pav.). Be to, gryno vandens aktyvacijos energija (20.442 kJ/mol), paskaičiuota naudojant išilginės relaksacijos spartos ($1/T_1$) temperatūrinę priklausomybę, yra palyginama su vandens, esančio NPs bandiniuose, aktyvacijos energija (21.362 kJ/mol), kuri buvo paskaičiuota naudojant difuzijos koeficiento D_1 temperatūrinę priklausomybę.

Remiantis gautais rezultatais, padaryta prielaida, kad NPs, kaip kontrastinių medžiagų, veikimas atitinka supaprastintą SBM modelį. Tai reiškia, kad relaksacijos mechanizmą nulemia tik du atskiri procesai. Vienas jų atitinka tūrinį vandenį, kurio difuzijos koeficientas yra D_1, toliau naudojamas kaip D_B (*angl*. bulk). Kitas procesas atitinka lokalų vandenį (tiesiogiai su gadolinio nanodalelėmis kontaktuojančių vandens molekulių),

kurio difuzijos koeficientas yra D_2, toliau naudojamas kaip D_L. Tuomet NPs vandeninių tirpalų relaksacijos sparta (R_1) gali būti aprašoma tokia išraiška:

$$R_1 = R_{1B} \cdot I_B + R_{1L} \cdot I_L. \quad (2)$$

NPs bandinių tūrinio ir lokalaus vandens difuzijos koeficientų (D_B ir D_L) įnašas į bendrą BMR signalo intensyvumą (I_B ir I_L) yra pateikiamas Topspin programiniame pakete. Tūrinio vandens relaksacijos spartą (R_{1B}) pakeitus į gryno vandens relaksacijos spartą, galime nesunkiai įvertinti lokalaus vandens relaksacijos spartą (R_{1L}), ko negalime padaryti kitais metodais.

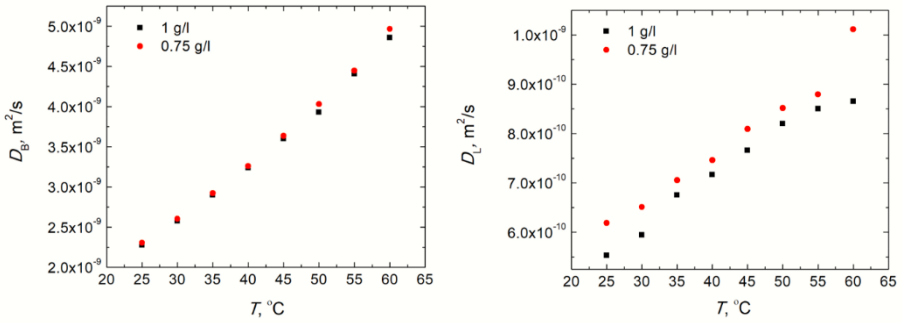

8 pav. *BMR metodu išmatuotų 19 nm NP bandinių difuzijos koeficientų priklausomybės nuo temperatūros: kairėje – tūrinio vandens (D_B), dešinėje – lokalaus vandens (D_L)*

Difuzijos koeficientų ryšys su relaksacijos procesais atveria galimybes tyrinėti vandens molekules, esančias arti gadolinio nanodalelių paviršiaus. Tai suteikia gilesnį supratimą apie esminius veiksnius, įtakojančius kontrastinių medžiagų relaksingumą, kas itin svarbu ieškant efektyviausių dvigubo panaudojimo KM variantų.

Gadolinio nanodalelių BMR analizės išvados

- Kuriant aukšto relaksingumo MRT išilginės relaksacijos kontrastines medžiagas, pagrinde remiamasi sąveikos sustiprinimu tarp nanodalelės ir gretimų vandens protonų. Šiame darbe parodyta, kad vandens difuzijos procesai, išmatuoti BMR metodu, gali būti siejami su MRT kontrastinių medžiagų veikimo paaiškinimui taikomu SBM modeliu. Tokiu būdu, galima įvertinti ne tik NPs įtaką bendrai vandens išilginei relaksacijai, bet ir NPs įtaką lokalaus vandens protonų, tiesiogiai sąveikaujančių su paramagnetiniais Gd^{3+} jonais, sukinio-gardelės relaksacijai.

- Detalus šių relaksacijos procesų supratimas nukreiptų tinkama linkme ieškant optimalios NPs struktūros sukinio-gardelės relaksacijos spartinimo požiūriu. Kuriant naujos kartos MRT kontrastines medžiagas, didelis dėmesys taip pat skiriamas sparčiai besivystančioms nanotechnologijoms, inovatyvioms MRT technikoms, bei naujiems klinikiniams pritaikymams. Dėl šios priežasties, dvigubo panaudojimo up-konversinės nanodalelės (UCNPs), išlaikančios aukštą relaksingumą plačiame magnetinio lauko stiprumo intervale bei pasižyminčios efektyviomis up-konversijos savybėmis, būtų itin vertingos.

- Šiame darbe parodyta, kad magnetinio lauko indukcija nanodalelių relaksingumui įtakos neturėjo. Taip pat pademonstruota, jog 12 nm gadolinio UCNPs pasižymėjo didesniu relaksingumu lyginant su 19 nm UCNPs. Tai reiškia, kad MRT kontrastinių medžiagų požiūriu mažesnio diametro NPs yra pranašesnės.

- Remiantis gautais rezultatais, galima teigti, jog gadolinio UCNPs yra perspektyvios kuriant inovatyvias dvigubo panaudojimo MRT kontrastines medžiagas.

Skystųjų kristalų (SSY) vandeninių tirpalų koncentracijos (nuo 0.7 iki 1.4 mol/kg) pasirinktos atsižvelgiant į fazinių virsmų diagramą, kurią sudaro trys mezofazės: izotropinė (I), nematinė (N) ir kristalinė (M) [29]. Nematinė (N) fazė pasižymi stulpeliniu molekulių išsidėstymu, išlaikant orientaciją, kuriai būdinga tolimoji tvarka, tačiau neturint pastovios padėties. Šioj fazėje pastebimas netvarkingas kolonų sukimasis apie jų ašis bei molekulių sukimasis kolonų viduje. Kristalinėje (M) fazėje molekulės išsidėsčiusios lygiagrečiomis kolonomis sudarant heksagoninę struktūrą. Šiai fazei būdingos sritys, kurios pasižymi tolimąja tvarka tiek krypties, tiek padėties atžvilgiu.

BMR spektrometrija yra jautrus metodas tyrinėjant skystųjų kristalų fazinius virsmus [30]. Keičiant temperatūrą nuo 25 iki 90 ºC, buvo išanalizuoti visi fazinių virsmų procesai I ↔ N ↔ M. ^{1}H-BMR spektrai parodė, kad sumaišius tirpalą izotropinėje (I) fazėje, priklausomai nuo jo koncentracijos, laiko intervalo ir temperatūrinės praeities, bus stebima skirtingo pobūdžio fazinių būsenų elgsena bei lėta saviorganizacija (*angl*. self-assembling) po bandinio peršaldimo (9 pav.).

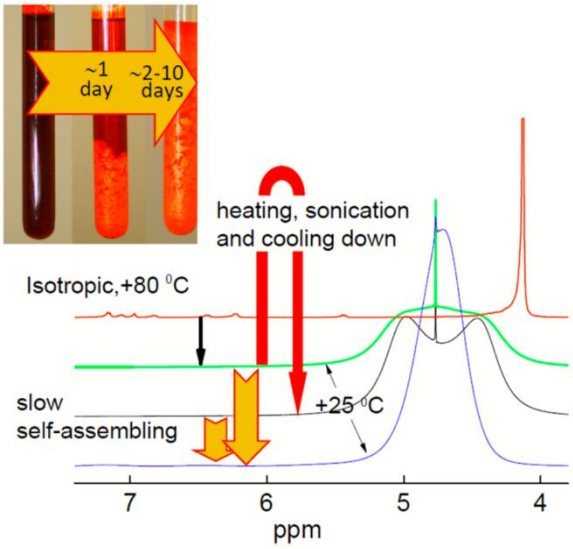

9 pav. *Temperatūrinė SSY (1.2 mol/kg) vandeninių tirpalų ^{1}H BMR spektrų evoliucija pereinant fazinius virsmus ir vykstant lėtai saviorganizacijai peršaldžius bandinį priklausomai nuo bandinio sumaišymo ir jo temperatūrinės praeities*

Literatūros duomenimis, atsižvelgiant į protonų giminiškumą, N−H···O forma yra laikoma stabilesne už O−H···N [32]. Darbo metu atlikti DFT skaičiavimų rezultatai taip pat parodė, kad SSY tautomerinė pusiausvyra yra stipriai pasislinkusi link hidrazono formos (pusiausvyros konstanta pK_T = 2.5). BMR metodu buvo išmatuotos ^{1}H-^{15}N sukinių, nutolusių vienas nuo kito per kelias chemines jungtis, sąveikos (HMBC eksperimentas). 2D spektre (10 pav.) aiškiai matomas cheminis poslinkis $\delta(^{15}N)$ = −178 ppm palyginamas su DFT metodu paskaičiuota verte (-191.5) azoto atomui, esančiam N−H···O tiltelyje SSY hidrazono tautomere. Tuo tarpu azoto, esančio azo tautomere, cheminis poslinkis pagal DFT skaičiavimus turėtų būti +58.4 ppm. Tai patvirtina, kad dominuojanti SSY forma yra hidrazonas (SSY koncentracija 0.7 M, temperatūra 293 K).

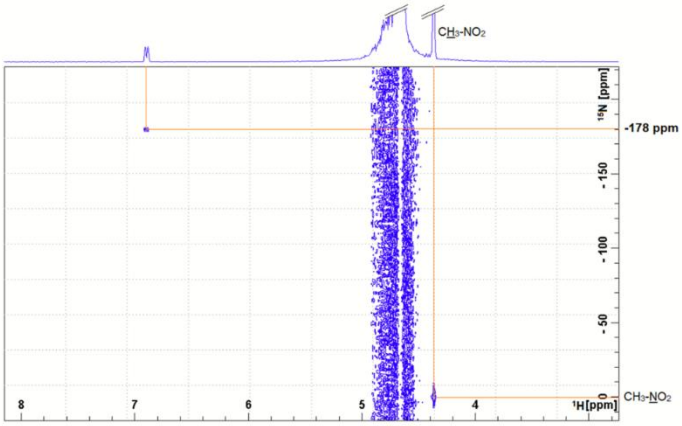

10 pav. *0.7 mol/kg SSY vandeninio tirpalo ^{1}H-^{15}N BMR koreliacijos spektras (HMBC) esant 25 °C temperatūrai*

Protono (H1), esančio N−H···O tiltelyje, cheminis poslinkis gali būti kita potenciali BMR spektrinė ypatybė, suteikianti tiesioginės informacijos apie tautomerų dinamiką ir vandenilinio ryšio stiprumą SSY tirpaluose. Šių protonų cheminių poslinkių vertės, apskaičiuotos DFT metodu, buvo 15.4 ir 16.8 ppm atitinkamai azo ir hidrazono tautomerams. SSY vandeninių tirpalų atveju, matuojant H1 cheminius poslinkius eksperimentiškai, paprastai yra tikimasi, kad vyks spartūs mainai tarp protonų, dalyvaujančių vandeniliniame ryšyje, ir vandens, kuris šiuo atveju naudojamas kaip tirpiklis. Dėl to, H1 BMR juosta būtų labai išplitusi ir neaptinkama. Vis dėlto, chromoniniai skystieji kristalai pasižymi viena išskirtine savybe – stipria saviorganizacija.

Chromoniniuose liotropiniuose skystuosiuose kristaluose, skirtingai nuo daugelio liotropinių kristalų, nėra kritinės micelių koncentracijos, taigi saviorganizacija gali vyki esant labai žemoms bandinio koncentracijoms. Saviorganizacija sąlygoja lazdelių formos agregatų, kurie gali būti ir sudėtingesnės geometrijos su sanglaudos kristalų defektais, susidarymą [32, 33]. Susidariusios struktūros yra sutvirtinamos $\pi-\pi$ ryšiu tarp aromatinių žiedų [34]. Tokiu būdu, galima tikėtis, kad mainai tarp vandens molekulių ir H1 protonų vyks tik agregato paviršiuje. Laikant, kad N−H···O tilteliai yra izoliuoti agregatų vidiniuose sluoksniuose, kurių gyvavimo trukmė yra $\geq 10^{-7}-10^{-8}$ s, kas atitinka BMR laiko skalę, atitinkama H1 spektrinė juosta turėtų būti matome spektre. Šiame darbe pademonstruota, kad H1 BMR signalas 14.2 – 14.7 ppm intervale buvo matomas visuose SSY BMR eksperimentuose, išskyrus esant trims žemiausioms temperatūroms (25, 30 ir 35 ºC) bandinio šaldymo ciklo metu (11a pav.). Sistemai lėtai grįžus į pusiausvyros padėtį, H1 spektrinė juosta buvo pastebima net ir minėtose temperatūrose (11b pav.).

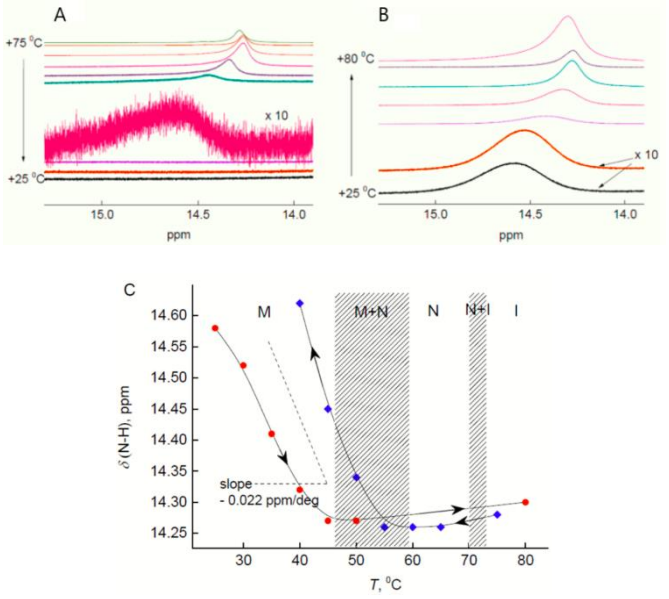

11 pav. *^{1}H NMR signalo formos kitimas šaldymo (A) ir šildymo (B) ciklų metu bei N−H···O protono cheminio poslinkio priklausomybė nuo temperatūros 1.2 mol/kg koncentracijos SSY vandeniniame tirpale (C)*

Eksperimentiškai išmatuoti H1 cheminiai poslinkiai šiek tiek skyrėsi nuo verčių, paskaičiuotų DFT metodu. Tai gali būti paaiškinta tuo, kad DFT BMR ekranavimo skaičiavimai buvo atlikti izoliuotoms molekulėms, neįskaitant

tirpiklio įtakos. Tai taip pat gali reikšti, kad išties vyko mainai tarp vandens ir kai kurių H1 protonų, tikėtina esančių agregatų paviršiuje. Staigus cheminio poslinkio padidėjimas mažėjant temperatūrai M fazėje (11c pav.) yra reikšmingai didesnis nei būtų galima tikėtis pasireiškiant tik vandeniliniam ryšiui [35].

H1 signalo išplitimas mažėjant temperatūrai gali būti sąlygotas keletos persiklojančių veiksnių, tačiau pagrindinį indėlį sudaro rotacinio judėjimo sulėtėjimas didėjant SSY agregatams. Kadangi žemose temperatūrose šaldymo ciklo metu ši juosta išnyko, galime teigti, kad signalo išplitimą taip pat įtakoja nepusiausvyrinės vietinės fluktuacijos. Visos kitos ^{1}H-BMR spektrinės juostos, esant žemoms temperatūroms taip pat išnyko, išskyrus vandens signalą (12 pav.). Šio signalo forma bei cheminis poslinkis priklausė ne tik nuo koncentracijos ir temperatūros, bet – kas svarbiausia – ir nuo temperatūrinės praeities. Taigi, tai gali būti efektyviai panaudota tyrinėjant lėtą saviorganizacijos procesą pereinant tarp N, N+M ir M fazių.

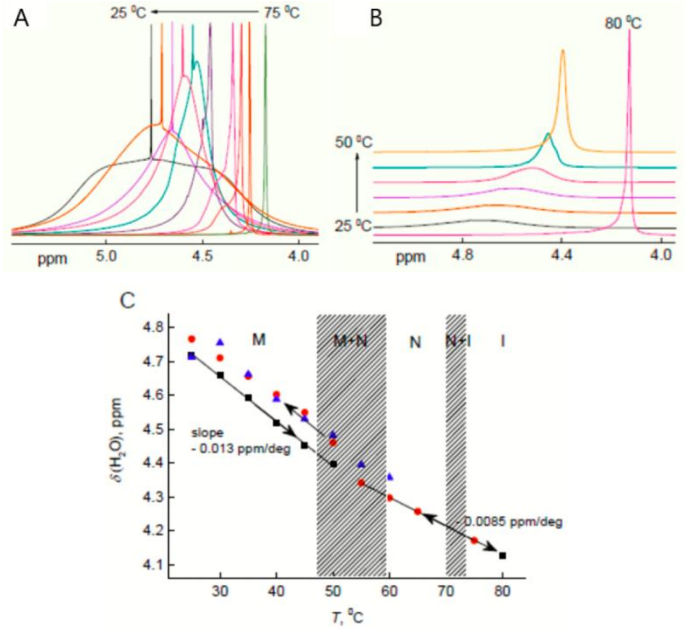

12 pav. *H_2O protonų BMR signalo formos evoliucija šaldymo (A) ir šildymo (B) ciklų metu bei H_2O cheminio poslinkio priklausomybė nuo temperatūros (C). Geresniam atvaizdavimui, šaldymo ciklo spektrai buvo sunormuoti į maksimalų signalo intensyvumą. Taškai, atitinkantys "plačius" ir "siaurus" signalo komponentus pažymėti atitinkamai mėlynais trikampiais ir raudonais apskritimais*

Lėta saviorganizacija po N + M → M fazinio virsmo

Darbo metu išmatuotos δ(N−H) ir $\delta(H_2O)$ cheminių poslinkių priklausomybės nuo temperatūros buvo praktiškai identiškos tiek šaldymo, tiek šildymo ciklų metu. Pusiausvyros nusistovėjimo laikas pereinant iš fazės N + M į fazę M yra labai ilgas. Taigi, jei bandinys yra greitai atšaldomas iki temperatūros, esančios žemiau fazinio virsmo N → M ribos, sistema patenka į peršaldytą būseną. Tokiu atveju, toliau seka lėtas saviorganizacijos procesas, kurio metu sistema grįžta į pusiausvyrąją būseną. Šis procesas aiškiai atsispindi ^{1}H-BMR spektruose. H_2O signalas, esantis ties 4.1 – 4.8 ppm, įgauna papildomus „šlaitus“ ir gali būti sudalintas į „siaurąjį“ ir „platųjį“ komponentus (9, 12 pav.). Jei bandinys dieną ar, tam tikrais atvejais, net keletą dešimčių dienų yra laikomas M fazėje pastovioje temperatūroje (+25 ºC), kompleksinė signalo forma palaipsniui pereina į vidutinio pločio vieno kontūro signalo formą. Tokia ^{1}H-BMR signalo evoliucija pavaizduota 9 paveiksle. Vizualiai bandinys ima atrodyti lyg būtų išdžiūvęs. Vis dėlto, stebimas procesas yra grįžtamasis, t.y. spektras įgauna savo pradinę išvaizdą, kai bandinys yra pašildomas. Tai reiškia, kad vanduo nebuvo išgaravęs. Be to, bandiniai buvo pakartotinai sveriami.

Akivaizdu manyti, jog agregatų augimas sudarant stulpeliais išsidėsčiusias struktūras yra lydimas vandens molekulių segregacijos tarpstulpelinėse ertmėse. Tokio izoliuoto vandens būsena buvo nagrinėjama analizuojant H_2O ^{1}H-BMR cheminių poslinkių temperatūrines priklausomybes, bei Ramano juostos formą. Įdomu pastebėti, kad esant arti N → N + M fazinio virsmo, Ramano juostos, esančios ties 2800–3800 cm^{-1}, pokyčiai atkartoja gryno vandens νO−H···O juostos elgseną ties lydymosi tašku [36]. Temperatūros pakėlimas ir peržengimas T_{NM} ~ 55 ºC ribą sąlygoja juostos intensyvumų persiskirstymą ties ~ 3185 ir ~ 3397 cm^{-1} panašiai, kaip gryname vandenyje (3138 ir 3385 cm^{-1} esant 0 ºC). Be to, pasibaigus saviorganizacijos procesui, vandens cheminio poslinkio temperatūrinės priklausomybės krypties koeficientas (−0.013 ppm/deg) sutampa su gryno vandens atveju (−0.012 ppm/deg) [37].

- Apjungus BMR, Ramano spektroskopiją bei DFT skaičiavimus, tiksliai įvertinta temperatūros ir sudėties įtaka skirtingiems SSY vandeninių tirpalų faziniams virsmams pereinant iš izotropinės fazės (I) į nematinę (N) ir kristalinę kolonų (M) fazes.

- Tyrinėjant I $\leftrightarrow$ I + N $\leftrightarrow$ N fazinius virsmus nepastebėta jokių staigių pokyčių nei Ramano, nei BMR spektruose. Spektrinių parametrų pasikeitimas yra grįžtamasis procesas tiek šaldymo, tiek kaitinimo ciklo metu naudojant įprastas temperatūros keitimo spartas. Pastebėtas labai ilgas N + M $\rightarrow$ M fazinio virsmo pusiausvyros nusistovėjimo laikas, galimai dėl lėto agregatų augimo suformuojant heksagoninius darinius M fazėje.

- SSY agregatų augimas yra lydimas vandens segregacijos proceso kristalinėse ertmėse, kas apriboja mainus tarp H_2O ir N–H protonų, esančių vidiniuose stulpeliais išsidėsčiusių darinių sluoksniuose. Tai buvo patvirtinta pirmą kartą užregistruoto ^{1}H BMR spektro N-H juosta. H_2O cheminių poslinkių temperatūrinės priklausomybės analizė ir Ramano νO–H juostos forma, parodė, kad vandens, izoliuoto tarpstulpelinėse kristalinėse ertmėse, elgsena atitinka gryną vandenį.

- Tarpkoloninėse ertmėse izoliuotos vandens molekulės galimai yra lašelių pavidalo kaip ir, pastarųjų tyrimų duomenimis, kai kuriuose joninių skysčių/vandens tirpaluose. Kadangi tiek chromoniniai liotropiniai skystieji kristalai, tiek joniniai skysčiai pasižymi periferijoje esančiomis joninėmis grupės, ši, iš pirmo žvilgsnio tolima analogija, gali būti panaudota kaip iššūkis tolimesniems eksperimentams.

- Tautomerinė SSY pusiausvyra yra stipriai pasislinkusi link hidrazono formos – mažiau nei vienas azo tautomeras tarp ~100 hidrazono tautomerų. Hidrazono formos dominavimas buvo patvirtintas eksperimentiškai pritaikant tolimosios ^{1}H–^{15}N sukinių koreliacijos BMR metodą (HMBC) bei DFT SMD skaičiavimus.

Kalcio hidroksiapatitų BMR tyrimų rezultatai

Vandens klasterių susidarymas nanostruktūrizuotuose kalcio hidroksiapatitų (CaHA) bandiniuose buvo nagrinėjamas taikant ^{1}H MAS BMR spektrometrija ir FTIR. Žinios apie klasterių formavimosi procesus inertinėse matricose gali būti labai naudingos priskiriant spektrines juostas bei nagrinėjant vandens būsenas nanostruktūrizuotuose ar kitose inovatyviose medžiagose.

2D FTIR sugerties koreliacijos analizė (2DCOR) užtikrino preciziską vandens, esančio argono matricose, persiklojančių spektrinių juostų identifikavimą [38]. Lyginant rezultatus su eksperimentiškai išmatuotais bei teoriškai apskaičiuotais kitų autorių darbuose [39, 40], buvo aiškiai išskirtos vandens monomerų, dimerų ir aukštesnių eilių klasterių (iki heksamero) juostos. Reikia atkreipti dėmesį, kad tokie eksperimentai atliekami žemose temperatūrose, kai tuo tarpu dauguma dominančių procesų bei technologijų vyrauja kambario temperatūros rėžiuose. Literatūros duomenimis [41] maži vandens klasteriai gali būti aptinkami ištirpinus vandenį hidrofiliniame CCl_4 tirpiklyje. Darbo metu užregistruoti vandens klasteriai: monomeras, dimeras, ciklinis trimetras, ciklinis tetrametras bei didelė vandenilinių ryšių struktūra, galimai heksameras. Gauti duomenys gali būti pritaikomi pereinant nuo labai žemų iki aplinkos temperatūrų, taip pat nagrinėjant vandens FTIR ir BMR spektrines savybes nano struktūrizuotose kalcio hidroksiapatituose.

Kai kurie CaHA FTIR ir BMR spektriniai bruožai yra gerai žinomi. ^{1}H MAS BMR spektre apytiksliai ties 0 ppm (13 pav.) matoma juosta yra priskiriama tūrinėms hidroksilo grupėms, t.y. hidroksilo grupėms, išsidėsčiusioms išilgai kanalėlių, susiformavusių CaHA kristalituose [42-44]. Osman kartu su bendraautoriais pirmą kartą eksperimentiškai parodė, kad ši juosta susideda iš dviejų kontūrų, galimai atitinkančių OH dipolio orientacijas „up“ (0.10 ppm) ir „down“ (-0.13 ppm), kas sąlygoja atsiradusį skirtingą atstumą tarp hidroksilo grupių protonų (14 pav.). Unikali *ν*O-H valentinio virpesio juosta ties 3572 cm^{-1} taip pat stebima FTIR metodu. Jos siaurumas parodo vandenilinio ryšio nebuvimą ir yra susijęs su atstumu tarp gretimų deguonies atomų tūrinėse hidroksilo grupėse (0.344 mm) [45].

Ypatingas dėmesys skiriamas vandens paviršinėms modoms. OH paviršinės modos yra stebimos CaHA vandens FTIR spektruose ties 3640 – 3651 cm^{-1}. Taip pat matomos protonuotų PO_4^{3-} grupių *ν*O-H valentinių virpesių juostos ties 3700 – 3850 cm^{-1} [45]. HPO_4^{2-} ir/arba $H_2PO_4^{-}$ jonų buvimas CaHA kristalitų paviršiuje buvo patvirtintas BMR CP MAS

eksperimentu [46]. Platus šių grupių cheminių poslinkių pasiskirstymas ties 8-13 ppm ^{1}H MAS BMR spektre sutampa su paviršinių *ν*P-O-H modų indėliu, stebimu FTIR spektruose.

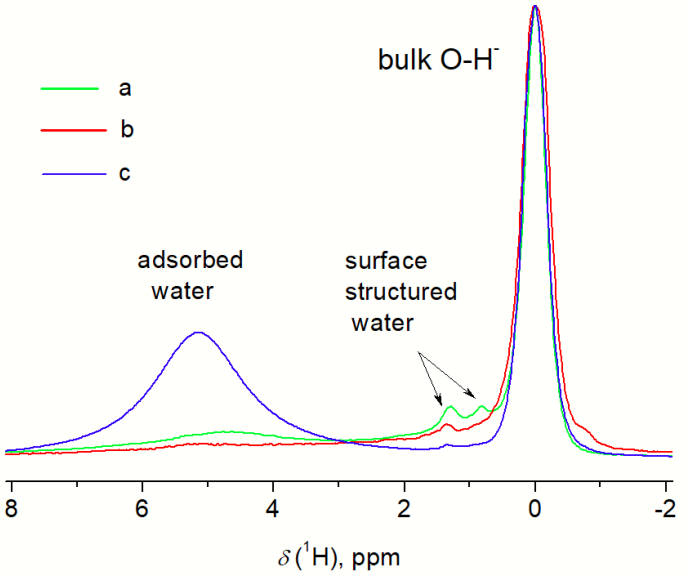

13 pav. *Kompleksinių CaHA, susintetintų zolių-gelių metodu, ^{1}H MAS BMR spektrai naudojant skirtingus kompleksadarius: a - etilenglikolį (EG), b - vyno rūgštį (TA), c - komercinis nano-struktūrizuotas CaHA. Signalų intensyvumai sunormuoti pagal tūrinių O–H⁻ protonų juostą ties ~0 ppm*

Kelios silpno intensyvumo BMR spektrinės juostos ties 0.5 – 3.0 ppm yra dažnai stebimos nagrinėjant CaHA ar panašias medžiagas [43]. Šiame darbe buvo taip pat užregistruotos dvi smailės ties 0.8 ir 1.3 ppm. Kadangi šios juostos nėra stebimos CP MAS BMR eksperimento metu, jų kilmė siejama su itin judriais protonais. Be to, smailės yra gana siauros, kas nebūdinga paviršinėms grupėms. Ilgą laiką minėtų BMR spektrinių juostų identifikavimas buvo kontraversiškas ir tik neseniai buvo parodyta, kad šios smailės priskiriamos struktūrizuotoms paviršinėms vandens molekulėms, išsidėsčiusioms išlaikant lygiavimą su turinėmis OH grupėmis [42]. Nustatyta, kad esant dideliam struktūrinio vandens kiekiui stebima tik viena spektrinė juosta ties 1.1 ppm, kuri suskyla į dvi smailes (H_2O_{UP} ir H_2O_{DOWN}) esant mažam struktūrinio vandens kiekiui.

Vandenilinio ryšio OH valentinių virpesių FTIR juosta buvo identifikuota daugelyje darbų [43, 45], tačiau paprastai jos forma ir struktūra nebūdavo nagrinėjama detaliau. Šiame darbe pirmą kartą parodyti vandens klasteriai nanostruktūrizuotuose CaHA bandiniuose. Vandens dimero, tetramero, heksamero ir galimai aukštesnės eilės klasterių komerciniame CaHA bandinyje juostos buvo išskirtos ties 2900 – 3600 cm^{-1}. Klasterių dydis ir struktūra labai priklauso nuo hidratacijos lygio. Adsorbuoto vandens kiekis buvo įvertintas BMR metodu pagal plataus ^{1}H signalo, esančio ties 5.1 ppm, intensyvumą, sunormuotą pagal OH juostą ties 0 ppm.

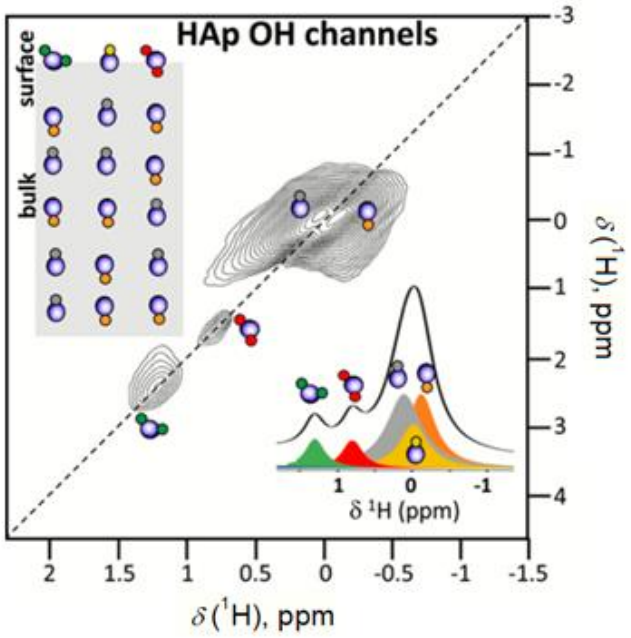

14 pav. *^{1}H 2D DQ-SQ ir ^{1}H MAS NMR spektrai bei scheminis pavaizdavimas galimų skirtingo tipo OH grupių (tūrinių bei paviršinių), taip pat struktūrizuotų paviršinių vandens molekulių konfigūracijų nanostruktūrizuotuose CaHA kristalituose. Detalesnis paaiškinimas tekste. (pagal M.B. Osman ir k.t. [42])*

- Apjungus BMR ir FTIR metodus buvo tiksliai išanalizuotos vandens būsenos bei struktūrinių OH grupių saviorganizacija. Dėl sudėtingo stebimų spektrinių savybių priskyrimo bei informacijos gausos, tai nebūtų buvę pasiekta taikant minėtus metodus atskirai.

- Įvairių tūrinių bei paviršinių cheminių grupių (PO_4, H_XPO_4, OH, H_2O) nanostruktūrizuotuose kalcio hidroksiapatituose nustatymas padeda įvertinti šių grupių vaidmenį analizuojant skirtingus CaHA, savo savybėmis artimus kauliniam audiniui, pritaikymus.

- Pirmą kartą FTIR spektroskopijos metodu nustatyta vandens klasterių nanostruktūrizuotuose kalcio hidroksiapatituose struktūra. Vandens dimero, tetramero, heksamero juostos, bei keletas paviršinių O-H ir P-O-H modų ties 2900 – 3900 cm^{-1} buvo identifikuoti lyginant vandens spektrus argono matricose ir CCl_4 tirpiklyje.

Disertacijos apibendrinimas

Disertacijos rezultatai parodė įvairiapusį BMR metodų panaudojimą tiriant nano-struktūrizuotų medžiagų bei BMR pagrindu sukurtų klinikinių metodų pritaikymo medicinoje ateities perspektyvas. Išanalizuotos keturios tyrimų grupės parodant BMR spektroskopijos tinkamumą:

1. BMR pagrindu pagrįsta MRS metodika, skirta prostatos piktybiškumo įvertinimui analizuojant metabolitų BMR spektrų elgseną.

2. Vandens difuzijos ir sukinio-gardelės relaksacijos procesų tyrimai nagrinėjant gadolinio (Gd) up-konversines nanodaleles (UCNPs), kaip potencialias dvigubo panaudojimo MRT kontrastines medžiagas, išlaikančias aukštą relaksingumą plačiame magnetinio lauko stiprumo intervale.

3. Liotropinių chromoninių skystųjų kristalų (LCLCs), daug žadančių kuriant inovacijas vaistų pernašoje bei sparčiai besivystančiuose naujos kartos biojutikliuose, tyrimai analizuojant temperatūros ir bandinio sudėties įtaką faziniams virsmams, lėtai saviorganizacijai bei tautomerinei pusiausvyrai vandeniniuose Saulėlydžio geltonojo FCF (SSY) tirpaluose.

4. Kalcio hidroksiapatitų (CaHAs), vis plačiau taikomų rekonstrukcinėje chirurgijoje gydant emalį ir kaulų defektus, tyrimai analizuojant vandens būsenas bei vandens molekulių, izoliuotų inovatyviuose nanostruktūrizuotuose CaHAs bandiniuose, klasterių susidarymą.

[1] D. Patkar, V. Jadhav, Ch. Jathar, New Advances in MRI, JIMSA, **26**, 59-64 (2013).

[2] P.D. Afonso, V.V. Mascarenhas, Imaging techniques for the diagnosis of soft tissue tumors, Reports in Medical Imaging, **8**, 63–70, (2015).

[3] D.V. Hingorani, A.S. Bernstein, M.D. Pagel, A review of responsive MRI contrast agents: 2005-2014. Contrast Media Mol Imaging, **10**, 245–265, (2014).

[4] J. Kudr, Y. Haddad, L. Richtera, Z. Heger, M. Cernak, V. Adam, O. Zitka, Magnetic Nanoparticles: From Design and Synthesis to Real World Applications. Nanomaterials, **7**, 243 (29), (2017).

[5] Y. Luo, W. Zhang, Z .Liao, S. Yang, S. Yang, X. Li, F. Zuo, J. Luo, Role of Mn^{2+} Doping in the Preparation of Core-Shell Structured Fe_3O_4@upconversion Nanoparticles and Their Applications in T1/T2-Weighted Magnetic Resonance Imaging, Upconversion Luminescent Imaging and Near-Infrared Activated Photodynamic Therapy, Nanomaterials, **8**, 466 (15), (2018).

[6] A. Nowogrodzki, The world's strongest MRI machines are pushing human imaging to new limits, Nature, **563**, 24-26 (2018).

[7] A. Capati, O.B. Ijare, T. Bezabeh, Diagnostic Applications of Nuclear Magnetic Resonance–Based Urinary Metabolomics, Magnetic Resonance Insights, **10**, 1-12, (2017).

[8] A. Fillmer, T. Kirchner, D. Cameron, A. Henning, Constrained Image-Based B0 Shimming Accounting for “Local Minimum Traps” in the Optimization and Field Inhomogeneities Outside the Region of Interest, Magn Reson Med, **73**, 1370-1380, (2015).

[9] L. Jacques, S. A. Dean, Advances in gadolinium-based MRI contrast agent designs for monitoring biological processes in vivo, Curr Opin Chem Biol, **45**, 121-130, (2018).

[10] Y.J. Lu, P.Y. Lin, P.H. Huang, C.Y. Kuo, K. Shalumon, M.Y. Chen, J.P. Chen, Magnetic Graphene Oxide for Dual Targeted Delivery of Doxorubicin and Photothermal Therapy, Nanomaterials, **8**, 193 (20), (2018).

[11] H. Lee, E. Sun, D. Ham, R. Weissleder, Chip-NMR biosensor for detection and molecular analysis of cells, Nat Med, **14**, 869–874, (2008).

[12] W.C. Lin, C.C. Chuang, C.J. Chang, Y.H. Chiu, M. Yan, C.M. Tang, The Effect of Electrode Topography on the Magnetic Properties and MRI Application of Electrochemically-Deposited, Synthesized, Cobalt-Substituted Hydroxyapatite, Nanomaterials, **9**, 200 (14), (2019).
[13] N. Agarwal, M.S. Nair, A. Mazumder, K.M. Poluri, *Characterization of Nanomaterials: Advances and Key Technologies*, Woodhead Publishing, pp 61-102, (2018).
[14] U. Klose, Measurement sequences for single voxel proton MR spectroscopy, European Journal of Radiology, **67**, 194–201, (2008).
[15] S.F. Keevil, Spatial localization in nuclear magnetic resonance spectroscopy, Phys. Med. Biol, **51**, R579–R636, (2006).
[16] G. Bellomo, F. Marcocci, D. Bianchini, E. Mezzenga, V. D'Errico, E. Menghi, et al. MR Spectroscopy in Prostate Cancer: New Algorithms to Optimize Metabolite Quantification, PLoS ONE, **11**, 1-18, (2016).
[17] M.H. Levit, *Spin Dynamics: Basics of Nuclear Magnetic Resonance*, 2nd edition, John Wiley and Sons Ltd, 724 p, (2008).
[18] S. Penzel, A. Oss, M.L. Org, A. Samoson, A. Böckmann, M. Ernst, B.H. Meier, Spinning faster: protein NMR at MAS frequencies up to 126 kHz, J Biomol NMR, **73**, 19-29, (2019).
[19] Y. Vasavi, N. Parthiban, S. Dinakaran, D. Banji, N. Srisutherson, S. Ghosh, M. Vinay, K. Chakravarthy, Heteronuclear Multible Bond Correlation Spectroscopy-An Overview, International Journal of PharmTech Research, **3**, 1410-1422, (2011).
[20] V. Balevičius, L. Kimtys, G. A. Misiūnas, *Magnetinio Rezonanso Spektrometrija*, Vilniaus Universiteto leidykla, (2000).
[21] G.A. Pereira, C.F.G.C. Geraldes, Design and Optimization of Gadolinium Based Contrast Agents for Magnetic Resonance Imaging, Ann. Magn. Reson, **6**, 1–33, (2007).
[22] J. Lu, I. Hung, A. Brinkmann, Z. Gan, X. Kong, G. Wu, Solid State ^{17}O NMR Reveals Hydrogen-Bonding Energetics: Not All LowBarrier Hydrogen Bonds Are Strong, Angew. Chem. Int. Ed, **56**, 6166−6170, (2017).
[23] A.I. Hashim, X. Zhang, J.W. Wojtkowiak, G.V. Martinez, R.J. Gillies, Imaging pH and Metastasis, NMR Biomed, **24**, 582-591, (2011).
[24] E. Von Goldammer, H. G. Hertz, Molecular motion and structure of aqueous mixtures with nonelectrolytes as studied by nuclear magnetic relaxation methods, J. Phys. Chem, **74**, 3734-3755 (1970).

[25] X.Y. Zheng, K. Zhao, J. Tang, X.Y. Wang, L.D. Li, N.X. Chen, Y.J. Wang, S. Shi, X. Zhang, S. Malaisamy, et al, Gd-Dots with Strong Ligand–Water Interaction for Ultrasensitive Magnetic Resonance Renography, ACS Nano, **11**, 3642-3650, (2017).

[26] F. Chen, W. Bu, S. Zhang, X. Liu, J. Liu, H. Xing, Q. Xiao, L. Zhou, W. Peng, L. Wang, J. Shi, Positive and Negative Lattice Shielding Effects Co-existing in Gd (III) Ion Doped Bifunctional Upconversion Nanoprobes, Adv. Funct. Mater, **21**, 4285-4294 (2011).

[27] Y. Hou, R. Qiao, F. Fang, X. Wang, C. Dong, K. Liu, C. Liu, Z. Liu, H. Lei, F. Wang, M. Gao, $NaGdF_4$ Nanoparticle-Based Molecular Probes for Magnetic Resonance Imaging of Intraperitoneal Tumor Xenografts in Vivo, ACS Nano, **7**, 330-338, (2013).

[28] M. Rohrer, H. Bauer, J. Mintorovich, M. Requardt, H.J. Weinmann, Comparison of magnetic properties of MRI contrast media solutions at different magnetic field strengths, Invest. Radiol, **40**, 715–724, (2005).

[29] H. S. Park, S. W. Kang, L. Tortora, Y. Nastishin, D. Finotello, S. Kumar, O.D. Lavrentovich, Self-Assembly of Lyotropic Chromonic Liquid Crystal Sunset Yellow and Effects of Ionic Additives, J. Phys. Chem. B, **112**, 16307−16319, (2008).

[30] X. Ding, T.C. Stringfellow, J. R. Robinson, Self-Association of Cromolyn Sodium in Aqueous Solution Characterized by Nuclear Magnetic Resonance Spectroscopy, J. Pharm. Sci, **93**, 1351-1358, (2004).

[31] E. Troche-Pesqueira, M.M. Cid, A. Navarro-Vazquez, Disodium Cromoglycate: Exploiting its Properties as a NMR Weakaligning Medium for Small Organic Molecules, Org. Biomol. Chem, **12**, 1957−1965, (2014).

[32] P. Gilli, V. Bertolasi, V. Ferretti, G. Gilli, Evidence for Intramolecular N−H···O Resonance-Assisted Hydrogen Bonding in β-Enaminones and Related Heterodienes. A Combined CrystalStructural, IR and NMR Spectroscopic, and Quantum-Mechanical Investigation, J. Am. Chem. Soc, **122**, 10405−10417, (2000).

[33] S. Zhou, K. Neupane, Y.A. Nastishin, A.R. Baldwin, S. Shiyanovskii, O.D. Lavrentovich, S. Sprunt, Elasticity, Viscosity, and Orientational Fluctuations of a Lyotropic Chromonic Nematic Liquid Crystal Disodium Cromoglycate, Soft Matter, **10**, 6571-6581, (2014).

[34] V. R. Horowitz, L. A. Janowitz, A. L. Modic, P. A. Heiney, P. J. Collings, Aggregation Behavior and Chromonic Liquid Crystal Properties of an Anionic Monoazo Dye, Phys. Rev. E, **72**, 041710 (10), (2005).

[35] V. Balevicius, Z. Gdaniec, K. Aidas, NMR and DFT Study on Media Effects on Proton Transfer in Hydrogen Bonding: Concept of Molecular Probe with an Application to Ionic and Super-polar Liquids, Phys. Chem. Chem. Phys, **11**, 8592−8600, (2009).

[36] I. Đurickovic, R. Claverie, P. Bourson, M. Marchetti, J.M. Chassot, M.D. Fontana, Water − Ice Phase Transition Probed by Raman Spectroscopy, J. Raman Spectrosc, **42**, 1408−1412, (2011).

[37] V. Balevicius, K. Aidas, Temperature Dependence of 17O NMR Shifts of Water: Entropy Effect, Appl. Magn. Reson, 32, 363−376, (2007).

[38] V. Balevicius, V. Sablinskas, I. Doroshenko, V. Pogorelov, Propanol clustering in argon matrix: 2D FTIR correlation spectroscopy, Ukr. J. Phys, **56**, 855-860, (2011).

[39] S. Coussan, P. Roubin, J.P. Perchard, Infrared induced isomerizations of water poly- mers trapped in nitrogen matrix, Chem. Phys, **324**, 527–540, (2006).

[40] R.M. Bentwood, A.J. Barnes, W.J. Orville-Thomas, Studies of Intermolecular interactions by Matrix isolation Vibrational Spectroscopy. Self-association of Water, J. Mol. Spectr, **84**, 391-404, (1980).

[41] T. Köddermann, F. Schulte, M. Huelsekopf, R. Ludwig, Formation of water clusters in a hydrophobic solvent, Angew. Chem. Int. Ed, **42**, 4904–4908, (2003).

[42] M. Ben Osman, S. Diallo-Garcia, V. Herledan, D. Brouri, T. Yoshioka, J. Kubo, Y. Millot, G. Costentin, Discrimination of surface and bulk structure of crystalline hydroxyapatite nanoparticles by NMR, J. Phys. Chem. C, **119**, 23008–23020, (2015).

[43] J. Kolmas, A. Jaklewicz, A. Zima, M. Bućko, Z. Paszkiewicz, J. Lis, A. Ślosarczyk, W. Kolodziejski, Incorporation of carbonate and magnesium ions into synthetic hydroxyapatite: the effect on physicochemical properties, J. Mol. Struct, **987**, 40–50, (2011).

[44] L. Dagys, V. Klimavicius, J. Kausteklis, A. Chodosovskaja, V. Aleksa, A. Kareiva, V.Balevicius, Solid-state ^{1}H and ^{31}P NMR and

FTIR spectroscopy study of static and dynamic structures in sol-gel derived calcium hydroxyapatites, Lith. J. Phys, **55**, 1-9, (2015).

[45] S. Diallo-Garcia, M. Ben Osman, J.M. Krafft, S. Boujday, C. Guylène, Discrimination of infrared fingerprints of bulk and surface POH and OH of hydroxyapatites, Catalysis Today, **226**, 81–88, (2014).

[46] S. Kareiva, V. Klimavicius, A. Momot, J. Kausteklis, A. Prichodko, L. Dagys, F. Ivanauskas, S. Sakirzanovas, V. Balevicius, A. Kareiva, Sol-gel synthesis, phase com- position, morphological and structural characterization of $Ca_{10}(PO_4)_6(OH)_2$: XRD, FTIR, SEM, 3D SEM and solid-state NMR studies, J. Mol. Struct, **1119**, 1–11, (2016).

Informacija apie autorę

Vardas, pavardė: Kristina KRISTINAITYTĖ
Gimimo data: 1988-01-23
El. paštas: kkristinaityte@gmail.com

Išsilavinimas:
2010 m. VU, Fizikos fakultetas, taikomoji fizika, Fizikos bakalauras
2012 m. VU, Medicinos fakultetas, Medicinos fizikos magistras
2015 10 – 2019 m. VU, Fizikos fakultetas, doktorantūros studijos, vadovas - Prof. Dr. Nomeda. R Valevičienė, konsultantas – Prof. Habil. Dr. Vytautas Balevičius**.**

Darbinė veikla:
2007 03 – 2007 10 – optinių dangų operatorius, UAB "OPTIDA" , Vilnius.
2007 10 – 2007 12 – eksperimentinės dalies grupė, Mokslo ir meno, šviesos reginių spektaklis „Langas į šviesą“ (Di luce in luce), (Paolo Di Trapani), Vilnius.
2007 10 – 2010 06 – laborantas, VU kvantinės elektronikos katedros (KEK) ir Lazerinių tyrimų centro (VU LTC) bendra laboratorija, Vilnius.
2012 06 – 2013 01 – medicininės aparatūros vadybininkas-inžinierius, UAB „Limeta“, Vilnius.
2013 01 – 2015 09 – jaunesnioji mokslo darbuotoja, Vilniaus Universitetas, Medicinos fakultetas, Vilnius
2013 01 – dabar – medicinos fizikas, VšĮ VU ligoninė Santaros klinikos, Vilnius.

Mokslinės stažuotės:
2005 09 – 2006 07 - Nacionalinė moksleivių akademija, Kauno technologijos universiteto gimnazija
2010 07 – 2010 08 - Studentų mokslinė praktika tema „Beselio pluoštai“, Vilniaus universitetas
2010 12 (16 val.) - „Projektų valdymo ir mokslo žinių komunikacijos įgūdžių tobulinimas“, Lietuvos onkologų draugija (LOD), Vilnius, Lietuva.
2014 09 18-20 - ESMRBM mokymai, „ Advanced neuroimaging: Diffusion, Perfusion, Spectroscopy“, Varšuva, Lenkija.

2016 09 05-09 - Mokymai, “Neuroimaging and fMRI data analysis - clinical and research applications”, Project “Development of neuroimaging research and clinical skills in Lithuania”, Vilnius, Lietuva
2016 09 23-26 - ESMRMB mokymai “In vivo MR spectroscopy: From basics to advanced methods”, Viena, Austrija.
2016 10 17 – 12 05 - ESMRMB e-mokymai “Basic course in applied MR techniques”
2017 06 28-30 - ESMRMB mokymai “MRI simulation for sequence development, protocol optimization and education”, Eindhovenas, Olandija.
2017 10 17-18 - ESMRMB mokymai “Small animal MR imaging”, Barcelona, Ispanija.
2018 05 01 – 2018 06 30 - Erasmus praktika, NanoBioMedicinos centras, Adomo Mickevičiaus Universitetas (AMU), Poznanė, Lenkija.

ACKNOWLEDGEMENTS

First of all, I would like to thank my family and friends, especially Vykintas, Andrius, Aistė and Rūta, who have supported me during the study years and despite being unfamiliar with the dissertation topic gave useful advices and motivation when needed mostly.

I am very grateful for the supervision by prof. Nomeda Rima Valevičienė who made it possible to explore NMR intrincacies from the clinical perspective. The same goes to all the members of the center of radiology, nuclear medicine and medical physics in Vilnius University hospital Santaros Klinikos, especially to prof. Algirdas Edvardas Tamošiūnas, dr. Jūratė Dementavičienė, Renata Baltagalvienė and dr. Dileta Valančienė, as well as to the group of medical physicists.

I am extremely grateful to prof. Vytautas Balevičius for introducing me to the academic domain and for the valuable guidance through its adventurous path. His dedication, keen interest and overwhelming attitude to help his students as well as timely advices and scientific approach have helped me to a very great extent in accomplishing different tasks throughout the study years. This also would not had been possible without assistance of Vytautas Klimavičius and Laurynas Dagys.

It is a genuine pleasure to express my sincere gratitude to prof. Liudvikas Kimtys who encouraged me to step into these interdisciplinary studies of NMR spectroscopy connecting physics and medicine.

I also express my gratitutude to all the collaborators of this work, especially to dr. Kęstutis Aidas for DFT calculations, Jonas Kausteklis for FTIR measurements, prof. Ričardas Rotomskis for giving me an opportunity to work with nanoparticles, and others. The same goes to all the members of Institute of Chemical Physics for the motivating and inspiring atmosphere during my years of study. Special thanks to Vaiva Paketurytė for the metabolites and assistance in preparing their samples.

Finally, I owe a deep sense of gratidtude to prof. Stefan Jurga for a warm welcome at NanoBiomedical center in Adam Mickiewicz University and for the opportunity to participate in the NMR summer school at Zakopane. I also thank profusely the whole team, especially to dr. Tomasz Zalewski, prof. Marek Kempka, dr. Dorota Katarzyna Flak, dr. Jacek Jenczyk, dr. Dr. Grzegorz Nowaczyk and dr. Łucja Przysiecka, for allowing me to perform a great variety of experiments and for creating the homely atmosphere during my Erasmus studies in Poznan.

PUBLICATIONS AND THEIR COPIES

I. **K. Kristinaityte**, J. Razanskas, V. Paketurytė, Nomeda R. Valeviciene, V. Balevicius, Methods of Sample Preparation for Analysis and Quality Assurance of Prostate MR Spectroscopy, Medical Physics in the Baltic States 13 (2017) p. 61-64.

II. **K. Kristinaityte**, L. Dagys, J. Kausteklis, V. Klimavicius, I. Doroshenko, V. Pogorelov, N. R. Valevicienė, V. Balevicius, NMR and FTIR studies of clustering of water molecules: from low-temperature matrices to nano-structured materials used in innovative medicine, Journal of Molecular Liquids, 235 (2017) p. 1-6.

III. **K. Kristinaityte**, A. Marsalka, L. Dagys, K. Aidas, I. Doroshenko, Y. Vaskivskyi, Y. Chernolevska, V. Pogorelov, N. R. Valevicienė, V. Balevicius, NMR, Raman, and DFT Study of Lyotropic Chromonic Liquid Crystals of Biomedical Interest: Tautomeric Equilibrium and Slow Self-Assembling in Sunset Yellow Aqueous Solutions, J. Phys. Chem. B., 122 (2018) p. 3047-3055.

IV. **K. Kristinaityte**, T. Zalewski, M. Kempka, S. Sakirzanovas, D. B. Paulaviciene, S. Jurga, R. Rotomskis, N. R. Valeviciene, Spin-Lattice Relaxation and Diffusion Processes in Aqueous Solutions of Gadolinium-Based Upconverting Nanoparticles at Different Magnetic Fields, Appl. Magn. Res., 50 (2019) p. 553-561.

UŽRAŠAMS

UŽRAŠAMS

Vilniaus universiteto leidykla
Saulėtekio al. 9, LT-10222 Vilnius
El. p. info@leidykla.vu.lt,
www.leidykla.vu.lt
Tiražas 15 egz.